ABSTRACT

Title of dissertation: CFD MODELING AND ANALYSIS
OF ROTOR WAKE IN HOVER
INTERACTING WITH A GROUND PLANE

Tarandeep Singh Kalra, Doctor of Philosophy, 2014

Dissertation directed by: Professor James D. Baeder
Department of Aerospace Engineering

The action of the rotor wake on loose sediment on the ground is primarily responsible for inducing the rotorcraft brownout phenomenon. Therefore, any simulation of brownout must be capable of accurately predicting the velocity field induced by the rotor when it is operating in ground effect. This work attempts to use a compressible, structured, overset Reynolds-Averaged Navier-Stokes (RANS) based solver to simulate hovering rotors in ground effect (IGE) to demonstrate the capability of the code to provide accurate tip vortex flow field predictions, and provide a good understanding of the ground-wake interactions. The computations are performed for a micro-scale rotor (0.086m radius, aspect ratio of 4.387 operating at a tip Mach number of 0.08 and Reynolds number of $32,500$) and a sub-scale rotor (0.408m radius, aspect ratio of 9.132 operating at a tip Mach number of 0.24 and Reynolds number of $250,000$) in order to compare to experimental measurements. The micro-scale rotor has a rectangular tip shape and is simulated three rotor heights: $1.5R$, $1.0R$ and $0.5R$ above ground (R = Rotor radius). The sub-scale rotor is simulated at one particular rotor height (i.e. $1R$) but with four different tip shapes: rectangular,

swept, BERP-like and slotted tip. Various mesh placement strategies are devised to efficiently capture the path of the tip vortices for both regimes.

The micro-scale rotor simulations are performed using the Spalart Allmaras (S–A) turbulence model. The examination of the IGE tip vortex flow field suggests high degree of instabilities close to the ground. In addition, the induced velocities arising from the proximity of the rotor tip vortices causes flow separation at the ground. The sub-scale rotor simulations show a smeared out flow field even at early wake ages due to excessive turbulence levels. The distance function in the S–A turbulence model is modified using the Delayed Detached Eddy Simulation (DDES) approach and a correction to length scaling is included for anistropic grids. The resulting computational flow field after these modifications compares well with the experiments. The slotted tip is seen to diffuse the tip vortices at early wake ages through injection of momentum and increased turbulence, and generates the least amount of unsteady pressure variation at the ground plane when compared with other three tip shapes.

CFD MODELING AND ANALYSIS OF ROTOR WAKE IN HOVER INTERACTING WITH A GROUND PLANE

by

Tarandeep Singh Kalra

Dissertation submitted to the Faculty of the Graduate School of the
University of Maryland, College Park in partial fulfillment
of the requirements for the degree of
Doctor of Philosophy
2014

Advisory Committee:
Dr. James D. Baeder, Chair/Adviser
Dr. J. Gordon Leishman
Dr. Anya Jones
Dr. Christopher Cadou
Dr. James Duncan, Dean's Representative

Dedication

This dissertation is dedicated to all the incidents and people that have shaped my thoughts.

Acknowledgments

I would like to thank my adviser, Dr.Baeder for giving me the opportunity for my best educational experience. He has shown immense patience and faced my several doubts with a calm demeanor. I believe that along with my technical education, i have learnt many soft skills from him to help me in my career. I would also like to thank Dr.Leishman. He has provided many valuable inputs from the begininng of this project and given it a proper direction. It has been a great learning experience to sit through his research group meetings. I would also like to thank Dr.Cadou who was my first adviser at University of Maryland. I would extend my gratitude to Dr.Duncan and Dr.Jones who have spared their valuable time to be a part of my dissertation committee. I want to thank Dr.Lakshminarayan who has been a guiding light for me in this project from day one up until now. I hope to inculcate the values of his sincere attitude towards the finer details of work each day. I would also like to thank Dr.Eshpuniyani whose initial encouragement led me to join graduate studies.

I am deeply indebted to my groupmates Sebastian, Shivaji and Debo who have motivated me through out this journey of last six years to stay on course. They have been personal friends and my mentors as well. I would like to thank my friends Mathieu, Harinder, Pranay, Kan, Ananth, Nishan, Juergen and Yashwant who stood by me at all times in graduate school. I have to spare a thought for all my friends from India: Rupam, Gagan (GD), Pawan(Pk), Parminder, Pawanpreet, Hardeep and Sameer who have shown faith in me.

I would like to thank my sister Gavneet and my brother in law Kuljeet. With-

Table of Contents

      (required, lower-case Roman)

List of Tables

List of Figures

x

Nomenclature

A	Flux Jacobian
c	Rotor blade chord
C_p	Pressure coefficient $= \dfrac{100 \times (p - p_\infty)}{\frac{1}{2}\rho_\infty U_\infty^2}$
C_P	Power coefficient in-ground effect $= \text{power}/(\rho\pi R^2 V_{tip}^3)$
$C_{P_{OGE}}$	Power coefficient in out of ground effect
C_T	Thrust coefficient in-ground effect $= \text{thrust}/(\rho\pi R^2 V_{tip}^2)$
$C_{T_{OGE}}$	Thrust coefficient in out of ground effect
d	Nearest wall distance
$\mathbf{D}$	Number of dimensions
E	Kinetic energy
e	Internal energy
$\mathbf{F}$	Flux function (tensor)
$\mathbf{f}$	Flux function (vector)
$\mathbf{f}, \mathbf{g}, \mathbf{h}$	Flux vectors along Cartesian directions
f	Flux function (scalar)
$\hat{\mathbf{f}}$	Numerical flux function (vector)
$\hat{f}$	Numerical flux function (scalar)
h	Rotor height above ground
i, j, k, l	Grid indices
M	Mach number
M_{tip}	Tip Mach number
Pr	Prandtl number
p	Pressure
q	normalized second invariant of the velocity gradient tensor $= \dfrac{\partial u_i}{\partial x_j}\dfrac{\partial u_j}{\partial x_i}$
r	radial distance
r_c	Vortex core radius
R	Rotor radius
Re	Reynolds number $= \dfrac{\rho_\infty U_\infty L}{\mu_\infty}$
T	Rotor Thrust
$\mathbf{u}$	Conserved variable (vector)
u	Conserved variable (scalar)
u, v, w	Flow velocity components along Cartesian directions
u', v', w'	Turbulent fluctuation velocities along Cartesian directions
V	Control volume
V_{tip}	Tip speed
V_θ	Swirl velocity
v_h	Hover induced velocity $= \sqrt{(T/2\rho A)}$
X^{-1}, X	Matrix of left and right eigenvectors
$\mathbf{x}$	Position (vector)
x, y, z	Cartesian directions

Symbols

Γ	Circulation
γ	Ratio of specific heats
Δx	Distance between adjacent grid points
ΔP	Pressure
Δt	Time step size
δ_{ij}	Kronecker delta function
ϵ	Parameter for WENO weights
λ	Eigenvalues
ω	Vorticity Magnitude
ψ	Blade azimuth angle
$\mathbf{\Phi}$	Characteristic flux function (vector)
ρ	Flow density
σ	Rotor solidity $= N_b c / (\pi R)$
τ_{ij}	Mean stresses
ζ	wake age, degrees

Subscripts

0	Initial value
i, j	Component of a vector along x_i or x_j
i, j	Function value at j-th grid point
s x	Partial derivative with respect to x
∞	Freestream flow variables

Abbreviations

CFD	Computational Fluid Dynamics
CPU	Central Processing Unit
DES	Detached Eddy Simulation
DDES	Delayed Detached Eddy Simulation
DNS	Direct Numerical Simulation
IGE	In-ground effect
IHC	Implicit Hole Cutting
LES	Large Eddy Simulation
OGE	Out of Ground Effect
MPI	Message Passing Interface
MUSCL	Monotone Upstream-centered Schemes for Conservation Laws
OVERTURNS	Overset Transonic Unsteady Navier-Stokes
PIV	Particle Image Velocimetry
RANS	Reynolds-Averaged Navier-Stokes
SA	Spalart-Allmaras
TVD	Total Variation Diminishing
VTG	Vortex Tracking Grid
WENO	Weighted Essentially Non-Oscillatory

Chapter 1

Introduction

1.1 Motivation: Problem of Rotorcraft Brownout

An issue associated with rotorcrafts operating in a desert or dusty environment is the brownout condition. When a helicopter operates at close proximity to the ground, the rotor wake causes loose sediment particles from the ground to get entrained into the air. Under certain operational conditions, particularly during takeoff and landing, these entrained particles tend to recirculate around the rotorcraft to form large dust clouds. Figure 1.1 shows the formation of such a dust cloud during the landing of a helicopter. A dense dust cloud can inhibit the ability of a pilot to perform maneuevers close to the ground due to the lack of visual cues.

Consequently, pilots can lose control of the vehicle and encounter obstacles. By DOD estimates [1], brownout accounts for three fourths of rotorcraft related accidents in Middle East operations. The engulfed sediment particles can also lead to mechanical wear and tear of the rotorcraft components, mainly affecting the rotor blade and hub. This results in huge maintainence issues and a shortening of the life span of rotorcraft components.

To avoid these issues, several possible solutions have been adopted to mitigate the effect of the brownout cloud. One solution is to provide sensor technologies to pilots which will allow them to navigate through dust clouds. The increased

Figure 1.1: A helicopter encountering brownout conditions during a landing in the desert. (Photo courtesy of Optical Air Data Systems LLC).

situational awareness because of these sensory systems [2, 3] shows an improvement in flight safety, but one can still not avoid the maintenance costs (mechanical wear and tear of rotorcraft components) incurred by brownout. Another possible solution to mitigate the effect of brownout adopted by pilots is to change the flight path [4]. Following this strategy, pilots spend lesser time during landing and takeoff maneuever to minimize the amount of dust entrainment. However, such a strategy is only limited to a few operational conditions depending on the weight of the vehicle, density altitude and particle characteristics. They also result in harder landings. The usage of sensory technologies or change in flight path only provide workarounds to limit the effects of brownout related issues. This infers the requirement for a more permanent solution to mitigate/prevent the brownout problem.

(a) Relatively mild brownout cloud beneath a hovering EH-101. Courtesy: AWI

(b) Severe brownout conditions beneath a hovering CH-47. [6]

Figure 1.2: Two rotorcraft with different brownout clouds

However, there are numerous challenges associated with studying the brownout phenomenon. The most important challenge comes from the enormity of the problem that needs to be tackled over a wide range of flight conditions and sizes of sediment particles over various terrains. In addition, photographic evidence shows that different rotorcrafts with distinct design features such as blade twist, rotor-disk loading, tip shape, number of blades, etc. produce different dust-cloud shapes while the dust cloud can also vary in their spatial extent, concentration, and rapidity of development. Some helicopters during landing approach can produce radially expanding toroidal shaped brownout clouds (seen in figure 1.2)(a)) with little vertical entrainment while leaving zones of good visibility for the pilot to maneuver within the cloud. Other helicopters can produce large, dome-shaped dust clouds that engulf the entire helicopter as observed in figure 1.2(b). Since different rotorcrafts under varying conditions show unique brownout signatures, one needs to carefully justify any simplifications to the brownout phenomenon.

1.2 Simplifying Brownout Phenomenon for CFD Modeling

The fundamental physics of brownout phenomenon consists of complex multiphase fluid dynamics involving the rotor wake (carrier phase) and sediment particles (dispersed phase). Figure 1.3 illustrates some of the fluid mechanics and sedimentology processes that are involved during brownout [9]. The carrier phase consisting of the rotor wake is the three-dimensional unsteady flow field produced by a rotorcraft operating in ground effect (IGE).

4
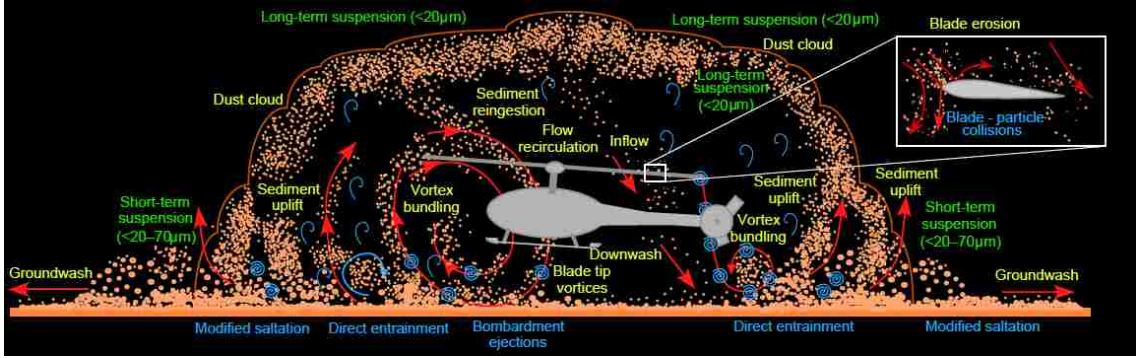
Figure 1.3: Schematic showing various mechanisms involved in brownout phenomenon [9].

The dispersed phase comprises of sediment particles that get transported under the influence of the rotor wake as it interacts with the ground. One can observe the mobilization and transport of sediment particles under the action of rotor flow in details by looking close to the ground as shown in figure 1.4. The influence of the wall jet formation and vortical structures can be seen to affect the velocity and pressure fields at the ground. The resulting shear stress distributions can produce mobilization and uplift of sediment particles [7, 8]. These observations infer that to capture all the various physical phenomenon can be quite challenging. Therefore, from a practical CFD modeling perspective, one needs to simplify this complex brownout phenomenon by assuming the following:

- Modeling the fluid-particle interaction for these complicated flow fields is extremely challenging. The development of a particle model is still an active field of research [9]. To simplify the computations, most recent studies [9, 10, 11, 12] simplify the multiphase aspect of brownout problem by ignoring the effects of airborne sediment particles on the flow field and simulate only the effect of the
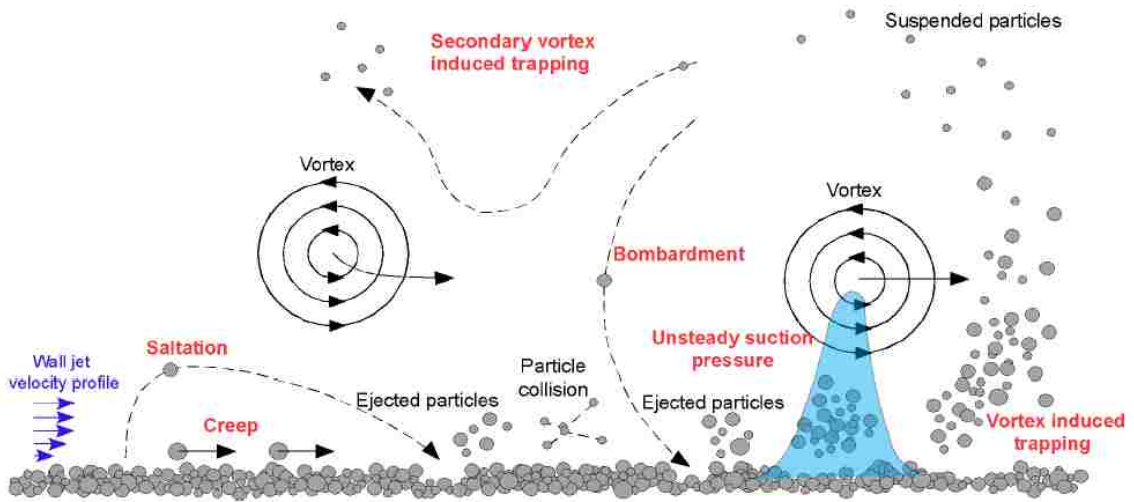
Figure 1.4: Schematic showing different sediment uplift processes (Reproduced from Sydney et al. [13]).

flow field on the particles. This is a reasonable approximation for the brownout problem, except close to the ground where the particle-density cloud may be large enough to affect the momentum of the fluid. This decoupled approach allows one to concentrate on the problem of tracking the evolution of the rotor tip vortices and their interaction with the ground boundary layer.

- Brownout occurs predominantly during landing and takeoff maneuvers. A simplified approximation for carrying out CFD modeling can assume a hovering condition for rotorcraft by ignoring any kind of dynamic maneuvers.

- It has been shown that different rotorcraft configurations generate different brownout cloud patterns. This means that various factors such as rotor shape, fuselage design and tail rotor designs feed into the evolving dust cloud. However, to first order one can ignore the effects of fuselage and tail rotor and only

6

focus on the isolated rotor for CFD analysis. One can then concentrate on the effect of the main rotor planform on tip vortex formation and subsequent interaction with the ground.

- Similar rotorcrafts performing identical landing or takeoff maneuvers can show different brownout conditions depending on the terrain over which the rotorcrafts are operating. This implies that the sediment characteristics such as the type and size of particles, their compactness, moisture content, etc. also affect the formation of dust clouds. However for CFD analysis, one can initially ignore the complicated terrain and assume a flat ground plane without the presence of sediment particles.

Thus, although the brownout phenomenon is a complex multiphase problem, one can make several simplifying assumptions to make the CFD simulations more tractable yet capture the key relevant physics with ramifications for understanding of brownout such a simplified problem is the detailed capturing of the rotor wake as it forms at the rotor surface and convects downward and outward along horizontal ground plane in hover.

1.3 Physics of Rotor Wake in Hover Interacting with a Ground Plane

The rotor hovering in ground effect (IGE) experiences a decrease in induced downward velocity compared to a rotor operating in out of ground effect (OGE). Consequently, a reduced power is required to operate at the same thrust. Similarly, for a given power, a larger thrust can be required. During hover IGE, rotor blades

operate at reduced collective to generate the same thrust and thus reduce the profile power as well [14].
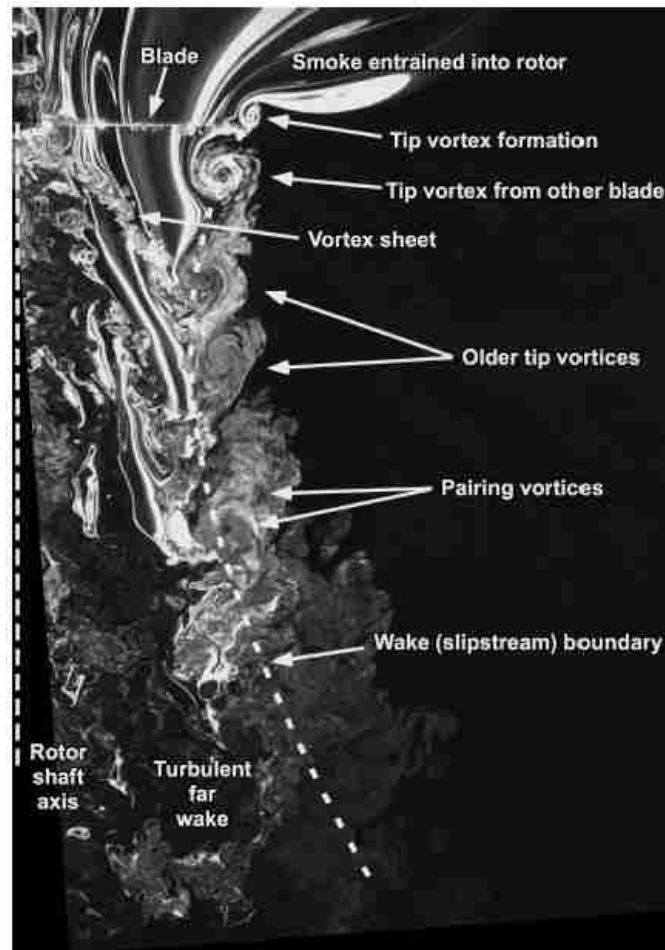
Figure 1.5: Flow field visualization of a hovering 2-bladed rotor operating in out of ground effect(OGE) [48].

Beyond the performance changes, the rotor wake under a rotor hovering IGE is very different from the one operating under OGE conditions. This is shown in figures 1.5 and 1.6 using flow visualization images. The flow is being seeded with smoke and a laser sheet illuminates a particular radial plane. The rotor blades shed helicoidal vortices that are trailed from the blade tips. These tip vortices can be
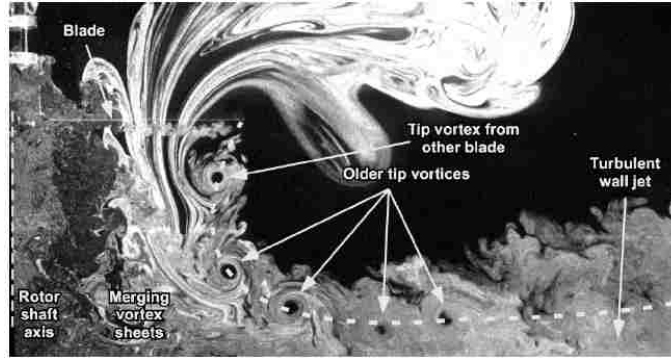
Figure 1.6: Flow field visualization of a hovering 2-bladed rotor operating in ground effect (IGE) [48].

identified by seed voids or the black circles that demarcate the vortex cores in figures 1.5 and 1.6 in a radial plane. In fig. 1.5, under OGE conditions, the tip vortices just under the plane of the rotor blade initially undergo contraction. One can notice that these vortices have laminar cores, identified by coherent seed voids. These laminar vortex cores are devoid of turbulence that is evident in the surrounding flow field. After 2-3 rotor revolutions, these tip vortices start to diffuse under the effects of viscosity and turbulence. Further downstream, these instabilities increase and flow field looks highly turbulent as tip vortices from adjacent turns end up pairing with each other at older wake ages.

Under rotor IGE conditions, as seen in figure 1.6, the rotor wake contracts initially under the plane of the rotor the same as observed in the OGE case. Note that the contraction for the IGE case is reduced compared to the OGE case because of the reduced induced velocity for the IGE case, resulting in a reduced amount of contraction. This also causes the tip vortices to stay closer to the rotor disk for the IGE case. For the IGE case, as the rotor wake convects further downwards, the
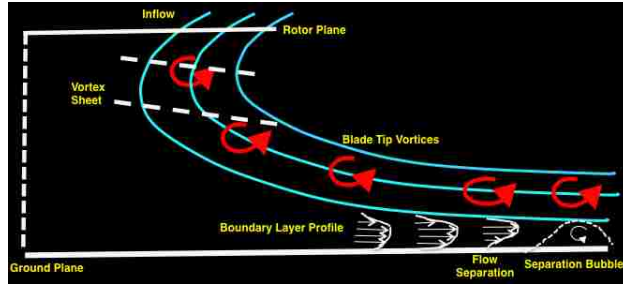
Figure 1.7: Schematic showing rotor wake formation and its interaction with a ground plane
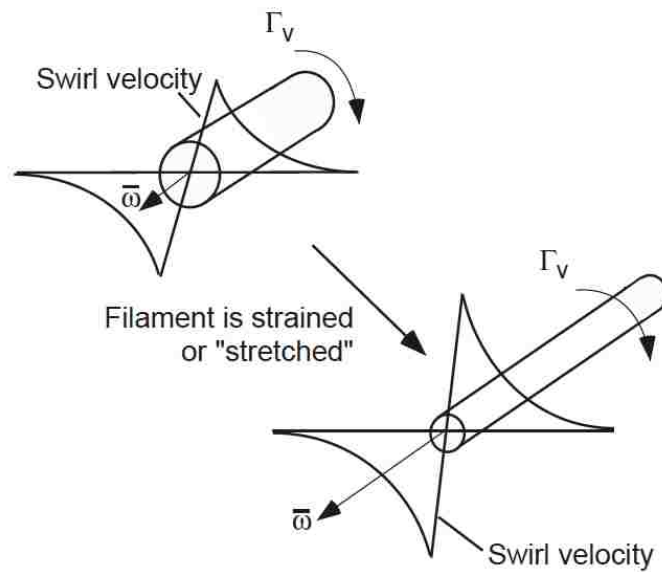
Figure 1.8: Schematic showing stretching of a vortex filament and intensification of vorticity within the vortex core with a decreasing core radius (Reproduced from Milluzzo et al. [31]).

rotor wake expands radially under the influence of the ground and the tip vortices undergo stretching. This causes the tip vortices to reintensify resulting in an increase in their swirl velocity. As a result, the tip vortices do not diffuse very much and persist to much older wake ages up until 4-5 rotor revolutions. Figure 1.8 shows the stretching effects on a tip vortex filament resulting in an increase of its swirl velocity

10

and decrease of core radius.

Close to the ground, the turning of the momentum in the rotor wake due to conservation of angular momentum causes the formation of a turbulent wall-jet like flow along the ground that initially thins, and then thickens further downstream along the ground. The tip vortices, upon getting very close to the ground (as seen in the schematic in figure 1.7, can cause adverse pressure gradients to exists on the ground plane leading to a separation of the boundary layer, that in some cases can also lead to formation of secondary vortices. The formation of secondary vortices can be an important factor for causing sediment particles to uplift and mobilize during brownout phenomenon [15]. This implies that for an accurate brownout prediction, accurate modeling of the rotor wake in hover during IGE is a prerequisite condition.

1.4   Literature Review of Related Previous Work

The focus of the present work is to use CFD tools to capture the rotor wake from a hovering rotor operating in IGE and capture its interaction with the ground in order to gain insight into the physics responsible for this brownout phenomenon. In light of the discussion presented above, one can divide the relevant physical phenomenon necessary to accurately model the rotor wake in hover and its interaction with the ground into three categories.

- Rotor thrust and power changes during IGE operation. This can be referred to as the global physics effects of IGE operation. This will affect the strength of the resulting tip vortices and the time-averaged downwash/outwash fields.

- Tip vortex formation and its initial convection. This should include the effects of tip geometry or tip blowing on tip vortices. This will affect the initial core size and turbulence levels of the tip vortex.

- Tip vortex diffusion at early wake ages, tip vortex stretching as it gets closer to the ground and aperiodicity in the flow field. At the ground, one needs to capture the perturbations to the steady outwash, as well as increased levels of turbulence, from the tip vortices and wake.

1.4.1   Measurements of Global Physics during rotor hovering IGE

Several studies in the past have focused on the problem of predicting the change in rotor thrust and power when operating IGE. Betz [16] analyzed the effect of ground on the performance of a lifting propeller. The study was performed by replacing the rotor with a sink and the ground was replaced by a mirror sink. The study showed that the power required by the propeller decreases for a constant thrust at heights lower than the propeller radius. Theoretical studies conducted by Knight and Hefner [17] used a cylindrical vortex sheet to model a lifting airscrew. They showed that the thrust coefficient increased in proximity to the ground while torque coefficient remained almost constant except for very low heights above ground. Cheeseman and Benett [18] performed a theoretical analysis to calculate the thrust and power of rotors in and out of ground at different rotor heights for varying forward speeds.

Fradenburgh [19] performed detailed studies of the flow field beneath the ro-

tor hovering IGE. The study showed that the rotor wake did not just continually contract as in OGE, but rather the tip vortices moved radially outwards as they approached the ground. A region of up wash was found near the root and there was an area of "dead air". Lighthill [20] used a modified actuator disk model for both OGE and IGE cases to calculate the induced power. The analysis showed a reduction in induced power in proximity to the ground. Hayden [21] used a large set of flight dataset measurements to develop a semi empirical model to estimate performance changes to a rotor IGE. The model introduced a modification to induced power due to the presence of ground. Rossow [22] used experimental and theoretical measurements to calculate rotor thrust and power for a model helicopter rotor. The experiments were performed in a vented wind tunnel to account for hovering and/or ceiling planes. The theoretical model was based on the squence of cylindrical vortex models similar to the ones used by Knight and Hefner [17]. This model over predicted the magnitude of change in thrust. Thererfore, a semiempirical modification was suggested to represent the wake IGE. With this modification thrust prediction improves for all ground plane distances unless the ceiling plane is not too near.

All the above studies showed a modification from global effects on rotor performance during rotor hovering IGE. Accurate modelng of these effects is a necessary condition for properly capturing the rotor wake and subsequently for an accurate understanding and modeling of the brownout phenomenon.

1.4.2 Tip Vortex Formation at Rotor Blades and Initial Convection

For an accurate prediction of the hovering rotor wake IGE, one also needs to accurately capture viscous separation and roll up into tip vortex. Comprehensive studies have been performed in both experiments and computations to estimate the tip vortex formation and its convection for early wake ages.

1.4.2.1 Experimental Studies

Caradonna and Tung [23] conducted hot wire velocity measurements in the wake of a two bladed model-scale hovering rotor. The measured peak swirl velocities were found to reach a maximum of 40% of the tip speed and the initial vortex core radius was found to be around 4% of the blade chord.

Tangler et al. [24] examined the sensitivity of the tip vortex structure to rotor blade design parameters(i.e., tip shape, number of blades and twist) for a sub-scale hovering rotor. Tests were performed for a range of tip Mach number and collective pitch settings. The maximum tip vortex swirl velocity was found to be of the order of 20%-50% of the tip speed for the collective pitch range.

Thompson et al. [25] performed detailed measurements with a laser Doppler velocimeter in the tip region and in the tip vortex core of a single-bladed subscale rotor in hover. The data exhibited evidence of a secondary structure inside the rotational core of the vortex.

Martin and Leishman [26] measured the swirl and axial velocities in the vortex system trailed from an isolated sub-scale blade in hover. The measured data in

select planes over one rotor revolution was corrected for aperiodicity. The peak swirl velocity was found to decay at a rate that was much slower than that for the measured axial velocity deficit. The effects of blade tip shape modification were also evaluated.

Ramasamy and Leishman [27] and McAlister [28] measured velocity profiles for an isolated sub-scale rotor in hover. They were able to show that the swirl velocity and circulation profiles are approximately self-similar with wake-age. Ramsamy et. al [29] performed measurements for a micro-scale rotor operating at a low tip Reynolds number of $32,400$. Flow visualization showed that the trailed vortex sheet from rotor blades was thicker than a case using higher chord Reynolds number. Similarly, core sizes were relatively large as a fraction of blade chord compared to those measured at higher vortex Reynolds number. Contrary to this trend, the core growth rate showed similar behavior as observed in higher Reynolds number cases.

Huan and Leishman [30] studied a sub-scale rotor with forward-facing slots directing incoming flow in the spanwise direction from the side edge of the blade tip. Their measurements showed a reduced peak swirl velocity in the tip vortex of 60% relative to a baseline rotor without slots. The core of the tip vortex grew to a size three times that of the baseline rotor. There was a 3% increase in power requirement for the slotted rotor.

More recently, Milluzzo and Leishman [31] used a sub-scale rotor in hover to understand the evolution of the trailed vortex wake sheet in great details. Various twist distributions of the rotor blade were examined. They showed that the vortex sheet provided a significant source of turbulence in the flow field and its development

was dependent on rotor thrust and twist distributions.

1.4.2.2   Computational Studies

Russell et al. [32, 33] performed RANS simulations using the Baldwin-Lomax turbulence model to validate the experimental hover measurements of MacAlister et al. [34]. The vortex velocity profiles from simulations were compared with measurements at distances of 0.5 and 3 chord lengths behind the trailing edge. Computed core radius was seen to be 60% larger than the experiments at 3 chord length downstream location.

Usta [35] used upto eighth order accurate symmetric TVD schemes [36] (for inviscid terms) with the Spalart-Allmaras turbulence model to model the Caradonna and Tung [23] - two bladed hovering rotor. Though high order schemes performed better than the low order schemes in predicting blade surface pressures, numerical diffusion was found to reduce the vortex strength significantly.

Tang [38] used a high order accurate Euler solver with mesh adaptation refinement and compared the evolution of peak swirl velocity with wake age for the isolated hovering rotor test case of Martin and Leishman [39]. The use of high order accuracy and mesh adaption was seen to reduce numerical dissipation.

Duraisamy and Baeder [40, 41] used the high order accurate overset RANS code, OVERTURNS, to simulate the same experiment. Detailed validations of swirl and axial velocities were achieved up to one full revolution of the wake (roughly 60 chords of evolution). In addition to this, the effect of tip blowing on the vortex

structure was studied using a surface boundary condition. Duraisamy et al. [42] also studied the formation of rollup of the tip vortex for a hovering rotor test case. The studies showed the presence of secondary and tertiary vortices resulting from crossflow separations near the blade tip.

Lakshminarayan et al. [43, 44] extended the previously described study to perform computations on a hovering micro-scale rotor. Detailed performance and wake characteristics were obtained that compared well with experiments. Different combinations of blade geometries (blunt leading/trailing edges, sharp leading/trailing edges, twist, taper) were tested to compare their relative aerodynamic performance.
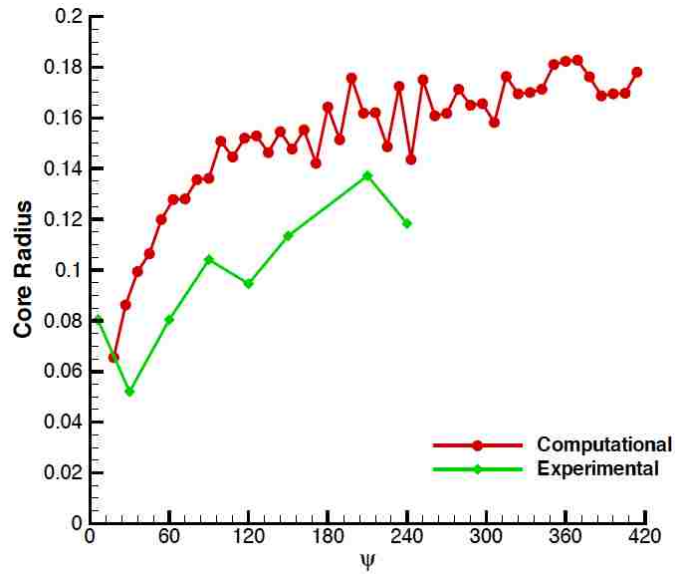
Figure 1.9: Tip vortex viscous core radius with experimental data with wake age for micro-scale single rotor hovering OGE (Reproduced from Lakshminarayan et al. [44]

The swirl velocity profiles were shown for a wake age of $180°$ and compared well with the results from experiments. The axial velocities were overpredicted by

17

less than 25%. Figure 1.4.2.2 shows that the core radius growth at 180° wake age was overpredicted by 20% in computations and the discrepancy with experiments were observed even at early wake ages. This indicates an inconsistency in the tip vortex formation. One of the reasons suggested in this work was the inadequacy of the Spalart-Allmaras turbulence model in a non isotropic environment such as regions of tip vortex formation and recommended investigating a higher fidelity approach such as Detached Eddy Simulations (DES). Another possibility for this discrepancy was attributed to the insufficient mesh resolution near the blade tip.

This last work laid down the foundation of the methodology for the current theses and the modeling of the hovering micro-scale rotors and sub-scale rotors during IGE operation has been performed using the same OVERTURNS solver.

1.4.3 Vortex Convection and Their Interaction With Ground

In order to understand the vortex convection towards the ground, their persistence to older wake ages IGE and their interaction with the ground, several studies have been conducted using experiments and computations.

1.4.3.1 Experimental Studies

Taylor [45] used balsa dust to carry out early flow visualization experiments to qualitatively study the flow patterns IGE produced by single and coaxial rotors.

Curtiss et al. [46] performed experiments to investigate the aerodynamic characteristics of an isolated rotor IGE at low advance ratios. A recirculation region was

seen at the low end of advance ratios in the rotor wake and a ground vortex was formed at higher advance ratios. Hot wire measurements showed that the strength of the ground vortex was about an order of magnitude larger than the individual tip vortices.

Light [47] used a wide-field shadowgraph method to perform flow visualization studies of rotor tip vortices produced by a hovering full scale Lynx tail rotor operating IGE and OGE. The axial descent and radial geometry of tip vortex were found to be functions of the rotor distance from the ground plane.

Lee et al. [48] conducted flow visualization and digital phase-resolved particle image velocimetry (DPIV) experiments to study the flow field on a micro-scale rotor at various heights above a ground plane. Digital PIV analysis was performed for four rotor heights - $0.25R$, $0.5R$, $1.0R$, and $1.5R$. Time-averaged and phase-averaged velocity profiles measurements were extracted close to the ground. The significance of mechanisms such as vortex diffusion, vortex stretching, and turbulence generation were studied. As the rotor wake approached the ground, vortex stretching was shown to have the effect of increasing swirl velocities within the vortex cores leading to a reintensification of vorticity. It was found that these stretching effects were largest when the rotor hovered at an intermediate height above the ground. Beyond this height, the effects of vortex diffusion became more significant than vortex stretching.

Nathan and Green [49] studied single and dual phase flow fields around a micro-scale rotor IGE operating at different heights above ground and at low advance ratios. Investigation using single-phase flow showed the formation of a recirculation region at low advance ratios and the formation of a ground vortex at higher

advance ratios. Dual-phase flow visualization used fine talcum powder particles as dispersed phase and it was observed that the particles accumulated near regions of high vorticity such as the ground vortex or the recirculation zone.

Johnson et al. [15] performed a detailed study of time varying single and dual-phase phase flows created by a micro-scale rotor hovering IGE. The single-phase results showed highly aperiodic phenomena resulting from the pairing and merging of adjacent turns of the blade tip vortices. These phenomena increased the induced velocities and consequently the shear stresses on the ground, which in turn increased initial mobilization and uplift of particles from the bed. Measurements made close to the boundary layer showed the presence of a separation bubble just downstream of the vortex impingement zone. The dispersed phase showed the mechanisms of saltation, saltation bombardment, reingestion bombardment and vortex induced trapping.

Milluzzo et al. [50] measured the evolution of a hovering sub-scale rotor wake IGE for various tip shapes (rectangular, swept, BERP-like, and slotted-tip) using flow visualization and phase-averaged PIV techniques. The rotor operated at $1R$ rotor height above the ground. The measurements resulted in a detailed dataset of rotor wake characteristics such as core size and swirl velocity profiles for upto $800°$ wake age. PIV measurements were able to could obtain radial velocity profiles deep into the boundary layer. An interesting result of this study was the observation that the diffusion of tip vortices for the slotted-tip geometry at early wake ages led to a reduced unsteady flow intensity at the ground.

Glucksman-Glaser and Jones [51] used dye flow visualization and PIV tech-

niques to qualitatively and quantitatively measure the flow field around a micro-scale rotor operating over a sediment bed in a water tank. It was found that the passage of tip vortices was causing the unsteady velocities to cause sediment mobilization. Results showed that the time-averaged data (that corresponded to global effects) did not capture the sharp velocity or pressure fluctuations at the ground. On the other hand, phase averaged data (that corresponded to local effects) could represent coherent tip vortices in the rotor wake and could provide valuable information on the up lift mechanisms. This study concluded that it is pertinent to match the local effects as well as the global effects while one is trying to capture the effects of full scale systems using small scale rotors.

Sydney and Leishman [52] performed time averaged PIV and particle tracking velocimetry on a micro-scale rotor hovering IGE over a sediment bed. Experiments were conducted with an isolated rotor and with three bodies representing generic fuselage shapes placed in the wake of the rotor. PIV results showed that the presence of the bodies led to a local intensification of vorticity by stretching effects and the excessive stretching caused a bursting of the otherwise coherent vortex core. For the case of an isolated rotor close to the ground, the radial velocities were symmetric and particles were concentrated away from the rotor blade. However, with the presence of bodies, the radial velocities were not symmetrically distributed and were lower in value compared to the case of an isolated rotor. Consequently, the sediment particles got lifted closer to the rotor rather than getting convected outwards and stayed suspended in the flow field.

1.4.3.2   Computational Studies

Xin et al. [53] used a finite state approach to theoretically model a hovering rotor IGE operating over a partial ground plane. The results compared the inflow distribution and performance with the experiments conducted using a Yamaha $R-50$ helicopter. In this approach, an induced inflow distribution at the rotor disk is assumed and then the ground plane is modeled using pressure perturbations. Other than the several inherent assumptions in this method, the advantages lie in its computational efficiency and the ability to model complicated dynamic environments such as inclined ground planes or even the addition of aeroelasticity for the rotor system.

Another approach to model rotors IGE is to use a Lagrangian based flow field solvers - free-vortex method [9]. A Lagrangian approach eliminates the need of high grid densities and allows for computations to involve larger physical distances as required during rotor wake convection and its interaction IGE. The rotor wake in this method is represented by full-span curved vortex filaments. A Weissenger-L blade model is used to obtain strengths of the bound circulation on rotor blades. The vortex filaments are assumed to have the same circulation strengths. These filaments are assumed to be straight line segments and are convected at local flow velocities using the Biot-Savart Law. The ground plane is modeled using an image plane method as seen in fig. 1.4.3.2. The evolution of tip vortices under the effects of viscous diffusion, turbulence, and stretching during IGE operation are based on an empirical model; where the vortex core radius grows with wake age as a function

of vortex Reynolds number. The interaction of the various tip vortices is governed by the Biot Savart's law. The problem of increased run time using Biot Savart's law has been largely circumvented by use of parallelization and fast multipole algorithms [9].
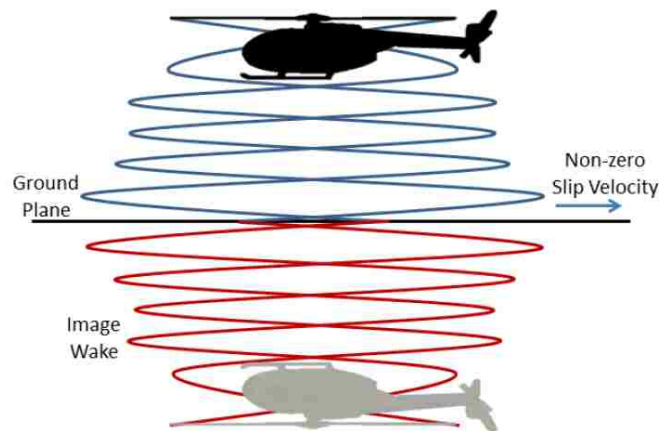
Figure 1.10: Representative free-vortex wake solution obtained using the "method of images" for a rotor operating IGE [9].

This method was used by Griffiths et al. [54] to study the shovering rotor wake IGE and more recently employed by Syal [9] to model the IGE cases for small-scale and full-scale brownout problems. Similar FVM based approaches have been used by Bhattacharaya et al. [55], Wachspress et al. [56] and D'andrea et al. [57] as well. Overall a FVM based methodology is at least two orders of magnitude faster than a RANS approach for rotor wake preservation for longer wake ages. However, the primary disadvantage of this method is that the use of image plane methods leads to a prediction of finite slip velocities at the ground plane, necessiating the use of empirical models to approximate the ground boundary layer.

Phillips and Brown [11, 58] used an inviscid vorticity transport method (VTM) to model the rotor flow IGE. VTM is a finite-volume method that solves the unsteady and incompressible Navier-Stokes equations in vorticity-velocity form using structured meshes. An advantage of a VTM solver over Lagrangian methods is that the small scale features resulting from the breakdown of larger vortical structures are properly resolved. However, the ground boundary layer is modeled using the method of images leading to finite slip velocities at the ground plane.

Wenren et al. [10] used an unsteady and incompressible vorticity confinement method to model rotors IGE. The rotors are modeled using a lifting line code with the resulting forces imposed as a source term. These equations were solved on uniform coarse Cartesian grids. The resulting flow field was generated for a hovering UH-60A helicopter. Tip vortices were shown to roll along the ground plane and this led to concentric rings of increased particulate concentration. Overall their vorticity confinement method is able to resolve tip vortices using coarse meshes. However, these coarse meshes lead to poorly resolved boundary layer at the ground.

Hariharan et al. [59] used a RANS based solver, Helios, that is capable of adaptive mesh refinement to resolve the important flow features locally along with a combination of higher order schemes. The body mesh was unstructured and employed a second order scheme while the off-body meshes were Cartesian and used a fifth-order spatial scheme. An inviscid wall boundary condition was used to model the ground plane. The rotor blade used in the experiments of Caradona and Tung [23] was operated at $0.5R$ rotor radius above ground. The qualitative results showed the expansion of the rotor wake (seen in fig. 1.11(a)) as it approached the

24
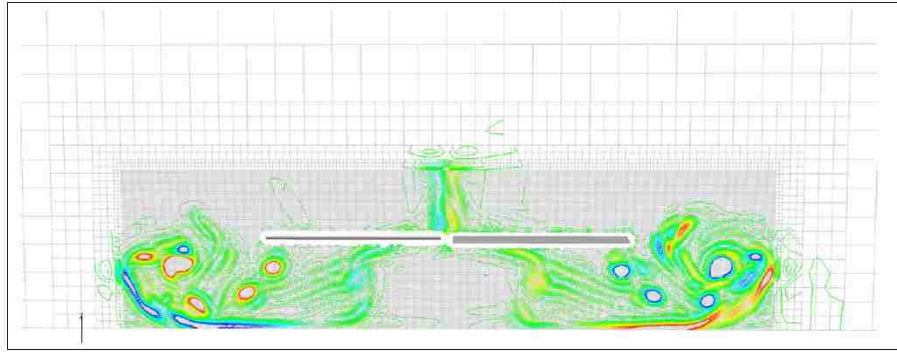
(a) Vorticity magnitude contours
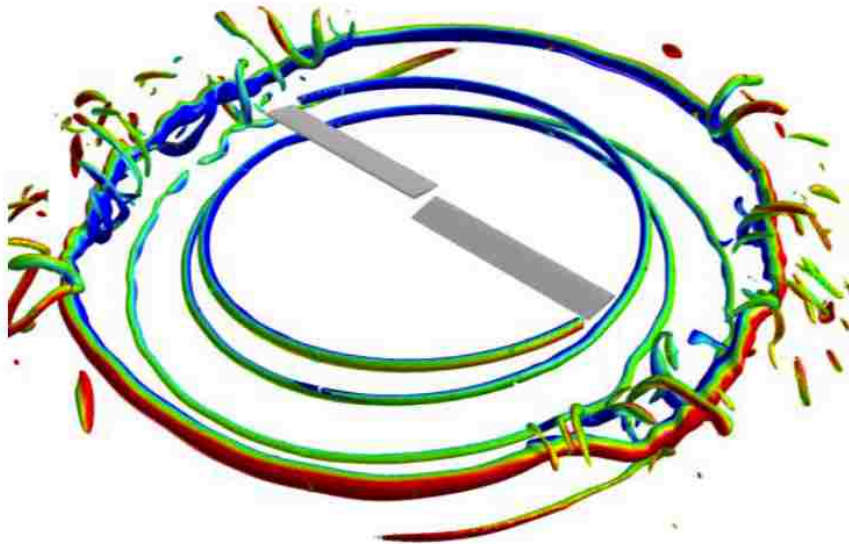
(b) Iso-surfaces of vorticity magnitude contours

Figure 1.11: Hovering rotor IGE operating at $h/R = 0.5$ above ground (Reproduced from Hariharan et al. [59]).

ground. Figure 1.11(b) shows the 3-D flow field using the iso-surfaces of vorticity magnitude. One can clearly observe the formation of secondary vortical structures around the distorted rotor wake as it approached the ground wake. It appears that the simulations were not ran long enough to develop and capture proper outwash.
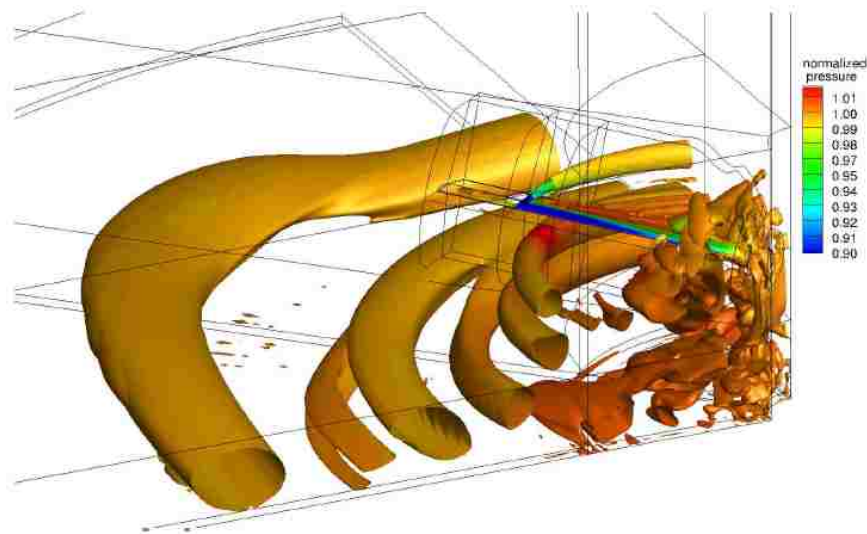
Figure 1.12: Pressure contours for a hovering rotor IGE at $h/R = 0.52$ (Reproduced from Kutz et. al [60]).

Kutz el al. [60] performed rotor IGE computations in hover and low speed forward flight. Computations were performed using a RANS solver with the ground plane using a viscous wall boundary condition. The hover simulations use a total of 7 million mesh points. Thrust values from the computations deviate roughly with a variation of 10% compared to experiments. Figure 1.12 shows the pressure contours for a hovering rotor IGE at a $h/R = 0.52$. The flow field results show the expansion of rotor wake along the ground. It is observed that the air in the center region of the rotor disk moves upwards and a fountain effect is formed. The discrepancy in performance results was attributed to this fountain effect that creates additional vertical drag. Increased unsteadiness was observed with decreasing rotor heights above the ground. A lack of mesh resolution in this work was observed due to the lack of discrete vortices in the flow field and this work could only capture global

outwash effects with such a mesh setup.

Morales and Squires [61] modeled the flow field in the near wall region using Direct Numerical Simulation (DNS). Coherent vortices were introduced in the flow field by adding a source term in the momentum equation. The presence of these vortices distorted the turbulent boundary layer flow. This increased the wall shear stress and raised kinetic energy levels of turbulence. Coupled with a Lagrangian based particle solver, this study helps in understanding the effect of vortices and turbulent boundary layers on the mobilization of sediment particles. Although a DNS based study can provide details of turbulence at the ground plane necessary for understanding causes of brownout phenomenon, the prohibitive cost makes it infeasible for any practical use.

To reduce the computational expense of a RANS methodology, one approach is to identify regions of the flow field where viscous and turbulent phenomena need to be properly resolved. One can then use a RANS solver in these regions and a lesser sophisticated but more numerically efficient model in the remainder of the flow field.

Thomas et al. [12] developed a hybrid methodology that combined the high fidelity of a RANS solver with the computational efficiency of a free-vortex method. Figure 1.13 describes this hybrid method; where the rotor wake is convected using vortex filaments using FVM (Lagrangian model) and close to the ground a CFD mesh is placed and RANS solver (Eulerian model) enables the capture of viscous and turbulent phenomena that feeds into the sediment mobilization mechanisms for brownout. The two models were coupled using a field velocity method such that the
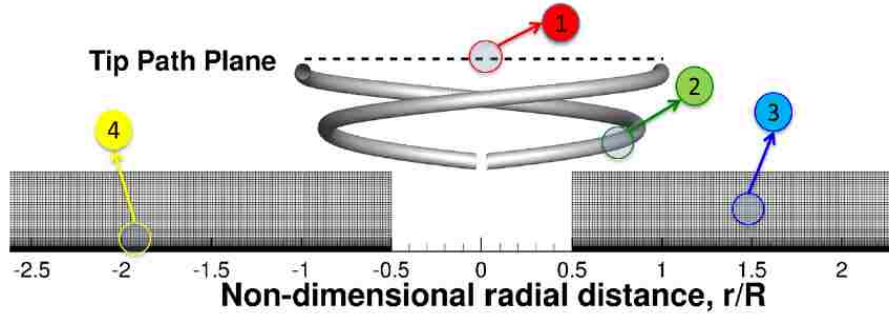
Figure 1.13: Schematic describing the structure of the Hybrid FVM-RANS Solver for a hovering rotor IGE simulation (Reproduced from [12] et al.) (1) For the airloads distribution, a linearized aerodynamics module is used. (2) Computations in the far-wake region between the rotor tip path plane are performed using a free-vortex method. (3) A high-fidelity RANS solver is used for computations near the ground plane. (4) For dual-phase flows, the RANS solution is coupled to a particle transport solver

velocities induced by the Lagrangian free-wake are imposed upon the CFD grid in addition to the velocities that are calculated by solving the RANS equations. This Euler-Lagrangian methodology was solved on a GPU based framework. Further, the model was coupled with the particle model developed by Syal [9]. The computations were qualitatively compared with experiments from the hovering micro-scale rotor IGE over a sediment bed performed by Sydney et al. [13]. Figure 1.14(a) shows the experimental results that show the formation of sediment waves outboard from the rotor when the tip vortices pass over the multiple layers of particles in the sediment bed. Similarly computations also show the capture of sediment waves (figure 1.14(b)).
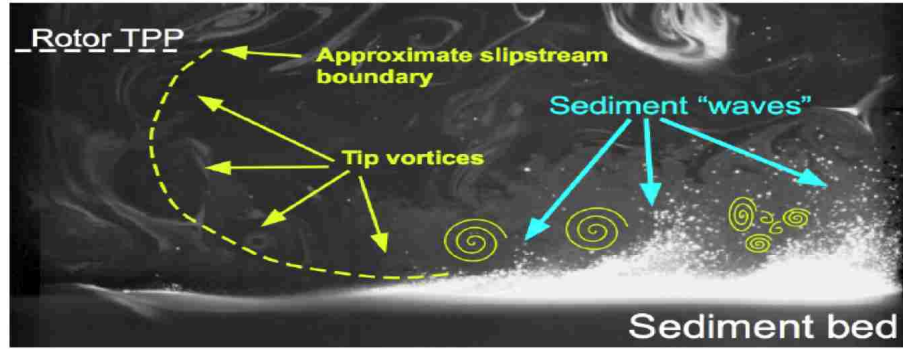
(a) Formation of sediment waves in experiments
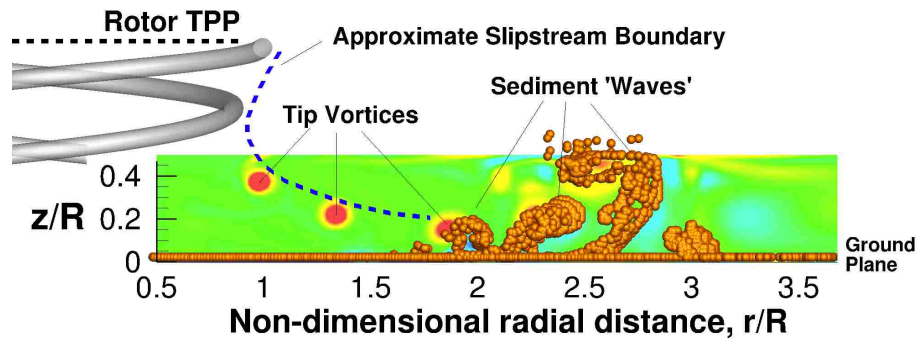
(b) Formation of sediment waves in hybrid methodology

Figure 1.14: The formation of sediment waves outboard of a micro-scale rotor. Note: Particles are not drawn to scale (Reproduced from [12] et al.)

1.5 Objectives of the Thesis

All the above mentioned computational approaches in the review work assume one or more of these factors during modeling:

1. Turbulence is not modeled and empirical models for vortex diffusion and stretching effects is used.

2. Ground plane is modeled as an invsicid wall.

3. Poor mesh resolution leading to vortex diffusion for longer wake ages.

Modeling of the tip vortex formation and convection of the rotor wake and its viscous interaction with the ground requires that none of these factors can be ignored and one needs a method that overcomes all of these challenges. The primary objective of this work is to overcome all these challenges. To accomplish this, the current work utilizes a RANS-based compressible, overset structured solver, OVERTURNS, to study the viscous and turbulent effects of rotor wake development and its viscous interaction with the ground. Further, the CFD results need to be thoroughly compared with the experiments. The following are the specific objectives of the computations from this work:

1. Accurate prediction of rotor performance.

2. Accurate capturing of tip vortex formation.

3. Maintain the tip vortex until it reaches the ground with high fidelity.

4. Provide a detailed understanding of flow physics near the ground. This includes the capture of unsteady boundary layer, diffusion/intensification of tip vortices IGE, and turbulence levels near the ground.

5. Investigate the effect of scaling parameters such as number of blades, Reynolds number and the effect of varying rotor tip shapes.

1.6   Contribution of the Thesis

The key contributions of this research include:

1. Developed a RANS based framework to model the rotor in ground effect. This required an appropriately refined overset mesh system, use of higher order spatial scheme and correct turbulent length scaling in the wake.

2. Performed a detailed capturing of the unsteady rotor wake IGE using CFD that includes turbulence and viscous wall effects at the ground. The results were validated qualtitatively and quantitatively.

3. The developed methodology enabled the modeling of varying rotor tip shapes in order to study the effect of tip shapes, as well as rotor scaling. All these variations in computations were validated with available qualitative and quantitative data from three different experimental tests.

1.7 Scope and Organization of Thesis

The present work is focused on the prediction of the hovering rotor wake and its interaction with the ground. This work looks at understanding and predicting the effects of rotor height, tip shape and scale. The rest of the thesis is organized as follows.

Chapter 2 describes the computational methodology employed in this study. This chapter is concerned with the description of the RANS based OVERTURNS code along with the implementation details of the various components of the code.

Chapter 3 first describes the evolution of the mesh system used for the micro-scale rotor simulations. Computational data for rotor wake capturing is presented for varying rotor heights above the ground. These simulation results are compared

with the available experimental data, followed by a detailed analysis of various flow field quantities at the ground.

Chapter 4 describes the mesh methodology for the sub-scale rotor along with the modeling challenges for this scale of rotors. Analysis of the the flow field originating from varying tip shapes is presented in detail and compared to available experimental data.

Chapter 5 details the conclusions and observations from this work as well as recommendations for future work.

Chapter 2

OVERTURNS Methodology

The present chapter describes the governing equations for the computations. The computations were performed using an overset structured Reynolds Averaged Navier Stokes solver, OVERTURNS (Overset Transonic Unsteady Rotor Navier-Stokes). The RANS equations form a system of nonlinear partial differential equations that are used to solve for unsteady and compressible flow in an Eulerian framework. The governing equations are non-dimensionalized and then Reynolds-averaged. A curvilinear coordinate transformation leads to solving the governing equations for curved coordinate lines. The resulting equations are numerically discretized on a computational domain and a system of coupled algebraic equations are solved to obtain the flow field solution. All the computations are performed in a time-accurate manner in the inertial frame of reference.

2.1   Governing Equations

The governing equations represent the conservation of mass, momentum and energy for a given fluid flow under the continuum hypothesis. Mathematically, the compressible Navier Stokes (NS) equations are a system of hyperbolic conservation laws in a given control volume. The Cartesian system of NS equations in strongly

conservative form are expressed in Eq. 2.1

$$\frac{\partial Q}{\partial t} + \frac{\partial F_i}{\partial x} + \frac{\partial G_i}{\partial y} + \frac{\partial H_i}{\partial z} = \frac{\partial F_v}{\partial x} + \frac{\partial G_v}{\partial y} + \frac{\partial H_v}{\partial z} \tag{2.1}$$

where Q is the vector of conserved variables, F_i, G_i and H_i are the inviscid flux vectors and F_v, G_v and H_v are the viscous flux vectors. S represents the body forces and/or account for a change in reference frame. The vector of conserved variables (Q) is expressed in Eq. 2.2

$$Q = \begin{bmatrix} \rho \\ \rho u \\ \rho v \\ \rho w \\ E \end{bmatrix} \tag{2.2}$$

The density is given by ρ, the velocity components along each dimension are u, v and w in the Cartesian coordinate system (x; y; z). E is the total energy per unit volume given by Eq. 2.3 :

$$E = \rho[e + \frac{1}{2}\rho(u^2 + v^2 + w^2)] \tag{2.3}$$

where, e is the internal energy per unit mass. The primitive variables are formed by the vector: (ρ,u,v,w,p).

The inviscid and viscous flux vectors are given by Eqs. 2.4-2.9

$$F_i = \begin{bmatrix} \rho u \\ \rho u u + p \\ \rho u v \\ \rho u w \\ (E + p)u \end{bmatrix} ; \tag{2.4}$$

$$G_i = \begin{bmatrix} \rho v \\ \rho v u + p \\ \rho v u + p \\ \rho v w \\ (E + p)v \end{bmatrix} ; \tag{2.5}$$

$$H_i = \begin{bmatrix} \rho w \\ \rho w u + p \\ \rho u w \\ \rho w w \\ (E + p)w \end{bmatrix} ; \tag{2.6}$$

$$F_v = \begin{bmatrix} 0 \\ \tau_{xx} \\ \tau_{yx} \\ \tau_{zx} \\ u\tau_{xx} + v\tau_{yx} + w\tau_{zx} - q_x \end{bmatrix} ; \tag{2.7}$$

$$H_v = \begin{bmatrix} 0 \\ \tau_{xz} \\ \tau_{yy} \\ \tau_{yz} \\ u\tau_{xy} + v\tau_{yy} + w\tau_{zy} - q_y \end{bmatrix} ; \qquad (2.8)$$

$$H_v = \begin{bmatrix} 0 \\ \tau_{xz} \\ \tau_{yz} \\ \tau_{zz} \\ u\tau_{xx} + v\tau_{yz} + w\tau_{zz} - q_z \end{bmatrix} ; \qquad (2.9)$$

where q_x, q_y and q_z are heat conduction terms expressed as a function of temperature (T) and coefficient of thermal conductivity (k) given by Eq. 2.10:

$$q_j = k\frac{\partial dT}{\partial x_j}(j = x, y, z) \qquad (2.10)$$

The viscous stress tensor for Newtonian fluids, τ_{ij}, is given by Stokes' hypothesis in Eq. 2.11:

$$\tau_{ij} = \mu[(\frac{\partial du_i}{\partial x_j}) + \frac{\partial du_i}{\partial x_j} - \frac{2}{3}\frac{\partial du_i}{\partial x_j}\delta_{ij}] \qquad (2.11)$$

where, $\delta_{ij} = 1$ if $i = j$ $\delta_{ij} = 0$ if $i = j$ and δ_{ij} is the Kronecker delta function.

The coefficient of molecular viscosity is given by Sutherland's law as follows:

$$\mu = \frac{C_1 T^{(3/2)}}{(T + C_2)} \qquad (2.12)$$

where, $C_1 = 1.4 \times 10^{-6} kg/(ms\sqrt{K})$ and $C_2 = 110.4K$ for air at standard temperature and pressure. To close the system of equations, the equation of state for ideal

gases is used:

$$p = \rho R T \tag{2.13}$$

where, R is the gas constant. Since all the flows studied in this work involve air at standard temperature and pressure, the calorically perfect gas assumption is valid. A calorically perfect gas is an ideal gas with constant specific heats. Specific heat at constant volume (C_v) and specific heat at constant pressure (C_p) are given by Eq. 2.14:

$$C_v = \frac{R}{\gamma - 1}; C_p = \gamma \frac{R}{\gamma - 1} \tag{2.14}$$

The following relations between various thermodynamic quantities are applicable to calorically perfect gases:

$$p = (\gamma - 1)\rho e$$

$$e = C_v T \tag{2.15}$$

where, e is the internal energy. The total energy per unit volume, E, can be now re-written in terms of pressure, p, and velocity components as follows:

$$E = \frac{p}{\gamma - 1} + \frac{1}{2}\rho(u^2 + v^2 + w^2) \tag{2.16}$$

where, γ is the ratio of specific heats and $\gamma = 1.4$ for air at standard temperature and pressure.

2.2 Rotating Frame of Reference

For the computation of unsteady flows involving moving bodies, the governing equations are usually solved in the inertial frame of reference. This requires com-

putation of the metric terms and connectivity information of the overset grids (if any) at every time-step. This additional cost can be avoided for hovering rotors if the equations are solved in the rotating reference frame [21]. To account for the non-inertial reference frame, the fluxes in Eqs. 2.4-2.6 become

$$
F_i =
\begin{bmatrix}
\rho(u - u_g) \\
\rho u(u - u_g) + p \\
\rho(u - u_g)v \\
\rho(u - u_g)w \\
(u - u_g)(E + p)
\end{bmatrix} ;
\tag{2.17}
$$

$$
G_i =
\begin{bmatrix}
\rho(v - v_g) \\
\rho(v - v_g)u + p \\
\rho(v - v_g)u + p \\
\rho(v - v_g)w \\
(v - v_g)(E + p)
\end{bmatrix} ;
\tag{2.18}
$$

$$
H_i =
\begin{bmatrix}
\rho(w - w_g) \\
\rho(w - w_g)u + p \\
\rho u(w - w_g) \\
\rho(w - w_g)w \\
(w - w_g)(E + p)
\end{bmatrix} ;
\tag{2.19}
$$

where, $U = u, v, w$ is the vector of physical velocities in the inertial frame and $U_g = u_g, v_g, w_g = \omega \times r$ is the rotational velocity vector. ω is the angular velocity vector given by $0, 0, \omega_z$ for a hovering rotor, rotating about the $z-$axis and r is the

38

relative position vector from the axis of rotation. Thus for a hovering rotor rotating about the z-axis, U_g becomes $\omega_z y, \omega_z x, 0$. In addition, the relative acceleration terms have to be included as a source term vector S in eqn. 2.1 and for the hovering rotor can be simplified to:

$$S = \begin{bmatrix} 0 \\ \rho v \omega_z \\ -\rho u \omega_z \\ 0 \end{bmatrix} ; \qquad (2.20)$$

2.3   Non-Dimensionalising Navier Stokes Equation

The Navier Stokes equations are often solved in their non-dimensional form. There are two advantages of doing this: (1) parameters such as Mach number and Reynolds number can be varied independently, (2) all variables are normalized to fall in the vicinity of (0,1), thereby reducing numerical inaccuracies that may occur due to mathematical operations between largely different values. Generally, a characteristic dimension such as the chord of an airfoil is selected to non-dimensionalize the length scale, while free-stream conditions are used to non-dimensionalize the dependant variables. The non-dimensional variables (with superscript $*$) are given below:

$$t^* = \frac{t a_\infty}{L}, \ (x^*, y^*, z^*) = \frac{(x, y, z)}{L}, \ (u^*, v^*, w^*) = \frac{(u, v, w)}{a_\infty},$$

$$\rho^* = \frac{\rho}{\rho_\infty}, \ T^* = \frac{T}{T_\infty}, \ p^* = \frac{p}{\rho a_\infty^2}, \ e^* = \frac{e}{\rho a_\infty^2}, \ \mu^* = \frac{\mu}{\mu_\infty} \qquad (2.21)$$

where for problems involving airfoil sections, chord length of the airfoil is chosen as the reference length, L, a is the speed of sound and subscript ∞ represents free-stream condition. Substituting the above relations into the governing equations in Eq. 2.21 gives a new set of equations in terms of the non-dimensional variables. The non-dimensional equations are identical in form to the dimensional equations except for the viscous stress tensor and thermal conduction terms. Modified viscous stress tensor and heat conduction terms are given below:

$$\tau_{ij} = \frac{\mu M_\infty}{Re_\infty} \left[\left(\frac{\partial u_i}{\partial x_j} + \frac{\partial u_j}{\partial x_i} \right) - \frac{2}{3} \frac{\partial u_k}{\partial x_k} \delta_{ij} \right] \tag{2.22}$$

$$q_j = -\frac{\mu M_\infty}{Re_\infty Pr(\gamma - 1)} \frac{\partial T}{\partial x_j} \tag{2.23}$$

All independent and dependent variables in the above two equations are non-dimensional, and the superscript $*$ representation is dropped. The new non-dimensional parameters that are formed as a result of non-dimensionalization are given below::

$$\text{Reynolds number :} \quad Re_\infty = \frac{\rho_\infty u_\infty L}{\mu_\infty} \tag{2.24}$$

$$\text{Mach number :} \quad M_\infty = \frac{u_\infty}{a_\infty} \tag{2.25}$$

$$\text{Prandtl number :} \quad Pr_\infty = \frac{\mu C_p}{k} \tag{2.26}$$

For air at standard temperature and pressure, the Prandtl number, $Pr = 0.72$ and V_∞ is the free-stream total velocity given by $\sqrt{u_\infty^2 + v_\infty^2 + w_\infty^2}$

2.4   Reynolds-Averaged Navier-Stokes Equation

The current work aims to capture the rotor wake and its interaction with the ground. Since the wake interaction with the ground is inherently a turbulent flow problem, one needs to solve the governing equations for turbulent flows. Turbulent flow is characterized by the chaotic motion of molecules, leading to increased momentum and energy exchange between various layers of the fluid and also between the fluid and the wall. Although these chaotic fluctuations of the flow variables are of a deterministic nature, the number of grid points needed for sufficient spatial resolution of all the scales of these fluctuations present a significant problem. Despite the performance of modern supercomputers a direct simulation of turbulence by the time-dependent Navier-Stokes equations, called Direct Numerical Simulation (DNS), is still possible only for rather simple flow cases at low Reynolds numbers.

A first level of approximation of turbulence is achieved using the Large- Eddy Simulation (LES) approach. The N-S equations are spatially filtered based on the scale of the grid to perform LES. The resulting equations capture the large scale eddies/turbulence that are strongly affected by the geometry of the body and small scales of turbulent motion are modeled using a subgrid-scale model. Since LES requires significantly less grid points than DNS, the investigation of turbulent flows at much higher Reynolds numbers becomes feasible. However, LES still remains computationally too expensive and is still far from becoming an engineering tool.

The next level of approximation of turbulence is performed by using Reynolds-Averaged Navier-Stokes (RANS) Equations. RANS equations augmented with tur-

bulence models present an affordable alternative to LES and DNS simulations. In the RANS approach, dependent variables in the baseline governing equations Eq. 2.1 are decomposed into their mean and fluctuating components and the resulting equations are averaged over a period of time. The Reynolds-Averaged Navier-Stokes (RANS) equations [62] are used in this study, where the flow variables are decomposed into their mean and fluctuating parts, i.e.,

$$\phi = \overline{\phi} + \phi' \tag{2.27}$$

where ϕ' is the fluctuation and $\overline{\phi}$ is the mean, defined as,

$$\overline{\phi} = \frac{1}{\chi} \lim_{\Delta t \to \infty} \frac{1}{\Delta t} \int_0^{\Delta t} \chi \phi(t) dt \tag{2.28}$$

where ϕ' is the fluctuation and $\overline{\phi}$ is the mean, defined as,

The time period Δt must be large compared to the period of turbulent fluctuations but small compared to the time scales of mean flow variation in unsteady flows. The time average of fluctuationg quantity is zero:

$$\overline{\phi'} = \frac{1}{\Delta t} \int_{t_0}^{t_0 + \Delta t} \phi' dt \tag{2.29}$$

The following relations hold for sum and product of any two fluctuating quantities:

$$\overline{\overline{f} g'} = 0; \quad \overline{\overline{f} g} = \overline{f} \overline{g}; \quad \overline{f + g} = \overline{f} + \overline{g} \tag{2.30}$$

The most important identity is that the time-average of the product of two fluctuating quantities is not zero:

$$\overline{f' f'} \neq 0 \text{ and } \overline{f' g'} = 0 \tag{2.31}$$

In the Reynolds decomposition approach, the dependent variables in the N-S equations are written as a sum of their mean and fluctuating components as shown below:

$$u = \overline{u} + u'; \;\; v = \overline{v} + v'; \;\; w = \overline{w} + w'; \;\;\;\; \rho = \overline{\rho} + \rho'; \;\; T = \overline{T} + T' \tag{2.32}$$

Substitution of the Reynolds-decomposed dependent variables in Eq. 2.32 into the instantaneous, unsteady N-S equations in Eq. 2.1, followed by time-averaging of the equations gives rise to a new set of governing equations. These are known as the Reynolds- Averaged Navier Stokes equations. They are identical in form to unsteady N-S equations, with the addition of new terms. These new terms are the functions of turbulent fluctuating quantities. These additional terms behave as an apparent stress tensor due to the transport of momentum by turbulent fluctuations. Hence, they are known as the Reynolds Stress Tensor and are given by:

$$(\overline{\tau_{ij}})_{turb} = -\rho\overline{u_i u_j} = \frac{\mu M_\infty}{Re_\infty}\mu[(\frac{\partial du_i}{\partial x_j}) + \frac{\partial du_i}{\partial x_j} - \frac{2}{3}\frac{\partial du_i}{\partial x_j}\delta_{ij}] \tag{2.33}$$

Closure to the RANS equations requires representation of the Reynolds stress tensor (τ_{ij}) in terms of the mean flow quantities. Various turbulence models are used to find the closure to the RANS equations. In the present study, the one-equation Spalart-Allmaras turbulence model [63] with the rotational correction [65] is used. Details of the turbulence modeling are discussed later in the chapter.

2.5 Curvilinear Coordinate Transformation

A curvilinear coordinate transformation maps the governing equations from a non-uniform spaced Cartesian domain (x,y,z) onto a computational domain (ξ,η,

ζ) as shown in fig. 2.1. The chain-rule of differentiation on the Cartesian set of equations results in the following:

$$\frac{\partial \tilde{Q}}{\partial t} + \frac{\partial \tilde{F}}{\partial \xi} + \frac{\partial \tilde{G}}{\partial \eta} + \frac{\partial \tilde{H}}{\partial \zeta} = \tilde{S} \tag{2.34}$$

(a) physical space   (b) computational space
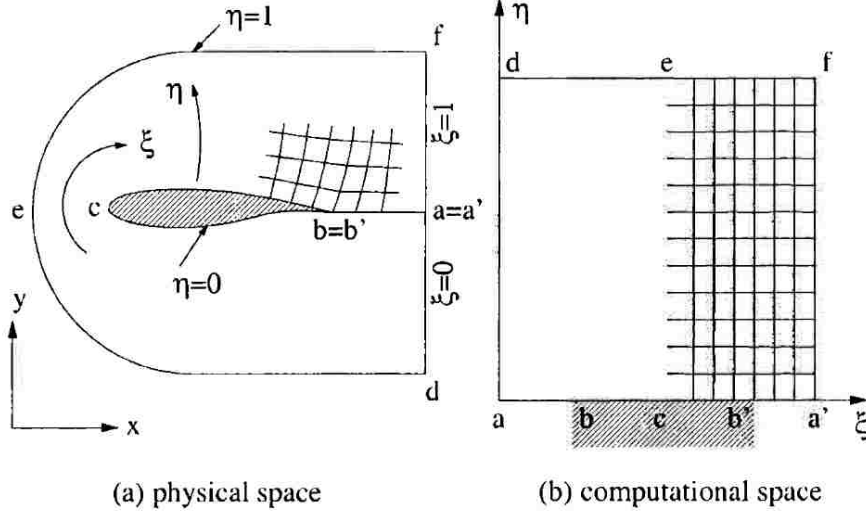
Figure 2.1: Curvilinear mapping of physical space onto computational space (reproduced from [66].

where,

$$\tilde{Q} = \frac{1}{J}Q$$

$$\tilde{E} = \frac{1}{J}[\xi_t Q + \xi_x(F_i - F_v) + \xi_y(G_i - G_v) + \xi_z(H_i - H_v)]$$

$$\tilde{F} = \frac{1}{J}[\eta_t Q + \eta_x(F_i - F_v) + \eta_y(G_i - G_v) + \eta_z(H_i - H_v)]$$

$$\tilde{F} = \frac{1}{J}[\zeta_t Q + \zeta_x(F_i - F_v) + \zeta_y(G_i - G_v) + \zeta_z(H_i - H_v)]$$

$$\tilde{S} = \frac{1}{J}S \tag{2.35}$$

44

J is the Jacobian of the coordinate transformation and is defined by the determinant of the 3×3 matrix, $\frac{\partial(\xi,\eta,\zeta)}{\partial(x,y,z)}$.

2.6   Numerical Algorithms in OverTURNS

This section describes the various numerical algorithms for spatial and temporal discretization of the governing equations, turbulence modeling, numerical boundary conditions, and convergence acceleration techniques available in the Over-TURNS fow solver. The curvilinear form of the RANS equations are solved by creating a fictitious volume around each grid point on a structured mesh. This fictitious volume is created around a point using the midpoints of the lines joining the adjacent grid points to the grid point. The faces of this volume lie exactly in the middle of two grid points. This volume is treated as a control volume and fluxes are evaluated at the faces of the volume, resulting in conservation equations for the volume. The semi-discrete conservative approximation of Eq. 2.36 can be written as

$$\frac{\partial \tilde{Q}}{\partial t} = -\frac{\tilde{F}_{j+\frac{1}{2}} - \tilde{F}_{j-\frac{1}{2}}}{\Delta \xi} - \frac{\tilde{G}_{k+\frac{1}{2}} - \tilde{G}_{k-\frac{1}{2}}}{\Delta \eta} - \frac{\tilde{H}_{j+\frac{1}{2}} - \tilde{H}_{j-\frac{1}{2}}}{\Delta \zeta} + \tilde{S}_{ij} \qquad (2.36)$$

where, (j,k,l) are the indices corresponding to the grid points in (ξ,η,ζ) directions respectively and $(j \pm \frac{1}{2}, k \pm \frac{1}{2}, l \pm \frac{1}{2})$ define the interfaces of the computational cell. The following section discusses the spatial discretization techniques used to evaluate the inviscid and viscous flux contributions at each cell face.
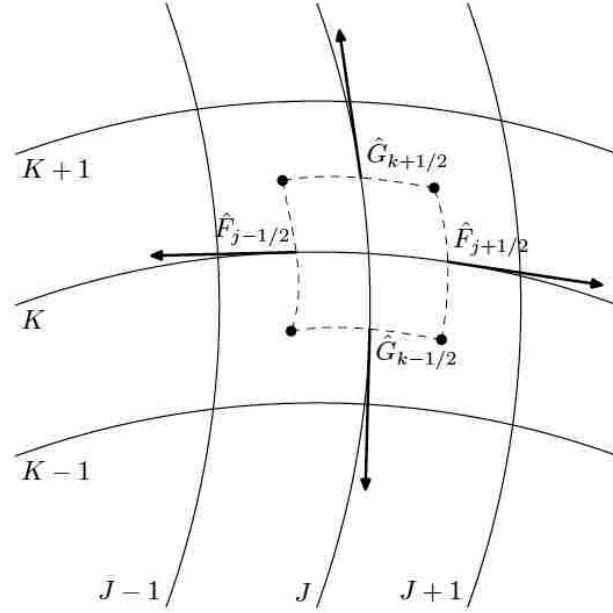
Figure 2.2: Schematic showing computational cell.

2.6.1 Inviscid Terms

Inviscid fluxes are evaluated in OverTURNS involving two steps: (1) reconstruction of the conservative variables at cell interfaces, and (2) evaluation of the fuxes at cell faces using reconstructed conservative variables. Reconstruction schemes for systems with hyperbolic properties are often based on some form of upwinding, through inclusion of explicit or implicit dissipation terms. This ensures that the numerical scheme follows the direction of wave propagation and uses information only from the upstream direction.

Figure 2.6.1 shows that the left and right states are calculated at the cell interface $j + \frac{1}{2}$ using the reconstruction of conservative variables in cell j and $j + 1$. The order of accuracy of the evaluation of the left and right states is governed by the stencil used (number of neighboring points). In this work, the third-order
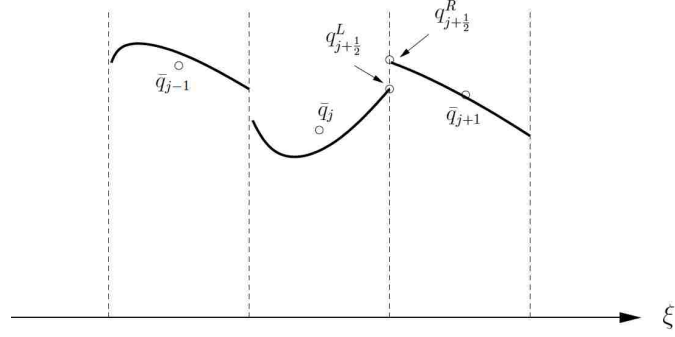
Figure 2.3: Schematic of one dimensional piecewise reconstruction.

Monotone Upstream- Centered Scheme for Conservation Laws (MUSCL) [67] and Weighted Essentially Non-Oscillatory (WENO) [68] are used for the reconstruction on the left and right cell faces. Either of the two schemes are used based on the mesh under consideration.

After evaluation of the left and right states at the cell interface, the next step is to calculate the fluxes at the interface. The left and right states can be used to define a local Riemann problem and the interfacial flux can be obtained using any flux splitting scheme. The baseline TURNS code uses the Roe flux difference splitting [69] with an entropy fix in which, the interfacial flux is given by:

$$F(q^L, q^R) = \frac{F(q^L) + F(q^R)}{2} - |\tilde{A}(q_L, q_R)| \frac{(q^R - q^L)}{2} \tag{2.37}$$

where F_L and F_R are the left and right state fluxes and $\tilde{A}$ is the Roe-averaged Jacobian matrix. The second term on the right-hand side of the above equation represents numerical dissipation. Harten's entropy correction to Eigenvalues of the fux Jacobian is given by [36]:

$$|\lambda| = \begin{cases} |\lambda| & \text{if } |\lambda| > \delta \\ \frac{\lambda^2 + \delta^2}{2\delta} & \text{if } |\lambda| \leq \delta \end{cases} \tag{2.38}$$

where $\delta = \max[0, (\bar{\lambda}_{i+\frac{1}{2}} - \bar{\lambda}_i), (\bar{\lambda}_{i+1} - \bar{\lambda}_{i+\frac{1}{2}})]$. The overbar on λ indicates Roe-averaged Eigenvalues.

2.6.1.1 MUSCL scheme with Koren's limiter

The third order Monotone Upstream-Centered Scheme for Conservation Laws (MUSCL) with Koren's differentiable limiter [70] is used to limit the high order reconstruction, so that the resulting scheme is third order accurate in smooth regions and is progressively lower order accurate (down to first order at a solution discontinuity) in high gradient regions. Given cell averaged values $\bar{q}_{j+1}, \bar{q}_j, \bar{q}_{j-1}$, the cell reconstruction is such that the interface value $q^L_{j+1/2}$ and $q^R_{j-1/2}$ is given below:

$$q^L_{j+1/2} = \bar{q} + \phi_i \left[\frac{1}{3}(\overline{q_{j+1}} - \overline{q_j}) + \frac{1}{6}(\overline{q_j} - \overline{q_{j-1}}) \right] \tag{2.39}$$

$$q^R_{j-1/2} = \bar{q} - \phi_j \left[\frac{1}{3}(\overline{q_{j+1}} - \overline{q_j}) + \frac{1}{6}(\overline{q_j} - \overline{q_{j-1}}) \right] \tag{2.40}$$

where ϕ is the Koren's differentiable limiter given by:

$$\phi_j = \frac{3\Delta \overline{q_j} \nabla \overline{q_j} + \epsilon}{2(\Delta q_j - \nabla q_j)^2 + 3\Delta q_j \nabla q_j + \epsilon} \tag{2.41}$$

and where ϵ is a small number to prevent division by zero, and Δ and ∇ are forward and backward operators defined by $\tilde{\Delta q_j} = (q_{j+1} - q_j)$ and $\nabla \tilde{q_j} = (q_j - q_{j-1})$

2.6.1.2 WENO5 Scheme

The fifth-order Weighted Essentially Non-Oscillatory (WENO5) scheme was constructed in [68]. WENO5 scheme uses a convex combination of stencils such that a high order of accuracy is achieved in all flow regions. The convex combination is chosen such that in high gradient regions, the smoothest stencil is assigned the maximum weight, resulting in a third order accurate reconstruction for a five point stencil. In a smooth region, fifth order accuracy is approached. The interface values are given by:

$$q_{i+\frac{1}{2}}^{L} = \sum_{r=0}^{k} w_r v_r^{L} \tag{2.42}$$

where, w_r are the weights and v_r^{L} are the interpolations from various stencils. Further,

$$
\begin{aligned}
w_r &= \frac{\alpha_r}{\sum\limits_{s=0}^{k} \alpha_s} \\
\alpha_r &= \frac{d_r}{(\beta_r + \epsilon^2)}
\end{aligned}
\tag{2.43}
$$

where, d_r are the optimal weight coefficients, β_r are smoothness indicators and $\epsilon = 10^{-6}$. The equations for v_r^{L}, d_r and β_r are given by:

$$v_0^L = \frac{1}{3}\overline{q}_i + \frac{5}{6}\overline{q}_{i+1} - \frac{1}{6}\overline{q}_{i+2}$$

$$v_1^L = -\frac{1}{6}\overline{q}_{i-1} + \frac{5}{6}\overline{q}_i - \frac{1}{6}\overline{q}_{i+1}$$

$$v_2^L = \frac{1}{3}\overline{q}_{i-3} - \frac{7}{6}\overline{q}_{i-1} - \frac{11}{6}\overline{q}_i$$

$$d_0 = \frac{3}{10}$$

$$d_1 = \frac{3}{5}$$

$$d_2 = \frac{1}{10}$$

$$\beta_0 = \frac{13}{12}(\overline{q_i} - 2\overline{q_{i+1}} + \overline{q_{i+2}})^2 - \frac{1}{4}(\overline{3q_i} - 4\overline{q_{i+1}} + \overline{q_{i+2}})^2$$

$$\beta_1 = \frac{13}{12}(\overline{q_{i-1}} - 2\overline{q_i} + \overline{q_{i+1}})^2 - \frac{1}{4}(\overline{q_{i-1}} - \overline{q_{i+1}})^2$$

$$\beta_2 = \frac{13}{12}(\overline{q_{i-2}} - 2\overline{q_{i-1}} + \overline{q_i})^2 - \frac{1}{4}(\overline{q_{i-2}} - 4\overline{q_{i-1}} + 3\overline{f_i})^2 \qquad (2.44)$$

2.6.2 Viscous terms

Viscous fluxes given in eqs. 2.7–2.9 in OverTURNS contain derivate terms of the form:

$$\frac{\partial}{\partial \xi}\left(\alpha\frac{\partial \beta}{\partial \eta}\right) \qquad (2.45)$$

These terms are solved using the second order central differencing as shown:

$$\frac{1}{2}\left(\left[\alpha_{j+\frac{1}{2},k}\frac{\beta_{j+\frac{1}{2},k+1} - \beta_{j+\frac{1}{2},k}}{\Delta\eta}\right] - \left[\alpha_{j-\frac{1}{2},k}\frac{\beta_{j-\frac{1}{2},k+1} - \beta_{j-\frac{1}{2},k-1}}{\Delta\eta}\right]\right) \qquad (2.46)$$

where, $\delta_{j+\frac{1}{2},k} = \frac{\delta_{j,k}+\delta_{j+1,k}}{2}$ and $\delta = (\alpha, \beta)$.

2.6.3 Time Integration

After the inviscid and viscous fuxes on the right hand side of Eqn. 2.36 are evaluated, the conservative variables (Q) are evolved in time on the left hand side. Two types of time marching methods can be used, explicit or implicit. Explicit methods only use information from the previous time step to calculate the conservative variables at the new time step; however, implicit methods indirectly use information from the new time step. Implicit methods require inversion of large space sparse matrices to accomplish this. Explicit methods have limitations on time steps based on mesh size and flow quantities. Contrary to that, most implicit methods do not have such limitations. They are more suited for boundary layer flows due to their superior stability and convergence characteristics compared to explicit time integration methods. In the present work, the semi discrete equation shown in Eqn. 2.36 is integrated using a second-order accurate backwards in time method (also knowns as BDF2) and is shown here:

$$\frac{\partial \tilde{Q}^{n+1}}{\partial t} = \frac{\partial \tilde{F}_{j+1/2}^{n+1} - \tilde{F}_{j-1/2}^{n+1}}{\Delta \eta} + \frac{\partial \tilde{G}_{k+1/2}^{n+1} - \tilde{G}_{k-1/2}^{n+1}}{\Delta \xi} + \frac{\partial \tilde{H}_{k+1/2}^{n+1} - \tilde{H}_{k-1/2}^{n+1}}{\Delta \zeta} + \tilde{S}_{j,k,l}^{n+1}$$

(2.47)

where,

$$\frac{\partial \tilde{Q}^{n+1}}{\partial t} = \frac{3\tilde{Q}^{n+1} - 4\tilde{Q}^n + \tilde{Q}^{n-1}}{2\Delta t}$$

(2.48)

In Eqn. 2.47, the fluxes are not known at the (n+1) time step, so there is a need for them to be linearized and expressed in terms of fluxes and conservative variables at the previous time step (n). The nonlinear terms are linearized in time

about $\tilde{Q}^n$ by Taylor series as:

$$\tilde{F}^{n+1} = \tilde{F}^n + \tilde{A}\Delta\tilde{Q} + O(\Delta t^2)$$

$$\tilde{G}^{n+1} = \tilde{G}^n + \tilde{B}\Delta\tilde{Q} + O(\Delta t^2)$$

$$\tilde{H}^{n+1} = \tilde{H}^n + \tilde{C}\Delta\tilde{Q} + O(\Delta t^2) \tag{2.49}$$

where, $\Delta\tilde{Q} = \tilde{Q}^{n+1} - \tilde{Q}^n$ is the difference between the old and (solution update), and A, B, C are flux Jacobians given by $\frac{\partial\tilde{F}}{\partial\tilde{Q}}, \frac{\partial\tilde{G}}{\partial\tilde{Q}}, \frac{\partial\tilde{H}}{\partial\tilde{Q}}$. The source term, S, is linearized in a similar manner. Since the linearization operation is second order accurate, it will not further degrade the time accuracy of second order BDF2 scheme. The linearized form of Eqn.2.47 in terms of the solution update, $\Delta\tilde{Q}$, is given by:

$$[I + \Delta t(\partial_\eta\tilde{A}^n + \partial_\xi\tilde{B}^n + \partial_\zeta\tilde{C}^n)]\tilde{Q} = -\Delta t[\partial_\eta\tilde{F}^n + \partial_\xi\tilde{G}^n + \partial_\zeta\tilde{H}^n - \tilde{S}^n] \tag{2.50}$$

The right hand side of the above equation represents the physics of the flow field (accuracy) and the left hand side represents the numerics responsible for stability and convergence of the solution. It can be easily shown that the implicit algorithm produces a large banded system of algebraic equations. The matrix is sparse, but it would be very expensive to solve the algebraic system in order to obtain a solution for $\Delta\tilde{Q}^n$. Further approximations to the LHS are necessary for ease of inversion of the matrix, but the penalty comes in some loss in the speed of convergence.

OverTURNS contains two methods for inverting the system equations, 1) Lower-Upper Symmetric Gauss-Seidel (LUSGS) [71] method and 2) Approximate

Diagonalized Alternate Direction Implicit (DADI) [72]. In the current work, the micro-scale rotor cases employ DADI method while the sub-scale cases use the LUSGS method for inversion purposes. Then following sections describe both LUSGS and DADI method in details.

2.6.4 LUSGS

In the LUSGS algorithm, the left-hand side of the equations is factorized by grouping terms into a lower diagonal (L), an upper diagonal (U), and a main diagonal (D) as follows:

$$[L + D + U]\tilde{Q}^n \simeq [D + L]D[D + U]\tilde{Q}^n = -\Delta t[RHS]^n \tag{2.51}$$

where,

$$L = -\Delta t(-\tilde{A}^+_{j-1,k,l} - \tilde{B}^+_{j,k-1,l} - \tilde{C}^+_{j,k,l-1}) \tag{2.52}$$

$$U = -\Delta t(-\tilde{A}^-_{j+1,k,l} - \tilde{B}^-_{j,k+1,l} - \tilde{A}^+_{j,k,l+1}) \tag{2.53}$$

$$D = I + \Delta t(\tilde{A}^+_{j,k,l} - \tilde{A}^-_{j,k,l} + \tilde{B}^+_{j,k,l} - \tilde{B}^-_{j,k,l} + \tilde{C}^+_{j,k,l} - \tilde{C}^-_{j,k,l}) \tag{2.54}$$

This can be solved by a forward and a backward sweep using a two-factor scheme that can be written as:

$$[D + L]\Delta Q = -\Delta t[RHS]^n \tag{2.55}$$

$$[D + U]\Delta\tilde{Q} = D[\tilde{Q}] \tag{2.56}$$

Additional simplifications are done by approximating the split flux Jacobians (e.g., $\tilde{A}^+$ and $\tilde{A}^-$ in terms of spectral radius (e.g.σ_v) as $\tilde{A}^+ = \frac{1}{2}(\tilde{A} + \sigma_\xi)$ and $\tilde{A}^- = \frac{1}{2}(\tilde{A} - \sigma_\xi)$. This reduces D to a diagonal matrix and matrix inversion reduces to a scalar inversion. The above derivation is strictly valid for the Euler equations. The contribution of viscous fluxes can be approximated by adding a scalar term to the spectral radius (e.g. σ_ϵ and σ_ϵ^v), where

$$\sigma_\xi = |U_\xi| + c + \frac{2\mu(\xi_x^2 + \xi_y^2 + \xi_z^2)}{\rho} \tag{2.57}$$

The approximation of the LHS results in factorization errors. To reduce these errors and to fully improve time accuracy, OverTURNS performs Newton sub-iterations at each physical time step. Details are provided in section 2.6.6.

2.6.5 DADI

Another method of inverting the LHS is by using ADI. The diagonalized algorithm developed by Pulliam and Chaussee [72] is used for implicit time inversion in small scale rotor cases. The equation is rewritten by Beam and Warming [73] and is first order implicit in time:

$$[I + \Delta t(\partial_\xi \tilde{A} + \partial_\eta \tilde{B} + \partial_\zeta \tilde{C})]\tilde{Q} \simeq [I + \Delta t\partial_\xi \tilde{A}][I + \Delta t\partial_\eta \tilde{B}][I + \Delta t\partial_\zeta \tilde{C}] \tag{2.58}$$

The original inversion has now been replaced by three less expensive inversions. The computational expense can be further reduced by using the fact that the inviscid

components of the flux jacobians can be diagonalized:

$$\lambda_\xi = T_\xi^{-1} \hat{A}_i T_\xi \tag{2.59}$$

$$\lambda_\eta = T_\eta^{-1} \hat{B}_i T_\eta \tag{2.60}$$

$$\lambda_\zeta = T_\zeta^{-1} \hat{C}_i T_\zeta \tag{2.61}$$

where T_ξ is the set of left eigenvectors of matrix $\hat{A}_i$ and T_ξ^{-1} is the set of right eigenvectors of matrix $\hat{A}_i$. Similarly, T_η and T_ζ are matrices corresponding to the matrices $\hat{B}_i$ and $\hat{C}_i$ respectively. The set of eigenvalues of matrix $\hat{A}_i$ are given in matrix λ_ξ. Similarly λ_η and λ_ζ contain eigenvalues of $\hat{B}_i$ and $\hat{C}_i$.

Substituting this diagonalized form of the flux jacobians and ignoring the viscous contribution on the LHS into the discretized Navier-Stokes equation, one can write eqn. 2.58 as:

$$[T_\xi T^{-1} + h(T_\xi \lambda_\xi T_\xi^{-1})][T_\eta T^{-1} + h(T_\eta \lambda_\eta T_\eta^{-1})][T_\zeta T^{-1} + h(T_\zeta \lambda_\zeta T_\zeta^{-1})]\Delta \hat{Q}^n = \Delta t[RHS^n]$$

$$\tag{2.62}$$

Assuming that the eigenvectors of the inviscid fux jacobians are locally constant in the local neighborhood of (j,k,l), the above equation can be rewritten as:

$$T_\xi[I + \Delta t \delta_\xi \lambda_\xi]T_\xi^{-1} T_\eta[I + \Delta t \delta_\eta \lambda_\eta]T_\eta^{-1} T_\zeta[I + \Delta t \delta_\zeta \lambda_\zeta]T_\zeta^{-1} = \Delta t[RHS^n] \tag{2.63}$$

The diagonal algorithm reduces the block tridiagonal inversion to 5×5 matrix multiplications and scalar tridiagonal inversions. The diagonal algorithm described above is rigorously valid for the Euler equations. This is because we have neglected the implicit linearization of the viscous fluxes. The viscous flux Jacobians are not simultaneously diagonalizable with the inviscid flux Jacobians and therefore an ap-

55

proximation to the viscous Jacobian eigenvalues have to be used and is given by:

$$\lambda_v(\xi) = \overline{\mu J^{-1}(\xi_x^2 + \xi_y^2 + \xi_z^2)} J\rho^{-1} \tag{2.64}$$

$$\lambda_v(\eta) = \overline{\mu J^{-1}(\eta_x^2 + \eta_y^2 + \eta_z^2)} J\rho^{-1} \tag{2.65}$$

$$\lambda_v(\zeta) = \overline{\mu J^{-1}(\zeta_x^2 + \zeta_y^2 + \zeta_z^2)} J\rho^{-1} \tag{2.66}$$

The new form of diagonal algorithm is given by:

$$T_\xi[I+\Delta t(\delta_\xi\lambda_\xi-\delta_{\xi\xi}\lambda_v(\xi))]T_\xi^{-1}T_\eta[I+\Delta t(\delta_\eta\lambda_\eta-\delta_{\eta\eta}\lambda_v(\eta))]T_\eta^{-1}T_\zeta[I+\Delta t(\delta_\zeta\lambda_\zeta-\delta_{\zeta\zeta}\lambda_v(\zeta))]T_\zeta^{-1}\Delta\hat{Q}_n = \Delta t|$$

$$\tag{2.67}$$

2.6.6   Dual time stepping

Approximation of the LHS results in factorization errors. To remove these factorization errors and to recover time accuracy, one must perform sub-iterations at each physical time step. To carry out these iterations, eqn. 2.36 can be modified to consider a term that also contains a fictitious pseudo time, τ:

$$\frac{\partial\tilde{Q}}{\partial\tau} + \frac{\partial\tilde{Q}}{\partial t} + \frac{\partial\tilde{F}}{\partial\xi} + \frac{\partial\tilde{G}}{\partial\eta} + \frac{\partial\tilde{H}}{\partial\zeta} = \tilde{S} \tag{2.68}$$

Convergence of the pseudo-time (sub-iterations) at each physical time step is important for obtaining an accurate transient solution. Discretizing eqn. 2.36 with first order finite difference for both artificial and physical time results in

$$\frac{\partial\tilde{Q}^{k+1}-\tilde{Q}^k}{\partial\tau} + \frac{\partial\tilde{Q}^{k+1}-\tilde{Q}^n}{\partial t} + \frac{\partial\tilde{F}^{k+1}}{\partial\xi} + \frac{\partial\tilde{G}^{k+1}}{\partial\eta} + \frac{\partial\tilde{H}^{k+1}}{\partial\zeta} = \tilde{S}^{k+1} \tag{2.69}$$

where k is the pseudo-iteration counter and n is is the time step counter. After linearization one gets:

$$\left[\frac{1}{\Delta\tau} + \frac{1}{\Delta t} + \delta_\xi \tilde{A}^k + \delta_\eta \tilde{B}^k + \delta_\zeta \tilde{C}^k \right] \Delta Q^k = - \left[\delta_\xi \tilde{F}^k + \delta_\eta \tilde{G}^k + \delta_\zeta \tilde{H}^k - \tilde{S}^k + \frac{Q^k - Q^n}{\Delta t} \right]$$

(2.70)

Defining $h = \frac{\Delta t}{1 + \frac{\Delta t}{\Delta\tau}}$ and rearranging

$$\left[I + h(\delta_\xi \tilde{A}^k + \delta_\eta \tilde{B}^k + \delta_\zeta \tilde{C}^k) \right] \Delta Q^k = -h \left[\delta_\xi \tilde{F}^k + \delta_\eta \tilde{G}^k + \delta_\zeta \tilde{H}^k - \tilde{S}^k + \frac{Q^k - Q^n}{\Delta t} \right]$$

(2.71)

The above equation has similar form as eqn. 2.50 and therefore can be solved either using LUSGS or DADI scheme. The unsteady residual at each time step is given by:

$$\delta_\xi \tilde{F}^k + \delta_\eta \tilde{G}^k + \delta_\zeta \tilde{H}^k - \tilde{S}^k + \frac{\tilde{Q}^k - \tilde{Q}^n}{\Delta t}$$

(2.72)

This term should approach zero as the solution converges during the sub-iterations. Typically, a drop in the unsteady residual on the order of one to two orders of magnitude may be considered to be sufficient to ensure that the iteration error is less than the other remaining discretization errors. If the pseudo time size is made very large τ, then $h \to \infty$ and we obtain a Newton sub-iteration scheme. Furthermore, if one doesnt do any sub-iterations then one recovers the traditional Euler implicit method described in eqn. 2.50. Similarly dual time-stepping can be applied with 2nd order backward difference in time (BDF2), by substituting $\delta_t \tilde{Q}^{k+1} = \frac{3\tilde{Q}^{k+1} - \tilde{Q}^n + 4\tilde{Q}^{n-1}}{2\Delta t}$

2.6.7   Preconditioning for Low Mach numbers

The small scale and subscale rotors studied in this work are both operating under a tip Mach number of 0.3. In these low subsonic flow regimes, a compressible RANS methodology shows poor convergence rate to a steady state or within a time step for unsteady flows. The difficulty in convergence arises from the spread in the characteristic wave speeds/eigenvalues, (e.g. $u + c$, $u - c$, u for a 1-D system) of the system of equations (where u is the total flow speed and c is the speed of sound). The time step chosen for the stability is inversely proportion to the largest eigenvalue of the system. For low Mach number flows, it can be approximated to be the speed of sound c. However, the slowest waves are convected at a speed u that is much smaller than c. This implies that these waves do not change much over a time step and require many more time steps to reach a steady state. This necessiates the use of low Mach preconditioning.

Another issue with compressible flow solvers for low Mach numbers is that they suffer from solution inaccuracy. At low Mach numbers, the Roe flux difference splitting causes an excess of artificial viscosity leading to excess dissipation. Roe's scheme is described in section 2.6.1. It can be shown that the dissipation caused by Roe's scheme is proportional to $|\tilde{A}|$, while the fluxes are proportional to the Roe-averaged Jacobian matrix $\tilde{A}$. After manipulating terms of $|\tilde{A}|$, $\tilde{A}$ in one-dimension for low Mach numbers ($M \rightarrow 0$), along with the velocity and density of order 1, one obtains:

$$\tilde{A} = \begin{bmatrix} 0 & O(1) & 0 \\ O(1) & O(1) & O(1) \\ O(\frac{1}{M^2}) & O(\frac{1}{M^2}) & O(1) \end{bmatrix} \qquad (2.73)$$

$$|\tilde{A}| = \begin{bmatrix} O(1) & O(M) & O(M) \\ O(\frac{1}{M}) & O(\frac{1}{M}) & O(M) \\ O(\frac{1}{M}) & O(\frac{1}{M}) & O(\frac{1}{M}) \end{bmatrix} \qquad (2.74)$$

Notice that several terms in $\tilde{A}$ have different order of Mach number compared to $|\tilde{A}|$ (evident from momentum equation, where $\tilde{A}$ has $O(1)$ and $|\tilde{A}|$ has $O(\frac{1}{M})$ and the dissipation terms in energy are too small and of the order $O(\frac{1}{M^2})$ for low Mach number flows). This difference in order of Mach number leads to solution inaccuracy.

The issues of poor convergence and solution inaccuracy for compressible flow solvers at low subsonic Mach numbers as described above can be overcome by using the preconditioning method developed by Turkel [76] and incorporating it in the dual-time algorithm. The psuedo-time term in eqn 2.68 is written in terms of the primitive variable vector, $\tilde{Q}_p$, and the preconditioning matrix, Γ_p, and is given by:

$$\Gamma_p \frac{\partial \tilde{Q}_p}{\partial \tau} + \frac{\partial \tilde{Q}}{\partial t} + \frac{\partial \tilde{F}}{\partial \xi} + \frac{\partial \tilde{G}}{\partial \eta} + \frac{\partial \tilde{H}}{\partial \zeta} = \tilde{S} \qquad (2.75)$$

Primitive variable vector, $\tilde{Q}_p$ is given by $\frac{(p,u,v,w,T)}{J}$, where p is the pressure, u, v and w are velocity components in x, y and z directions, respectively and T is the temperature. The preconditioning matrix, Γ_p is defined as:

59

$$
\Gamma_{\mathrm{p}} =
\begin{bmatrix}
\rho'_p & 0 & 0 & 0 & \rho_T \\[6pt]
u\rho'_p & \rho & 0 & 0 & u\rho_T \\[6pt]
v\rho'_p & 0 & \rho & 0 & v\rho_T \\[6pt]
w\rho'_p & 0 & 0 & \rho & w\rho_T \\[6pt]
(\rho h_p + h_0\rho'_p - 1) & \rho u & \rho v & \rho v & \rho h_T + h_0\rho_T
\end{bmatrix}
\tag{2.76}
$$

where $\rho'_p = \frac{1}{\epsilon_p a^2}$, a is the speed of sound, h is the enthalpy and h_0 is the stagnation enthalpy. Here $\epsilon_p = \frac{M_p^2}{1+(\gamma-1)M_p^2}$ and M_p is the preconditioning Mach number, which is typically chosen to be a value close to the freestream Mach number.

Discretizing eqn. 2.75 with first order finite difference in time for both the artifical and the physical time and linearizing with primitive variables gives:

$$
\left[\frac{\Gamma_p}{\Delta\tau} + \frac{\Gamma_e}{\Delta t} + \delta_\xi\tilde{A}_p^{\ k} + \delta_\eta\tilde{B}_p^{\ k} + \delta_\zeta\tilde{C}_p^{\ k}\right]\Delta\tilde{Q}_p^k = -\left[\delta_\xi\tilde{F}^k + \delta_\eta\tilde{G}^k + \delta_\zeta\tilde{H}^k - \tilde{S}^k + \frac{Q^k - Q^n}{\Delta t}\right]
$$
$$
\tag{2.77}
$$

where $\tilde{A}_p^{\ k}$, $\tilde{B}_p^{\ k}$ and $\tilde{C}_p^{\ k}$ are flux Jacobians with respect $\tilde{Q}_p$ and $\Gamma_e = \frac{\partial Q}{\partial Q_p}$.

The psuedo and physical time derivative terms are combined into a single matrix in the LHS and this results in:

$$
\left[S_p + \Delta\tau(\delta_\xi\tilde{A}_p^{\ k} + \delta_\eta\tilde{B}_p^{\ k} + \delta_\zeta\tilde{C}_p^{\ k})\right] = \Delta\tau\left[\delta_\xi\tilde{F}^k + \delta_\eta\tilde{G}^k + \delta_\zeta\tilde{H}^k - \tilde{S}^k + \frac{Q^k - Q^n}{\Delta t}\right] = R_k
$$

Multiplying through by $\Gamma_e S_p^{-1}$ and converting back to the conservative system, one obtains:

$$
[I + \Delta\tau\Gamma_e S_p^{-1}\delta_\xi\tilde{A}^k + \Delta\tau\Gamma_e S_p^{-1}\delta_\eta\tilde{B}^k + \Delta\tau\Gamma_e S_p^{-1}\delta_\zeta\tilde{C}^k]\Delta\tilde{Q}^k = \Gamma_e S_p^{-1} R^k \tag{2.78}
$$

Applying approximate factorization,

$$[I + \Delta\tau\Gamma_e S_p^{-1}\tilde{A}^k\delta_\xi] + [I + \Delta\tau\Gamma_e S_p^{-1}\tilde{A}^k\delta_\xi] + [I + \Delta\tau\Gamma_e S_p^{-1}\tilde{A}^k\delta_\xi]\Delta\tilde{Q}^k =$$

$$\Gamma_e S_p^{-1}R^k \quad (2.79)$$

Now the scheme can be diagonalized similar to eqn. 2.67 to obtain:

$$\Gamma_e X_\xi[I + \Delta\tau\delta_\xi\tilde{\lambda}\xi]\lambda_\xi^{-1}\lambda_\eta[I + \Delta\tau\delta_\eta\tilde{\lambda}\eta]\lambda_\eta^{-1}\lambda_\xi[I +$$

$$\Delta\tau\delta_\zeta\tilde{\lambda}\zeta]\lambda_\zeta^{-1}\Gamma_e^{-1}\Delta\tilde{Q}^k = \Gamma_e S_p^{-1}R^k \quad (2.80)$$

where X_ξ and $\tilde{\lambda}_\xi$ are respectively, the eigenvector matrix and the eigenvalue matrix of $S_p^{-1}\tilde{A}_p$. The eigenvalue matrix $\tilde{\lambda}_\xi$ is given by:

$$\begin{bmatrix} \lambda_1 & 0 & 0 & 0 & 0 \\ 0 & \lambda_2 & 0 & 0 & 0 \\ 0 & 0 & \lambda_3 & 0 & 0 \\ 0 & 0 & 0 & \lambda_4 & 0 \\ 0 & 0 & 0 & 0 & \lambda_5 \end{bmatrix} \quad (2.81)$$

$$\lambda_{1,2,3} = bU \quad (2.82)$$

$$\lambda_{4,5} = \frac{b}{2}\left[U(1 + \beta') \pm \sqrt{U^2(1 - \beta')^2 + 4a^2\beta'}\right] \quad (2.83)$$

Here $\beta'_p = \frac{M_p^2}{b - (b-1)M_p^2}$, a is the speed of sound and $b = \frac{\frac{\Delta t}{\Delta\tau}}{1 + \frac{\Delta t}{\Delta\tau}}$ The values of M_p^2 and b control the behavior of the preconditioner. The parameter b switches the

behavior of preconditioner from unsteady to steady. For steady flows, $b = 1$ and $\beta' = M_p^2$. Using $M_p = 1$ switches the preconditioner off. The small-scale rotor runs used a β' value equal to the hover Mach number and the sub-scale rotor runs used a β' value equal to the local Mach number. This reduces the spread of the eigenvalues for low Mach numbers and results in an improved convergence using preconditioning. The characteristic boundary conditions need to be modified as well based on the modified eigenvalues.

Preconditioning modifies the Roe's flux scheme to:

$$F(q^L, q^R) = \frac{F(q^L) + F(q^R)}{2} - P^{-1}|P\tilde{A}(q^L, q^R)|\frac{q^R - q^L}{2} \qquad (2.84)$$

where $P = \Gamma_e S_p^{-1}$. The dissipation term for the scheme is now proportional to $P^{-1}|P\tilde{A}|$. In the limits of low Mach number, the order of terms as a function of Mach number can be written as:

$$\text{P}^{-1}|\text{P}\tilde{\text{A}}| = \begin{bmatrix} O(1) & O(1) & 0 \\ O(1) & O(1) & O(1) \\ O(\frac{1}{M^2}) & O(\frac{1}{M^2}) & O(\frac{1}{M^2}) \end{bmatrix} \qquad (2.85)$$

This order of terms is similar to the one for the flux Jacobian matrix (eqn.2.54). This characteristic of the dissipation matrix keeps the terms bounded improving the solution accuracy at low Mach numbers.

2.7 Turbulence Modeling

One approach to turbulence closure of the RANS equations is to solve six additional transport equations, one for each of the stress tensor components, along with an equation for the energy dissipation rate. These models are categorized as Reynolds Stress Models (RSM) [77, 78]. Although Reynolds stress models adopt the most physically realistic approach to turbulence modeling, they are expensive and suffer from issues of robustness and convergence. A more common approach to turbulence modeling is based on the use of the Boussinesq eddy viscosity hypothesis, which relates the Reynolds stress tensor to the mean strain rate as follows:

$$(\overline{\tau_{ij}})_{turb} = -\rho \overline{u_i u_j} = \frac{2}{3} \bar{\rho} k \delta_{ij} - \mu_t \left[\left(\frac{\partial \overline{u_i}}{\partial x_j} + \frac{\partial \overline{u_i}}{\partial x_j} \right) - \frac{2}{3} \frac{\partial \overline{u_k}}{\partial x_k} \delta_{ij} \right] \qquad (2.86)$$

where, k is the turbulent kinetic energy. With this assumption,

$$(\overline{\tau_{ij}})_{total} = \frac{2}{3} \bar{\rho} k \delta_{ij} - (\mu + \mu_t) \left[\left(\frac{\partial \overline{u_i}}{\partial x_j} + \frac{\partial \overline{u_i}}{\partial x_j} \right) - \frac{2}{3} \frac{\partial \overline{u_k}}{\partial x_k} \delta_{ij} \right] \qquad (2.87)$$

2.7.1 Spallart Allmaras (S–A) Turbulence Model with Rotational Correction

In the Spalart Allmaras turbulence model, the Reynolds stresses are related to the mean strain by the isotropic relation, $< u_i' u_j' > = -2\nu_t S_{ij}$, where ν_t is the turbulent eddy viscosity, that is obtained by solving a PDE for a related variable $\tilde{\nu}$.

$$\frac{\partial \tilde{\nu}}{\partial t} = \frac{1}{\sigma}[\nabla.((\tilde{\nu} + \nu)\nabla\tilde{\nu}) + c_{b2}(\nabla\tilde{\nu})^2] + c_{b1}\tilde{S}\tilde{\nu} - c_{w1}f_w\left[\frac{\tilde{\nu}}{d}\right]^2 \qquad (2.88)$$

The eddy viscosity ν_t is related to $\tilde{\nu}$ by the relation,

$$\nu_t = \bar{\nu}f_{v1} \qquad (2.89)$$

where f_{v1} is a function of $\tilde{\nu}$ and the molecular viscosity ν and is defined by:

$$f_{v1} = \frac{\chi^3}{\chi^3 + c_{v1}^3} \qquad (2.90)$$

where $\chi = \frac{\tilde{\nu}}{\nu}$. The function f_{v1} is a damping function that attenuates the eddy viscosity in the viscous sub-layer. This means that $\tilde{\nu} \approx \nu_t$ everywhere except in the sub-layer, where an attempt is made at ensuring a linear profile with the correct log-layer profile. The left hand side of 2.88 accounts for the convection of the working variable $(\tilde{\nu})$ at the mean flow velocity $\mathbf{V}$. The first term on the right hand side represents diffusion, followed by the production and destruction terms. The production is given by:

$$\tilde{S} = S + \frac{\tilde{\nu}}{\kappa^2 d^2}f_{v2} \qquad (2.91)$$

$$S = |\omega| = \Delta \times V \qquad (2.92)$$

$$f_{v2} = 1 - \frac{\chi}{1 + \chi f_{v1}} \qquad (2.93)$$

The destruction term is given by:

$$f_w = g\left[\frac{1 + c_{w3}^6}{g^6 + c_{w3}^6}\right]^{\frac{1}{6}} \qquad (2.94)$$

where g is given by:

$$g = r + c_{w2}(r^6 - r) \qquad (2.95)$$

and r is given by:

$$r = min \left(\frac{\tilde{\nu}}{\tilde{S}\kappa^2 d^2}, 10.0 \right) \quad (2.96)$$

where d is the distance to the nearest wall. The various constants in the turbulence model are:

$$\sigma = \frac{2}{3}$$

$$c_{b1} = 0.1355$$

$$c_{b2} = 0.622$$

$$c_{w1} = \frac{c_{b1}}{\kappa^2} + \frac{1 + c_{b2}}{\sigma}$$

$$c_{w2} = 0.3$$

$$c_{w3} = 2.0$$

$$\kappa = 0.41$$

$$(2.97)$$

2.7.1.1 Implementation of rotational correction

The production term as shown in the S–A model is based on the magnitude of the vorticity vector. This formulation performs well for wall bounded flows. However, vortex cores behave like a solid body with pure rotation that supresses turbulence [64]. The vortex core has low strain rates but high vorticity. A modification to the production term first introduced by the in Spalart et al. [65] takes

care of the effects of pure rotation in the vortex core by using:

$$S = |\omega| + 2min(0, |D| - |\omega|), \tag{2.98}$$
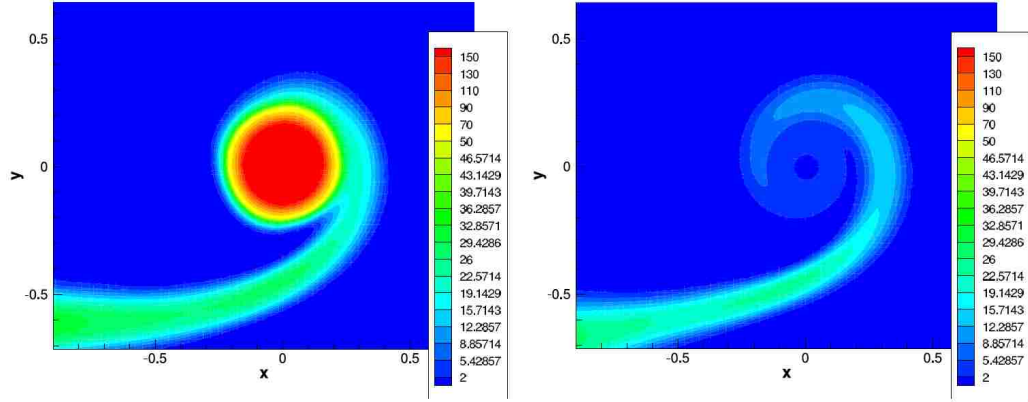
(a) S-A model without rotational correction.   (b) S-A model with rotational correction.

Figure 2.4: Eddy viscosity contour levels inside a vortex core (Reproduced from Karthik [40]).

The above equation shows that the production of eddy viscosity depends on relative magnitudes of vorticity and strain rate tensors. This modification supresses the turbulent production in tip vortices where vorticity is much larger than the strain-rate. Near to the wall, in thin shear layers vorticity and strain rate are closer in magnitude. This implies that the production term returns back to its original form as proposed in the S–A model. Figures. 2.4(a) and (b) show the difference in the turbulence levels in the core of the tip vortex with and without this modification to the production term in the S–A model. It can be clearly observed that the rotational correction reduces the eddy viscosity levels in the vortex core.

2.7.1.2   Initial and Boundary Conditions for Turbulence Modeling

The initial and freestream values of $\tilde{\nu}$ is set nominally to be $\tilde{\nu} = 0.1\nu$. However, this value can be modified if the experiments specify a different freestream value. The farfield boundaries use a characteristic treament depending on the the direction of local velocity vector (ie. $\tilde{\nu}$ is either extrapolated from the interior or set to the freestream value). At solid surfaces, $\tilde{\nu}$ is set to zero and this satisfies the Reynolds stress boundary condition. The wake cuts use a high order averaging:

$$q_{j,bc} = \frac{1}{6}(-q_{j-2} + 4q_{j-1} + 4q_{j+1} - q_{j+2})$$ (2.99)

2.8   Boundary Conditions (BC)

A Navier Stokes based solver can employ various types of boundary conditions. There can be physical boundaries (eg. wall bc), numerical boundaries (eg. wake cut bc), or artificial boundaries (eg. point-sink bc). Some of these boundary conditions have been utilized as a part of this work and are described below. There are several other boundary conditions that exist for the different cases in the OverTURNS solver. Figure 2.5 shows a 2-D cross-cut of the blade, a top view of the cylindrical background mesh, in which the blade mesh is embedded, and an azimuthal view of the cylindrical mesh; respectively highlighting the various boundary conditions used in this work.
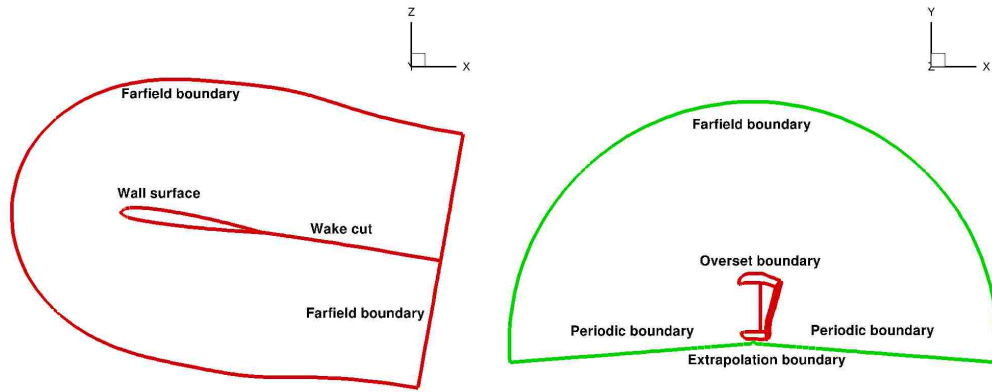
(a) 2-D blade mesh view at a spanwise loca- (b) Top view of background and blade mesh.
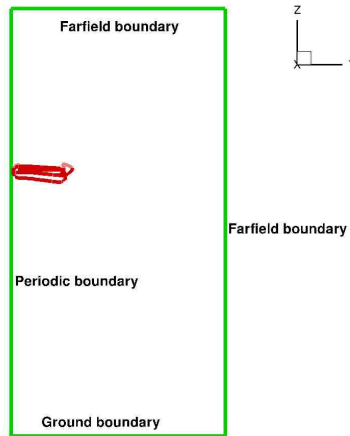
tion.

(c) Side view of background and blade mesh.

Figure 2.5: A sample blade and body mesh system describing various boundary conditions.

2.8.1 Farfield boundary conditions

The farfield boundaries should be placed far enough away from physical bodies such that there are no spurious wave reflections occuring at the boundary where prevailing conditions are very close to freestream. Based on the direction of the velocity vector and the magnitude of the sonic velocity, the Reimann invariants are extrap-

olated either from the interior or from the freestream. The boundaries are typically placed at approximately 20-30 chord lengths away from body surfaces for fixed wing computations. This allows for stronger gradients to diminish while approaching the boundary. Mesh stretching at the boundaries also helps in numericallly dissipating strong flow gradients in the vicinity of the boundary (e.g. slipstream dividing the flow inside and outside of the rotor wake).

2.8.2   Wall boundary condition

At the solid wall, the density is extrapolated from the interior of the domain. For viscous calculations, the no-slip condition requires that the velocity at the wall equals the grid velocity. The pressure (p) is then obtained from the normal momentum equation that is given by:

$$p_\xi(\nabla\xi.\nabla\zeta)+p_\eta(\nabla\eta.\nabla\zeta)+p_\zeta(\nabla\zeta.\nabla\zeta) = -\rho U(\nabla\eta.\frac{\partial Q}{\partial\xi})-\rho V(\nabla\zeta.\frac{\partial Q}{\partial\eta})-\rho W(\nabla\zeta.\frac{\partial Q}{\partial\zeta})$$

(2.100)

In the case of an inviscid wall, the contravariant velocity components (U; V; W) are extrapolated to the surface. In order to satisfy the no-penetration condition, the contravariant component of velocity in the wallnormal direction is set such that it (Q) equals the surface velocity in the wall normal direction.

2.8.3   Wake cut boundary condition

In a C- topology mesh, the wake cut starts to appear adjacent to the solid wall where the grid planes collapse on each other. The solution values along the collapsed cells are obtained by a simple averaging of the solution from either side of the wake cut. A wake-cut boundary also appears in a C-O topology blade mesh, on the collapsed planes at the root and tip.

2.8.4   Periodic boundary condition

The hover simulations in this work assume periodicity for the wake capturing meshes. The size of the period in azimuthal space is dependent on the number of blades in the rotor. For example, for a two bladed rotor, the azimuthal period is 180°. This allows the simulations to only model one rotor blade. The periodic boundary condition is formulated by creating ghost cells at the boundary, where the vector quantities are prescribed using coordinate rotation and scalar quantities are set to be identical.

2.9   Parallelization

An accurate resolution of the tip vortex formation, evolution and eventual interaction as it approaches towards the ground requires the usage of large mesh sizes. This requires that the large meshes can be divided into smaller sizes or subdomains and the solution can be carried out independently on many processors, making the current problem massively parallel. The process of making the individual subdo-

mains independent of each other in operation is referred as the domain decomposition method. At the same time, the adjacent subdomains need to communicate with each other for exchanging information. Accordingly, the message passing interface system (MPI) has been employed to perform parallel computations and communications between different processors in OverTURNS. The information exchange between adjacent processors is done through an artificial boundary condition.
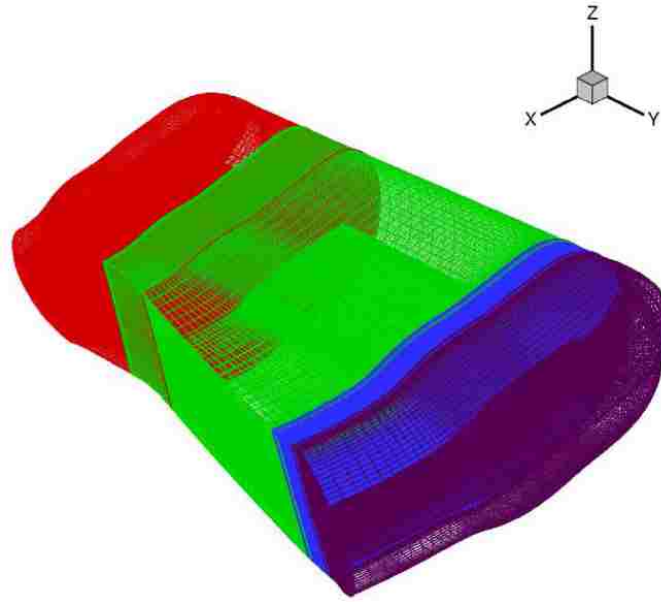
Figure 2.6: Sample domain partitioning for blade mesh in spanwise direction for parallel computation.

The size of the subdomains is kept roughly equal to ensure proper load balancing. The size can be increased or decreased based on the memory of individual processors. In the current work, the size of each subdomain is kept close to 10 Megabytes. The blade meshes are split along the spanwise direction and the background meshes are split in all three directions. Figure 2.6 shows an example of domain partitioning, where the blade mesh is divided into four along the spanwise

direction. Note that, sufficient overlap (3 points on each side of the subdomain) is ensured between the split meshes to maintain the spatial accuracy.

2.10   Overset meshes and Grid Connectivity

The OverTURNS methodology requires the usage of structured meshes. Generally, structured meshes involve less computational storage, are computationally faster and can handle wall boundary layers better than alternative approaches. In a case where different parts of the domain are required to resolve fine flow features while other parts can maintain coarser resolution, one can introduce multiple overset meshes. The alignment and geometry of overset meshes need not be strictly corresponding to each other and this provides a greater flexibility in the mesh generation process, therefore allowing one to have a high grid resolution in regions of interest. The various overset grids need to have an efficient information transfer mechanism/connectivity between them.

The original Implicit Hole Cutting (IHC) method was developed by Lee [79] and was later modified by Lakshminarayan [44] to incorporate more generic boundary conditions and donor search methods. The donor cell search uses the so-called stencil walk procedure by Gupta [80]. The modified IHC method is used in the current work. The principle idea behind the IHC method is that in a given CFD domain consisting of overset meshes, the solution is computed on the grid points that are associated with the smallest cell sizes and interpolated to cells with coarser cell sizes. Using an octree search algorithm, the method parses through every grid cell

in the CFD domain and selects the smallest cell in multiple overlapped regions. The details of the octree algorithm search is described by Jose [81]. The IHC method senses the presence of the wall because of the progressively decreasing cell sizes as the wall/body-surface is approached and the hole is automatically cut around the body at the optimum location.
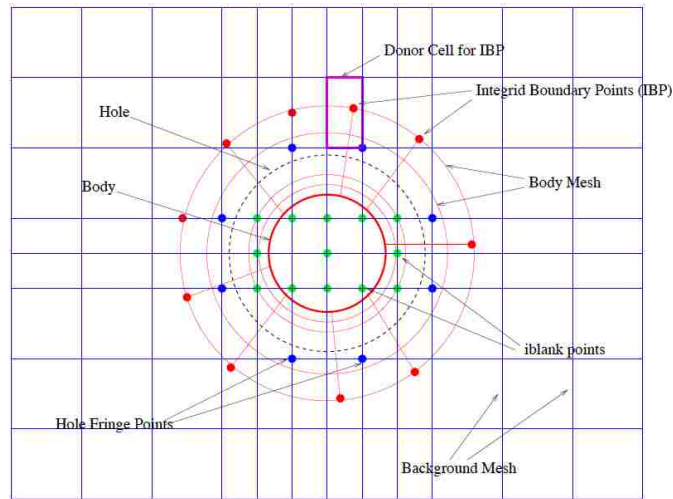
Figure 2.7: Schematic describing the terms involved in the traditional hole cutting problem. Reproduced from Jose et al. [81].

The chimera connectivity methodology involves three main steps: i)hole cutting, ii) identification of hole fringe and chimera boundary points (collectively known as receiver points) and iii) finding donor cells and interpolation factors. To illustrate this, figure 2.7 shows a body mesh embedded in a background mesh. A hole is a region cut out by the body mesh. The points of the background mesh inside this hole region are called hole points. These points are blanked out and do not participate in the solution process. After obtaining the list of hole points, a list of hole fringe points, which require solution information from other grids to serve as boundary

conditions, is extracted. As a next step, a list of chimera boundary points, which are the points on the boundary of one mesh requiring solution information from another mesh is specified by the user. The size of the fringe and chimera boundary layers is a function of the stencil used by the spatial scheme in the simulation. Both the hole fringe points and the chimera boundary points are also referred to as receiver points. These receiver points need their solution values interpolated from donor cells. The location of the receiver point with respect to the donor cell is used to compute the interpolation weightage by using each corner point of the donor cell. The donor cell is indexed by the index of its lower, left corner point. All the other points are refferred to as field points.

An iblank array is further defined corresponding to all the grid points. Iblank array is set as 0 for hole points and as 1 for the field points. Consequently, the flow solver is modified so that the governing equations are not solved at hole points and are solved only at field points. The iblank array is set to have -1 values for the hole fringe/chimera boundary points during implicit inversion and is set to be 1 while calculating the fluxes. This means that these hole fringe/chimera points are blanked out during time inversion. To accomplish this in the solution procedure, a function consisting of the iblank array is multiplied to the time step corresponding to each grid point (for e.g., h in eqn. 2.64). The time step in the LHS of the equation is multiplied by max(iblank, 0) and that in the RHS is multiplied by abs(iblank). As a result of this, the contribution of hole points is blanked out in both the LHS and RHS, while that of the hole fringe and chimera boundary points are blanked out only in the LHS. This prevents the propagation of inaccuracies from the hole

74

points to the flow solution. At the same point where physical boundary conditions are applied, the code also applies the proper interpolation from donor cells to the receiver cells

2.11 Summary of Chapter

Details of the governing equations and their numerical solution methodology in the OverTURNS flow solver were summarized in this chapter. Discussion also included advanced algorithms such as low-Mach preconditioning, detached eddy simulations, and implicit hole cutting that were used in this work. In the next chapter, results will be presented for the micro-scale rotor simulations operating in ground effect using the OVERTURNS flow solver.

Chapter 3

Micro-scale Rotor Modeling

In this chapter, computations are performed on a hovering micro-scale single rotor operating in ground effect (IGE) at various rotor heights above the ground. The performance data is validated with experimental results. Subsequently, detailed analysis of the flow physics of the rotor wake convection and its resulting " interaction with the ground plane is performed.

3.1   Micro-Scale Rotor Configuration
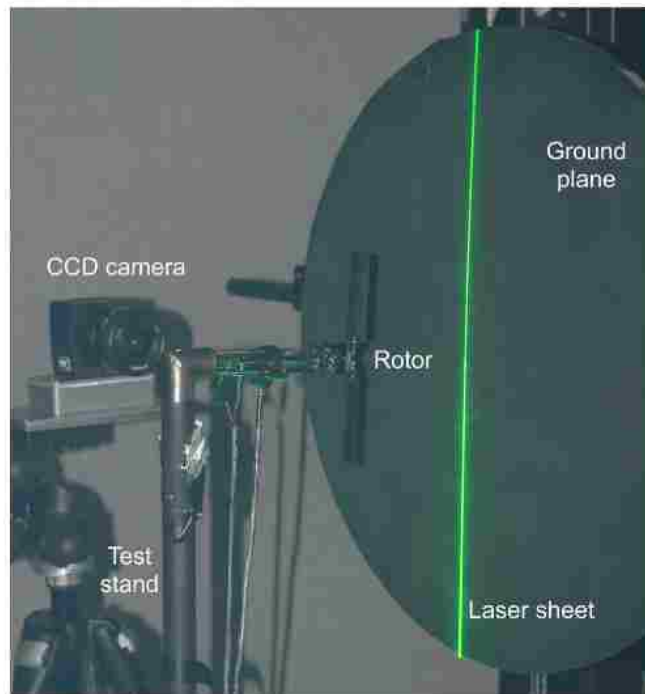
Figure 3.1: Experimental setup of 2-bladed micro-scale rotor of Lee et al.

The experimental setup of Lee et al. [48] shown in fig. 3.1 is used to validate the flow field of a hovering micro-scale rotor in ground effect. The rotor consisted of two untwisted rectangular blades of radius 86 mm. The blades had a circular arc airfoil with 19.6 mm chord (resulting in an aspect ratio of 4.39), 3.7% thickness, and 3.3% camber. The blades were set at a collective pitch of 12°. The experimental results were obtained at a tip Mach number of 0.08, resulting in a root Reynolds number of 6480 and a tip Reynolds number of $32,400$. Experimental results were available for rotor heights varying from 0.25 to 2.5 times the rotor radius.

3.2   Mesh System for Micro-Scale Rotor Modeling

An overset mesh system consisting of a body conforming C-O type blade mesh, a cylindrical main background mesh, cylindrical overset meshes and vortex tracking grids are used in the present study. To save computational costs, only one blade is simulated (implying the use of half of the domain) by using a periodic boundary condition. Simulations are performed for three rotor heights of $0.5R$, $1.0R$ and $1.5R$ above the ground. The implicit hole-cutting technique, developed by Lee [79] and improved by Lakshminarayan [44] (described in section 2) is used to determine the connectivity information between the various overset meshes. The complete mesh described below is for a rotor operation at $1R$ rotor height above the ground.

The blade mesh consists of a body conforming structured curvilinear mesh formed by using a hyperbolic mesh generation technique [84]. In this method, 2D C-type meshes are generated around the airfoil sections and stacked together at
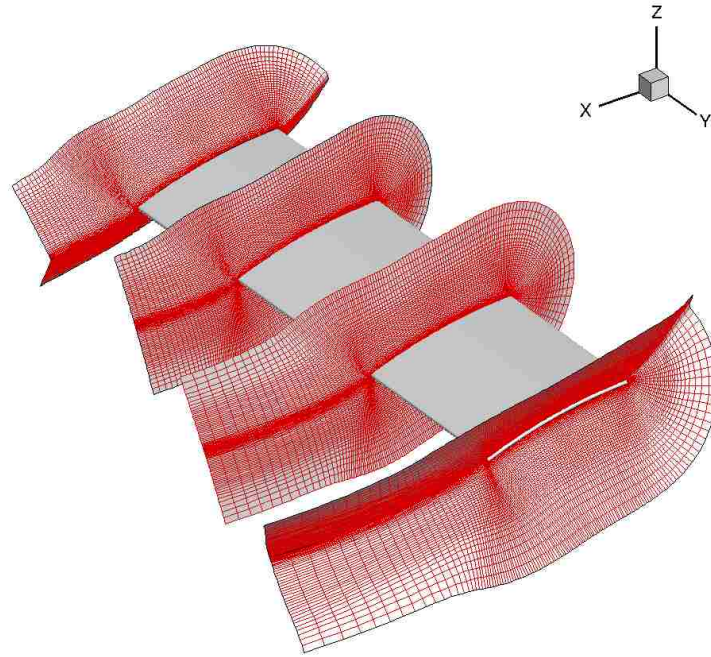
(a) Spanwise stacking of C meshes and collapse of C-O blade mesh at the tip and root

]
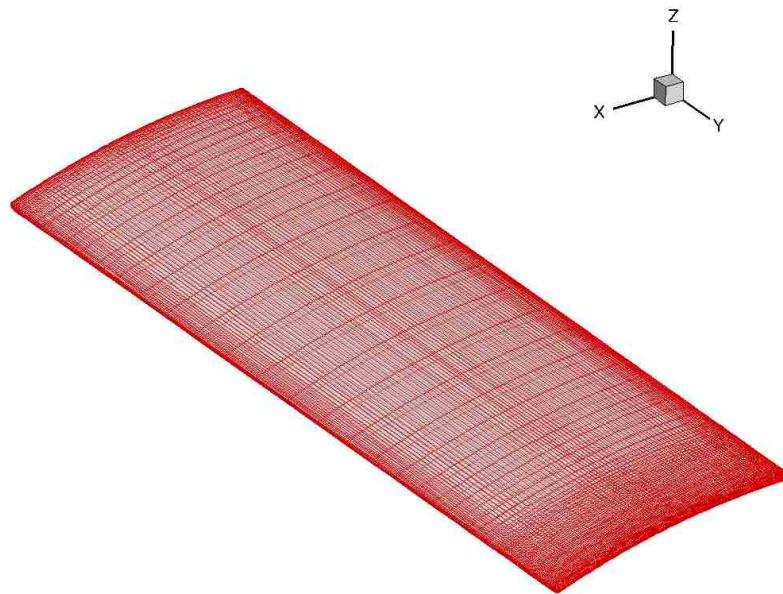
(b) Blade surface

Figure 3.2: Micro-scale rotor blade mesh.

various spanwise locations as seen in fig. 3.2(a). The C-type meshes are free of a geometrical singularity at the trailing edge. The grid clustering at the trailing edge provides good resolution for capturing the shed wake. Also, note the rotation and collapse of the C sections near the root and the tip regions to define a C-O topology. Details of the collapsing technique are described in Duraisamy [40]. One can also observe the blunt leading and trailing edge in the micro-scale rotor blade at the tip region in fig. 3.2(a). The blade surface is seen in fig. 3.2(b). The blade mesh consists of $267 \times 93 \times 50$ points in the streamwise, spanwise and wall normal directions. 187 points are along the airfoil surface in the streamwise direction. A spacing of 5.0×10^4 chords is used in the wall normal direction, which corresponds to $y+$ value of around 1.0.

The blade mesh is overset into a background mesh. The background mesh is a cylindrical Cartesian mesh that consists of identical planes rotated in the azimuthal direction. Each azimuthal plane is spaced at every 1.5^o in azimuth. One such azimuthal plane is shown in fig.3.3(a). Figure 3.3(b) shows the top view of the background mesh to illustrate the various azimuthal planes. The mesh is refined in the regions of interest to capture the convection of the root and tip vortices. The root region is refined from $0.1R$ to $0.22R$ and the tip region is refined from $0.6R$ to $1.6R$. In these most refined regions, the background mesh has a grid spacing of 0.04 chords in both the radial and vertical directions. The mesh extends to $10.0R$ in the radial direction. This distance is chosen to be far enough to prevent any reflections from the farfield boundary. To model the ground plane, the mesh is refined close to the ground smoothly to obtain a $y+$ value of around 1.0. The rotor height is
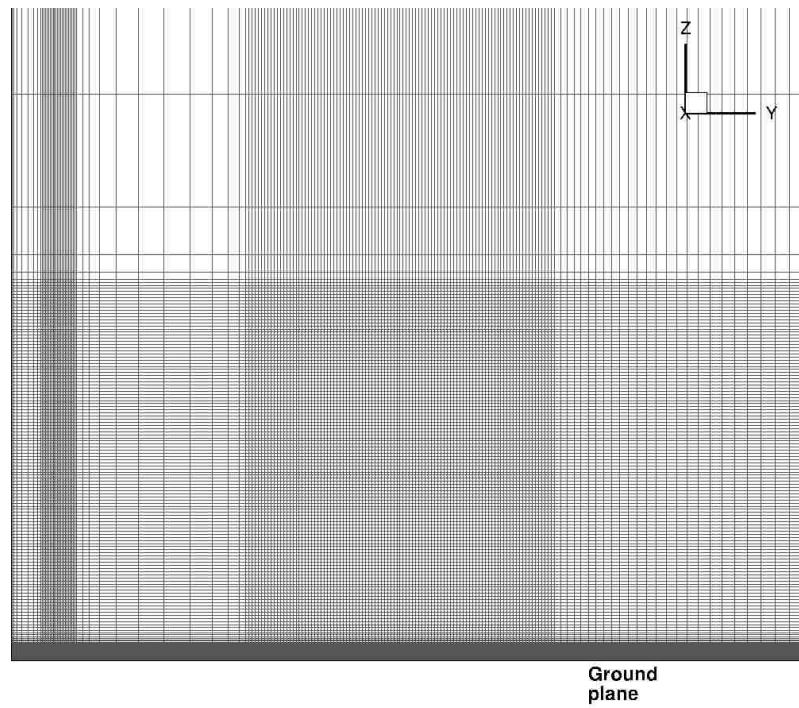
(a) Azimuthal plane
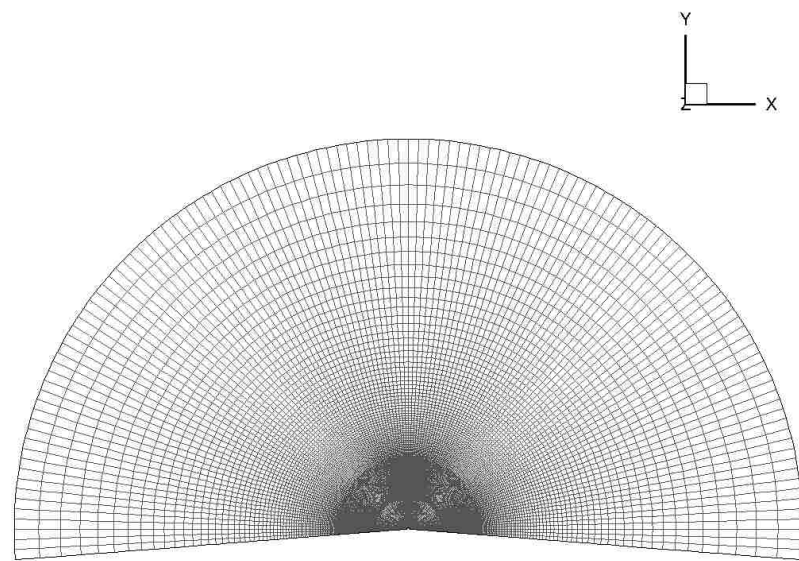
(b) Top view

Figure 3.3: Cylindrical background mesh.
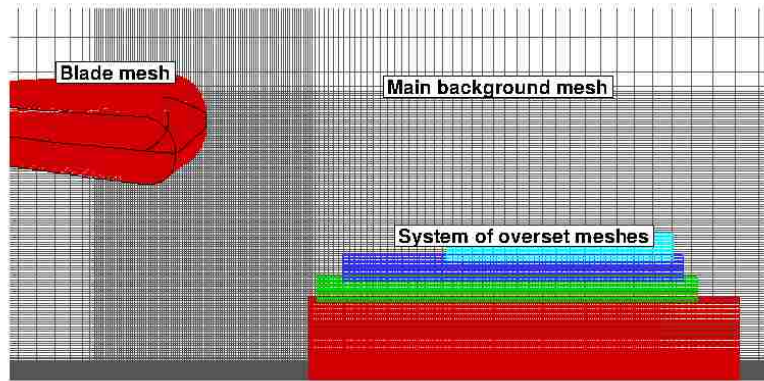
Figure 3.4: Blade mesh, main background mesh, and a system of overset meshes for a rotor placed at $1R$ above the ground.

$1R$ above the ground plane in fig. 3.3(a). The total number of mesh points in the background cylindrical mesh are $127 \times 207 \times 205$.

Initially in this work [85], the grid system consisted of only the blade mesh and a single cylindrical background mesh to simulate the problem. However, this mesh system did not resolve the tip vortices to sufficiently outboard radial locations and therefore, did not capture some of the unsteadiness observed in the experiment. This problem is overcome by using a system of overset cylindrical Cartesian meshes placed near the ground in addition to the blade and the main background meshes. Figure 3.4 shows the blade, the main background and the system of cylindrical overset meshes used in the simulation of a rotor placed at $1R$ above the ground. The overset meshes are laid down in a stair-step manner, with the most refined overset mesh placed at the bottom and the coarsest mesh at the top. This strategy is adopted to limit the cell size disparity between the various overset meshes to less

than a factor of two in the regions of interpolation, and thereby, minimize the errors arising due to these interpolations. Each azimuthal plane is spaced at every 1.0^o for the additional overset cylindrical meshes along with a grid spacing of 0.04 chords in both the radial and vertical directions. These meshes enable the refinement of the mesh system to $3.5R$ in the radial direction. For the overset mesh placed at the ground, the $y+$ value is maintained similar to the background mesh. There is an overlap of atleast three points in the radial and vertical directions between the background and overset meshes to reduce interpolation errors.

In order to efficiently preserve the tip vortex all the way to the ground, additional vortex tracking grids (VTGs) are added into the simulations. Vortex tracking grids have been earlier developed by Lee [79] and and employed by Duraisamy [40] as well. The VTGs are overset onto the main background mesh. VTGs are three dimensional helical meshes, which are generated by azimuthally extruding a 2-D Cartesian plane. Ideally, the 2-D planes should be positioned based on the instantaneous tip vortex trajectory, which are extracted by searching for maximum vorticity magnitude corresponding to the vortex center at different wake ages. However in the current work, a typical instantaneous tip vortex trajectory, shown in figs. 3.5(a) and (b), is seen to have high levels of unsteadiness. If the VTGs are generated based on the instantaneous trajectories (shown in fig. 3.6(a)), the tip vortices are seen to dissipate spuriously due to the lack of smoothness in the azimuthal direction. In order to rectify this issue, the VTGs are generated based on phase-averaged trajectories (shown in figs. 3.5(a) and (b)), which typically show lesser amount of unsteadiness compared to the instantaneous trajectories.
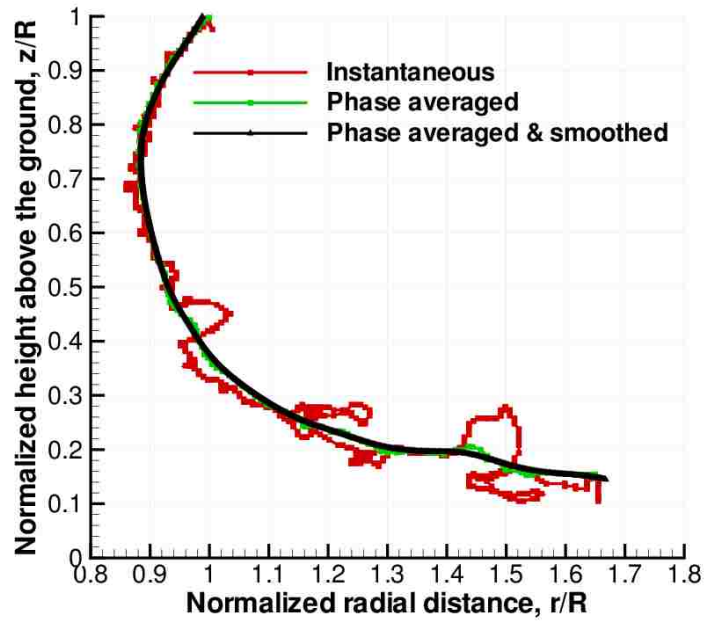
(a) Wake trajectory
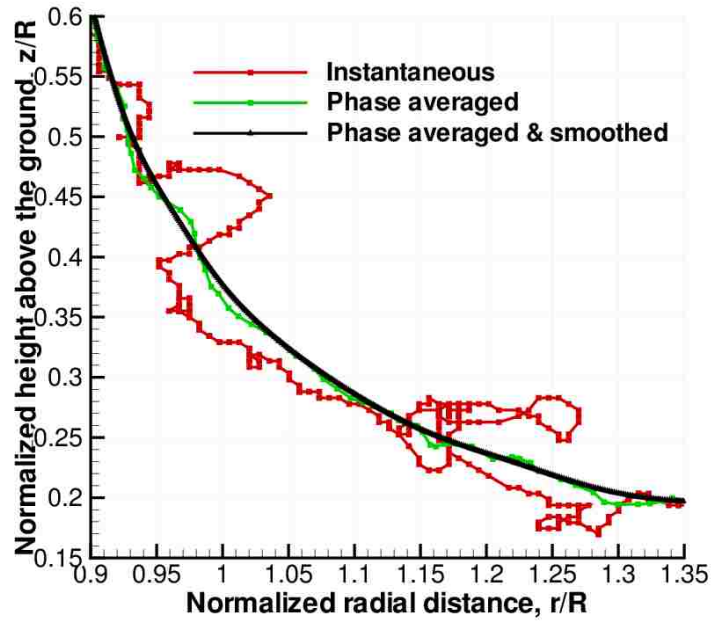
(b) Zoomed in wake trajectory

Figure 3.5: Typical instantaneous, phase-averaged and smoothed trajectories for $h/R = 1.0$.
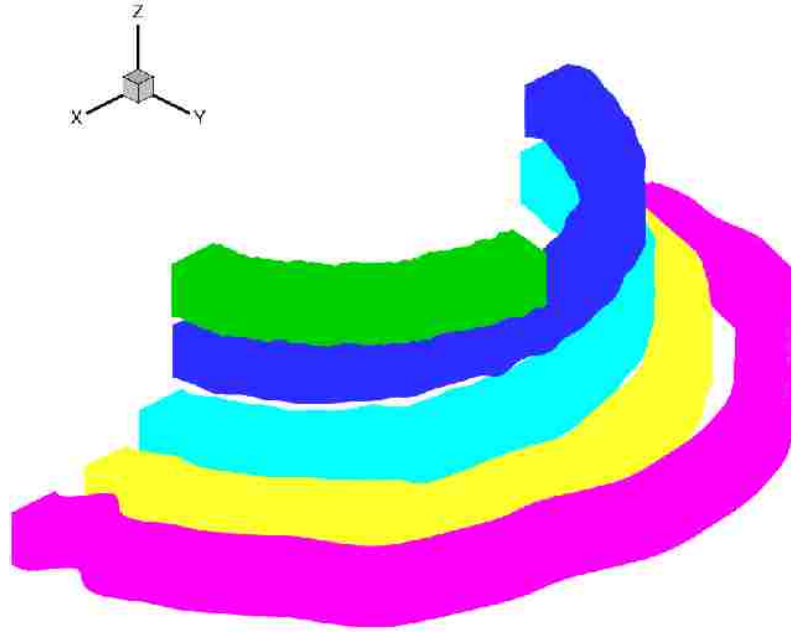
(a) VTG based on instantaneous trajectory
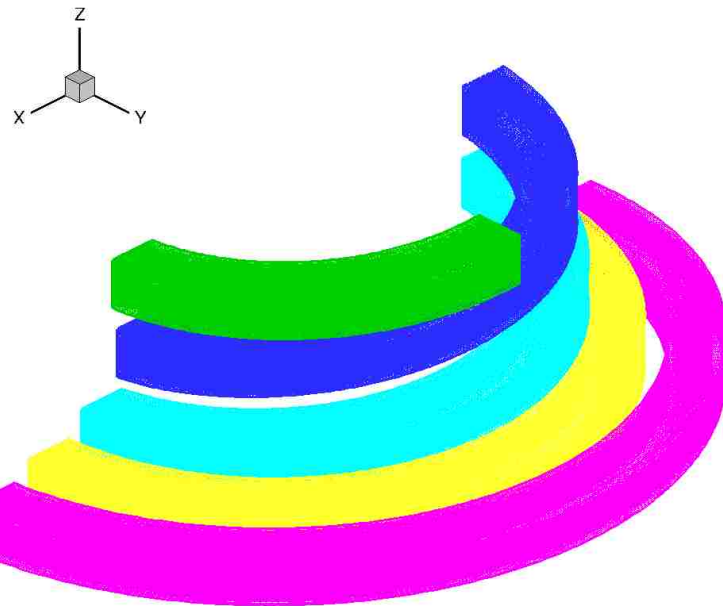
(b) VTG after phase-averaging and smoothing

Figure 3.6: Isometric view of vortex tracking grid for $h/R = 1.0$.
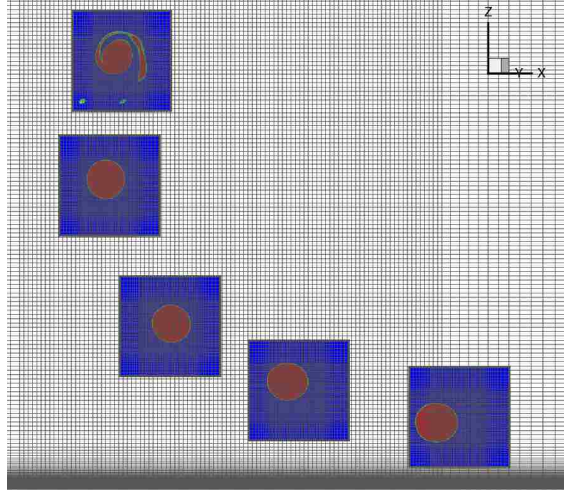
(a) 2-D planar cross sections of VTG with vortic-

ity contours from the cap tured tip vortices
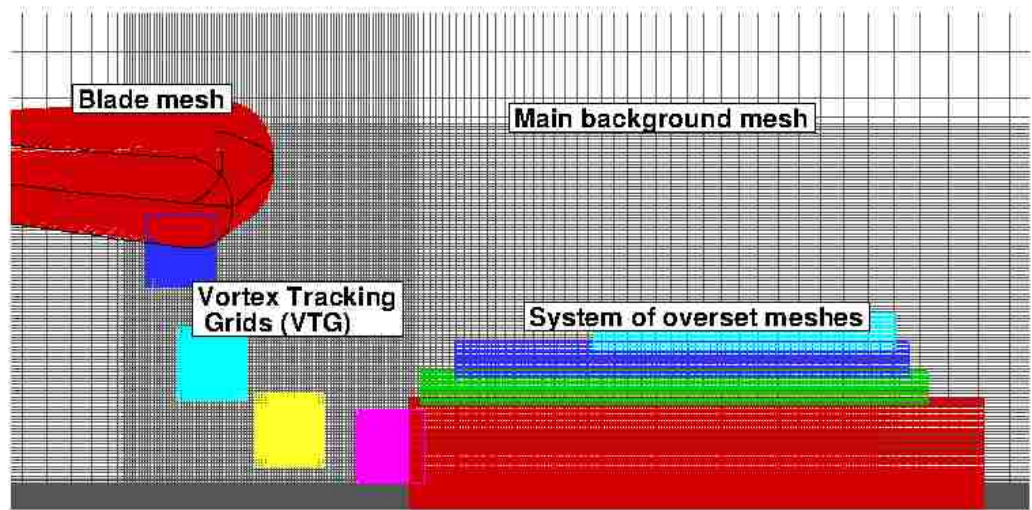
(b) Complete mesh system

Figure 3.7: Mesh system for $h/R = 1.0$.

In fact, even the phase-averaged trajectories have some amount of wiggles

when looked at closer, see fig. 3.5(b), and therefore additional smoothing of these

trajectories is done by using a Laplacian based operator. The resulting vortex tracking mesh obtained using such a smoothed trajectory is shown in fig. 3.6 and is seen to be much smoother than one based on an instantaneous trajectory. The 2-D planar section of the VTG is a Cartesian mesh with equi-spaced mesh points near the middle, which stretches at the edges to reduce the cell size disparity between the vortex mesh and the main background mesh. The extent of the 2-D plane is calculated by accounting for the expected wandering of the tip vortex. Each 2-D plane in the VTGs has been placed every 0.75^o of the azimuth, i.e. one-half of the azimuthal spacing of the main background mesh. In the most refined regions the VTGs have a grid spacing of 0.01 chords in both the vertical and radial directions. This means that at the cell center, the spacing in the VTG is approximately one-fourth that in the main background mesh. At the edge of the VTG, the cell spacing stretches smoothly to become equal to that in the main background mesh to reduce interpolation errors. The position of a VTG is predetermined by running the simulation without the VTG until the flow is reasonably well developed. Over the VTG mesh is determined the flow from the main background mesh is interpolated onto the VTG mesh and the solver restarts using this new mesh system. The VTGs are adapted after every three revolutions until the tip vortex positions are converged. The vortex positions were fairly converged within one adaptation of the vortex mesh in the current simulations, such that the total number of time steps required for convergence with and without the use of a VTG is not significantly different. Figure 3.7 shows a 2-D planar cross section, highlighting the ability of the VTGs to capture the tip vortices, as well as the complete mesh system.

Table 3.1: Number of points used in various meshes for simulation for a $h/R = 1.5$.

Mesh	Dimensions	Mesh points (in millions)
Blade Mesh	$267 \times 93 \times 50$	1.2
Main Background Mesh	$127 \times 205 \times 305$	7.9
Overset Mesh 1	$187 \times 186 \times 146$	5.1
Overset Mesh 2	$187 \times 111 \times 21$	0.4
Overset Mesh 3	$187 \times 61 \times 20$	0.2
Vortex Tracking Grid	$70 \times 70 \times 1330$	6.5
Total		21.4

Tables 3.1, 3.2 and 3.3 show the total number of mesh points used in the simulation of the three different rotor heights ($h/R = 1.5$, 1.0 and 0.5), respectively.

3.3 Micro-Scale Rotor Setup Parameters and Computational Costs

The micro-scale rotor simulations use the DADI Method [72]. described earlier in Chapter 2. The chosen time-steps correspond to 0.25° of azimuth for all the calculations. The low Mach preconditioning was used with the value of the pseudo-time step size on the order of the actual time step for both convergence and accuracy. The time-step for Newton sub-iterations is chosen to be 0.2. At each time step, 6 sub-iterations are used to remove the linearization errors. Each simulation is run for 18 revolutions to allow the tip vortex trajectory to fully converge. The calculations

Table 3.2: Number of points used in various meshes for simulation for a $h/R = 1.0$.

Mesh	Dimensions	Mesh points (in millions)
Blade Mesh	$267 \times 93 \times 50$	1.2
Main Background Mesh	$127 \times 205 \times 207$	5.4
Overset Mesh 1	$187 \times 186 \times 146$	5.1
Overset Mesh 2	$187 \times 111 \times 21$	0.4
Overset Mesh 3	$187 \times 61 \times 20$	0.2
Overset Mesh 4	$187 \times 25 \times 20$	0.1
Vortex Tracking Grid	$70 \times 70 \times 1082$	5.3
Total		17.7

Table 3.3: Number of points used in various meshes for simulation for a $h/R = 0.5$.

Mesh	Dimensions	Mesh points (in millions)
Blade Mesh	$267 \times 93 \times 50$	1.2
Main Background Mesh	$127 \times 280 \times 217$	7.7
Overset Mesh 1	$187 \times 186 \times 146$	5.1
Overset Mesh 2	$187 \times 111 \times 21$	0.4
Overset Mesh 3	$187 \times 61 \times 20$	0.2
Vortex Tracking Grid	$70 \times 70 \times 846$	4.1
Total		18.7

take about 1 revolution per day when run in parallel on 32 Intel Xeon 3.20GHz processors.

3.4 Performance Comparison

The variation of the sectional thrust and power with span is plotted in fig 3.8 for the different rotor heights above the ground. As expected, the sectional thrust and power values increase across the span because of the increasing rotational velocity of the rotor blade. At the tip of the rotor blade, the drop in thrust and power values signifies the presence of the tip vortex. As the rotor height above the ground decreases, the sectional thrust increases at most of the span locations. However, an opposite trend is observed near the tip region. Looking at the power distribution, the results from the various rotor heights above the ground do not show much variation. Overall, the spanwise distribution looks consistent with what is expected from the experiment and theory due to the of decreasing rotor height above the ground.

Table 3.4 compares the computed integrated performance for the three different rotor heights with the measured experimental data. The values are normalized with the respective out of ground effect (OGE) values. In OGE, the thrust and power coefficient predicted by the computations are 0.0143 and 0.00249 respectively, whereas the experimental values are 0.0133 and 0.00227 respectively. The approximately 10% differences between the computational and experiments are possibly due to the difficulty in setting the exact collective angle in the experiments. The
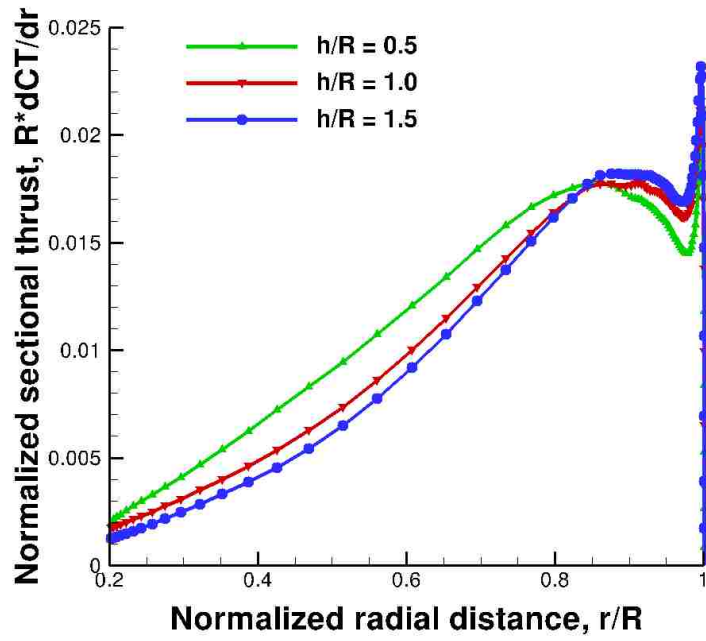
(a) Thrust coefficient
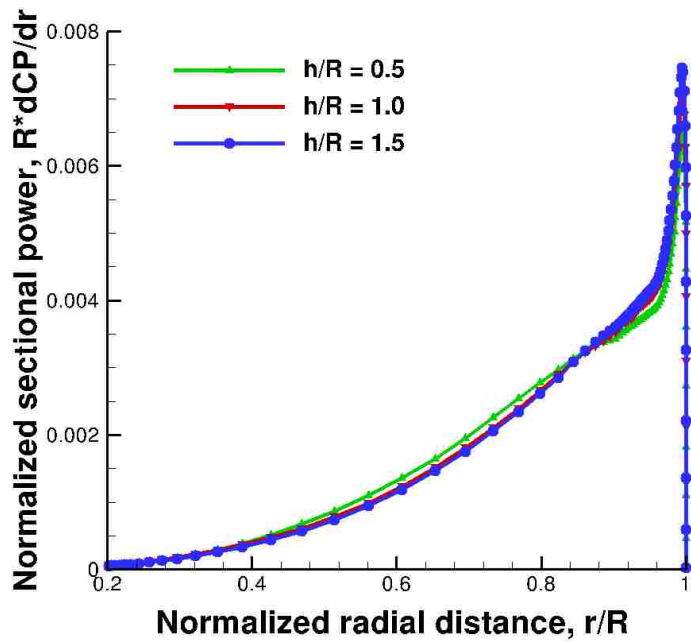
(b) Power coefficient

Figure 3.8: Spanwise variation of performance parameters.

computed OGE results compare better to a different set of experimental data obtained on the same rotor operating at similar flow conditions [29]. Details regarding the earlier computational work concerning the OGE values are given in [44]. From table 3.4, it is seen that the current simulations accurately predict the change in performance as the rotor height above the ground varies. As the rotor height above the ground decreases, the thrust increases as expected, while the power remains fairly constant (marginal increase with decreasing ground distance).

3.5   Flow field Comparison

Following the performance validation, the current section focuses on comparing the predicted flow field with the available experimental data. PIV measurements were performed to obtain velocity fields for the different ground distances. These velocities are used to obtain vorticity magnitude at corresponding wake-ages. Particular wake ages were then selected over a period of time from the experimental

Table 3.4: Thrust and power comparison with experiment [48] for different ro tor heights.

| h/R | $C_T/C_{T_{OGE}}$ | | $C_P/C_{P_{OGE}}$ | |
	Computed	Expt.	Computed	Expt.
0.5	1.23	1.26	1.07	1.05
1.0	1.15	1.17	1.06	1.05
1.5	1.06	1.08	1.06	1.04

data and then the data is averaged out and referred to as phase-averaged values in the experiments. Wake age is a measure of the time since the vortex was generated, in terms of the angular displacement (degrees of rotor rotation) of the corresponding blade (seen in fig. 3.9). A similar averaging process is carried out using the CFD solution using the data from 30 different instances of time to obtain the phase-averaged vorticity values.
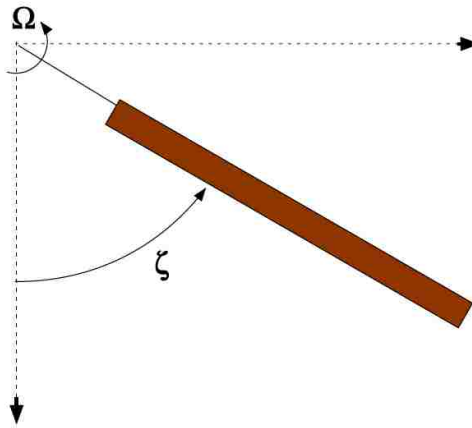
Figure 3.9: Schematic showing wake age, ζ.

Figure 3.10 shows the CFD predicted and experimentally measured comparison of phase-averaged azimuthal vorticity contours at three different wake ages ($\zeta = 0°$, 60°, and 120°) for the rotor height of $1R$ above the ground. The plot also shows the velocity vectors at one in every four grid points in both the normal and radial directions in the simulation. From the plot, it can be seen that the predicted wake trajectory is very similar to that from the experiment data at all wake ages. In addition, the strength of the predicted azimuthal vorticity is in good agreement with the experimental results. The tip vortices are well captured for five blade
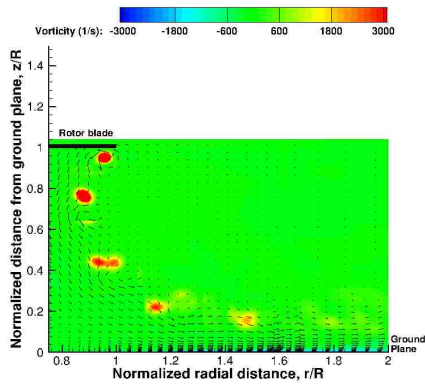
(a) Computational result, $\zeta = 0°$ (b) Experimental result, $\zeta = 0°$
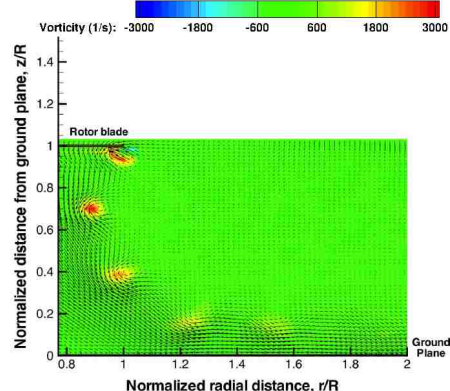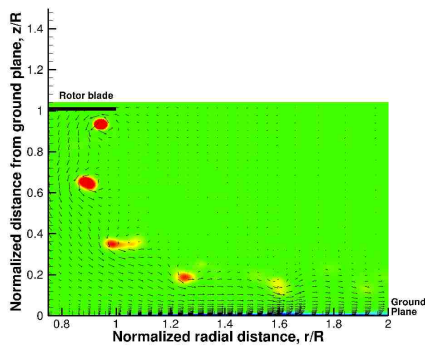
(c) Computational result, $\zeta = 60°$ (d) Experimental result, $\zeta = 60°$
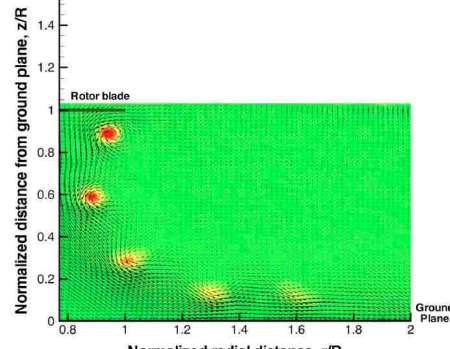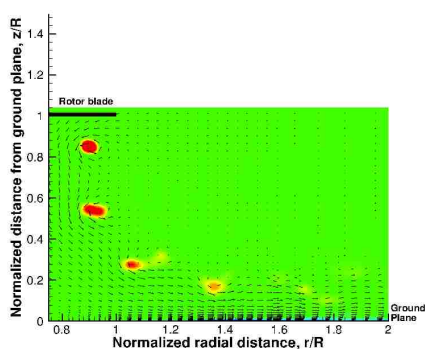
(e) Computational result, $\zeta = 120°$ (f) Experimental result, $\zeta = 120°$
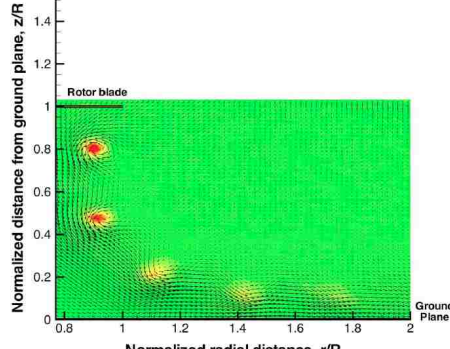
Figure 3.10: Comparison of CFD predicted phase-averaged vorticity contours (along with velocity vectors) with experimental data [48] at different wake ages for $h/R = 1.0$.
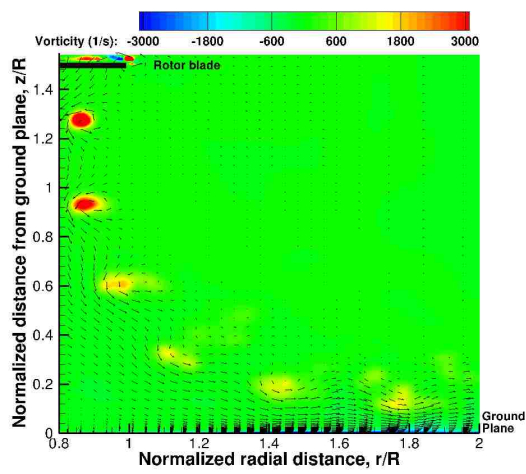
(a) Computational result, $h/R = 1.5$
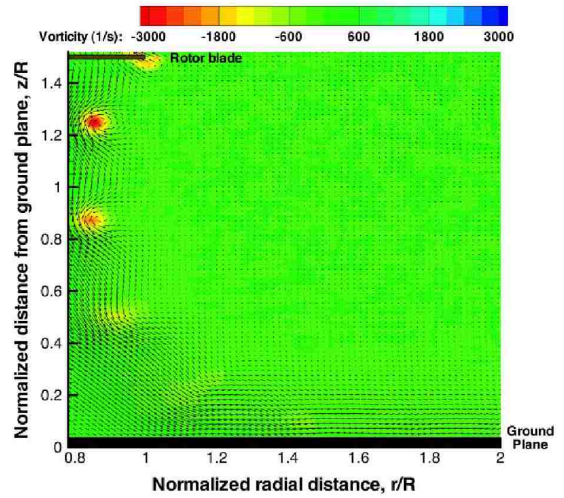
(b) Experimental result, $h/R = 1.5$
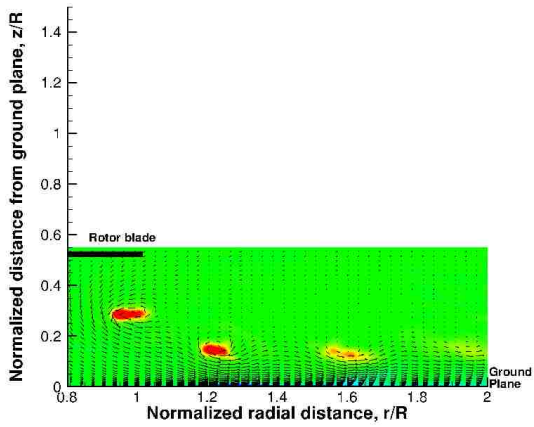
(c) Computational result, $h/R = 0.5$
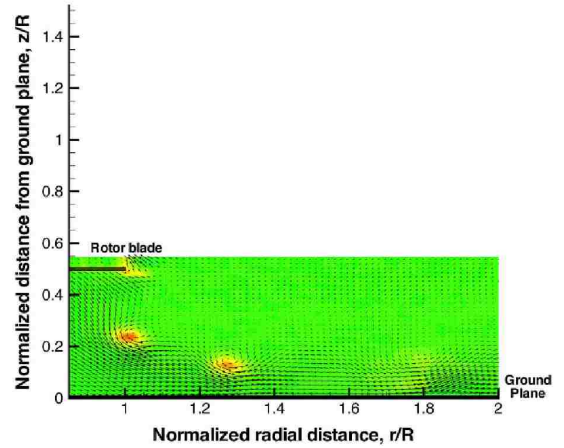
(d) Experimental result, $h/R = 0.5$

Figure 3.11: Comparison of CFD predicted phase-averaged vorticity contours (along with velocity vectors) with experimental data [48] for various rotor heights at $\zeta = 0°$.
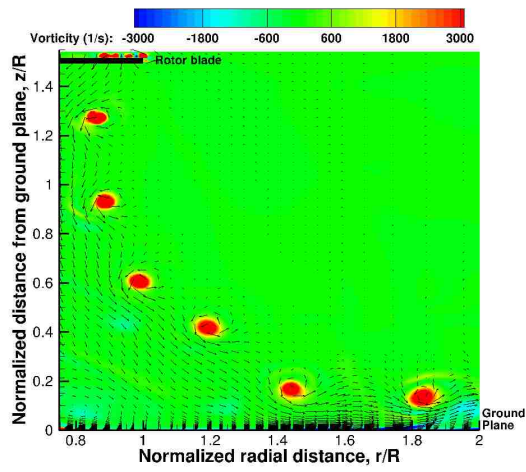
(a) Computational result, $h/R = 1.5$
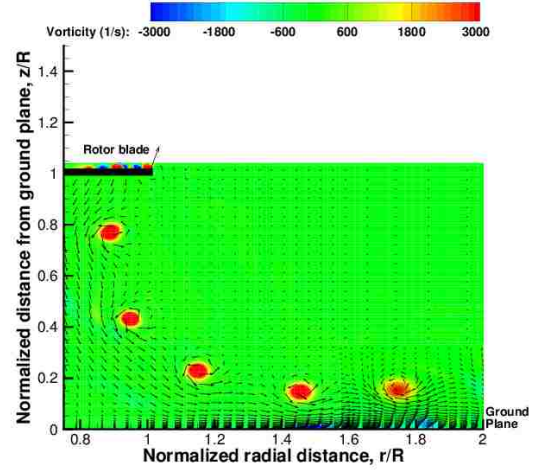
(b) Computational result, $h/R = 1.0$
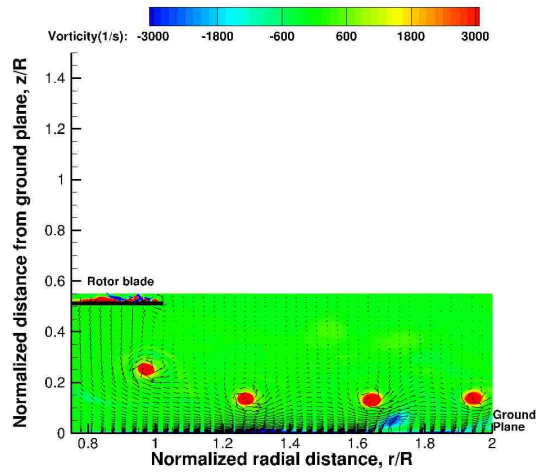
(c) Computational result, $h/R = 0.5$

Figure 3.12: CFD predicted instantantaneous vorticity contours (along with velocity vectors) for various rotor heights at $\zeta = 0°$.

passages. The tip vortices are observed to initially contract under the effect of the rotor wake. However, they begin to move radially outward as they approach the ground. The ground effect causes a stretching of the vortex filaments and a reintensification of the vortex cores. Eventually, the vortices start to become less stable, start to wander, and hence become aperiodic. Consequently, the vortices at older wake ages get smeared out during the phase-averaging process, observed in both the computation as well as the experiment. The smearing out at older wake ages is more noticeable in the experimental results than in the computational solutions. This can be attributed to the fact that the phase-averaged results CFD use a fewer number of instances for averaging compared to the experiment.

Similar to the vorticity contours shown for the rotor height of $1R$ above the ground, figure 3.11 shows the comparison between CFD predictions and experimental data of the phase-averaged azimuthal vorticity contours for the other two rotor heights of $h/R = 0.5$ and $h/R = 1.5$ at $\zeta = 0°$. One can notice that the tip vortex positions along with the vorticity magnitude resulting from the computations compare well with those from the experiments for both rotor heights.

Although the phase-averaged results show smeared out vorticity contours at later wake ages, an instantaneous snapshot of the vorticity in fig. 3.12 of the CFD predicted instantaneous vorticity contours (along with velocity vectors) at $0°$ wake age shows well defied tip vortices at the later blade passages. Note that the instantaneous experimental results are not available for comparison. Figure 3.12 reveals that the tip vortices at older wake ages are still significantly strong due to the intensification caused by the stretching of the vortex filament under ground effect. The

tip vortices are well captured for four, five, and six blade passages, respectively, for the $0.5R$, $1.0R$, and $1.5R$ rotor heights, thereby clearly demonstrating the capability of the current mesh system to accurately resolve the tip vortices for sufficiently long periods of time. The differences between the instantaneous and phase-averaged results from the simulations for the older tip vortices signifies the growing degree of unsteadiness and wandering as the vortices interact with the ground plane.

3.6 Time-Averaged Velocity Profile Comparison

A more quantitative validation of the CFD results is done by comparing the time-averaged radial-velocity profiles at several radial locations with the experimental data for the three rotor heights, shown in Figs. 3.13–3.15. The velocities are normalized by the ideal hover induced velocity for the corresponding thrust value. From the plot, the computations can be observed to predict the overall physics of the flow field correctly. For all cases, the rotor induced flow is forced to expand radially outward, creating a wall jet. The height of the wall jet is seen to decrease (similar to the experimental data) as one moves radially outward. As a consequence, there is an increase in the peak radial velocity as the radial distance increases, until it eventually starts to decrease at the outermost measured radial station due to radial spreading. Furthermore, the jet boundary layer begins to thicken at the outermost radial station. CFD predicts a marginally higher maximum radial velocity and at a slightly larger wall distance than that measured in the experiment.
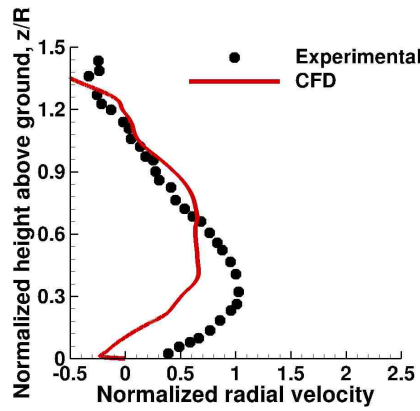
(a) $r/R = 0.8$
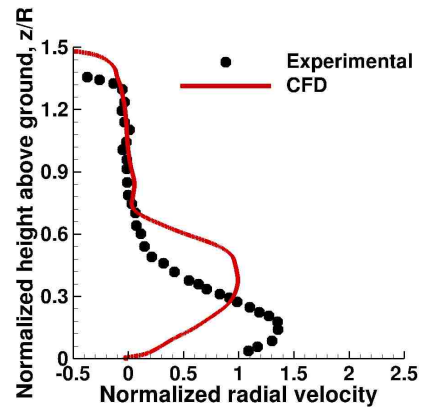
(b) $r/R = 1.0$
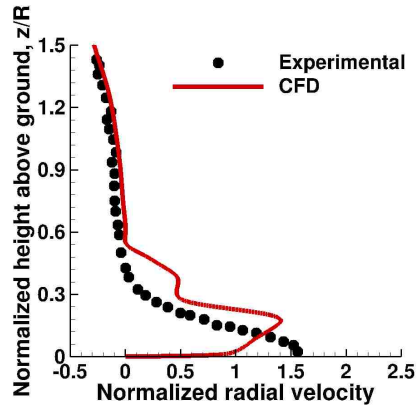
(c) $r/R = 1.25$
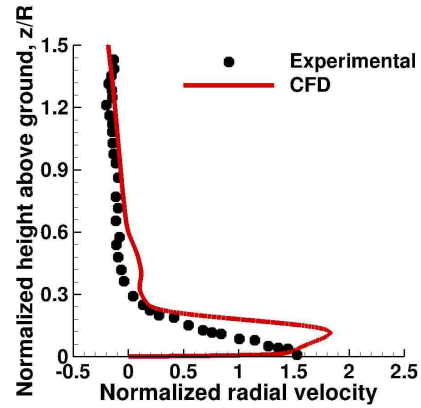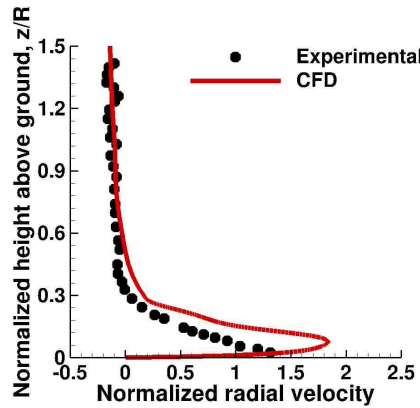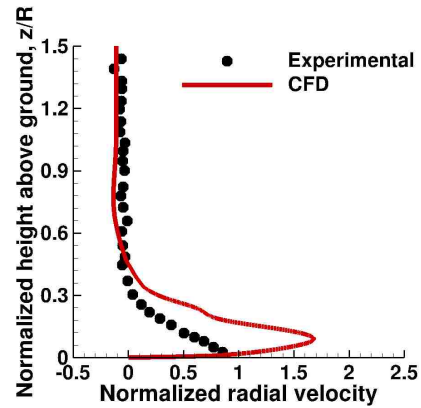
(d) $r/R = 1.5$

(e) $r/R = 1.75$

(f) $r/R = 2.0$

Figure 3.13: Comparison of CFD predicted time-averaged velocity profile with experimental data [48] at several radial locations for a rotor height of $h/R = 1.5$.
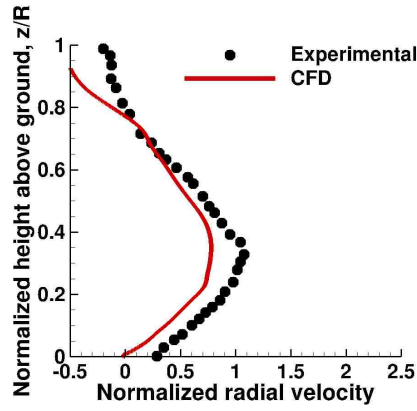
(a) $r/R = 0.8$
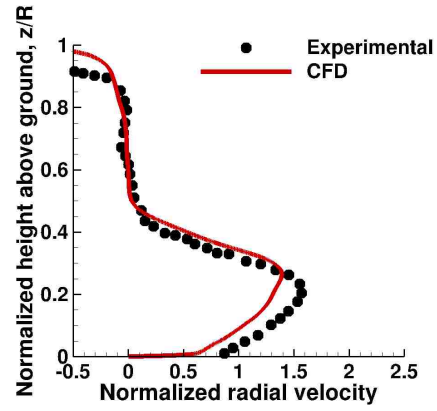
(b) $r/R = 1.0$
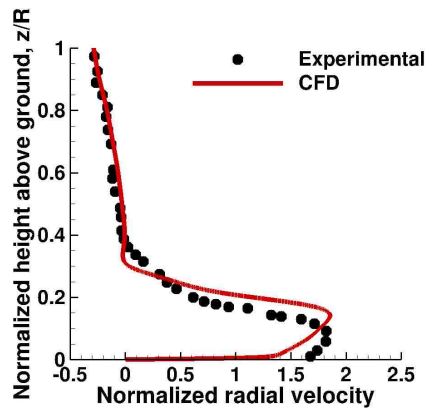
(c) $r/R = 1.25$
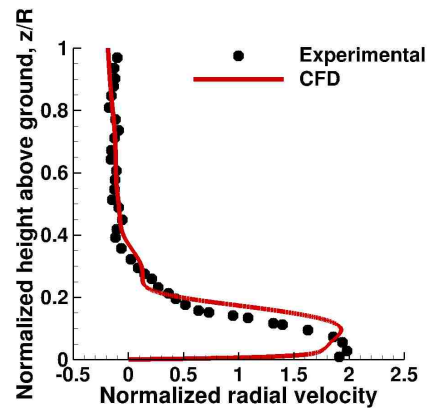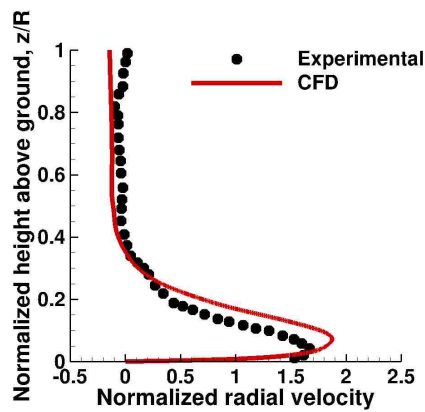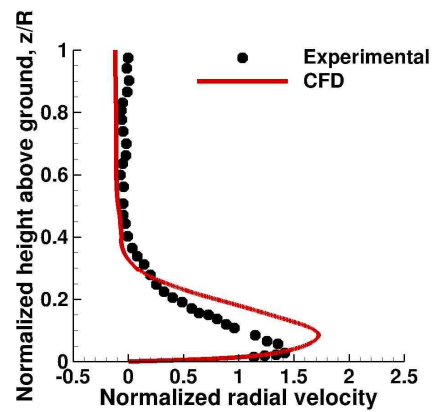
(d) $r/R = 1.5$

(e) $r/R = 1.75$
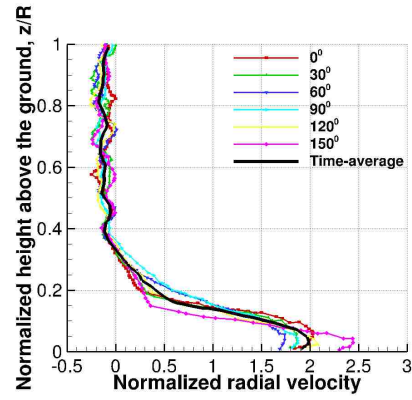
(f) $r/R = 2.0$

Figure 3.14: Comparison of CFD predicted time-averaged velocity profile with experimental data [48] at several radial locations for a rotor height of $h/R = 1.0$.
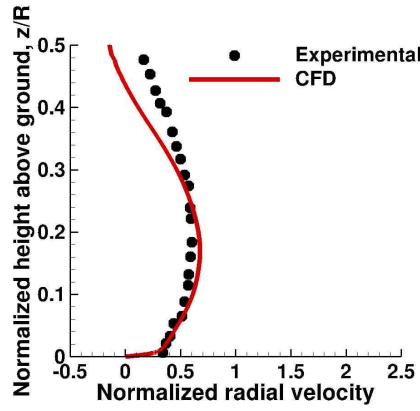
(a) $r/R = 0.8$
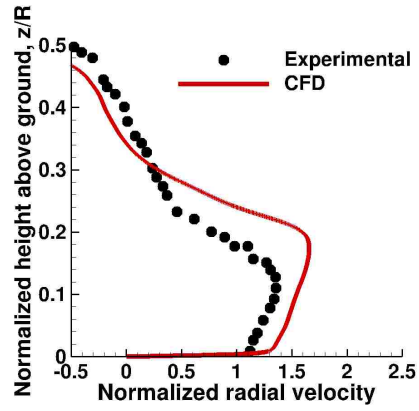
(b) $r/R = 1.0$
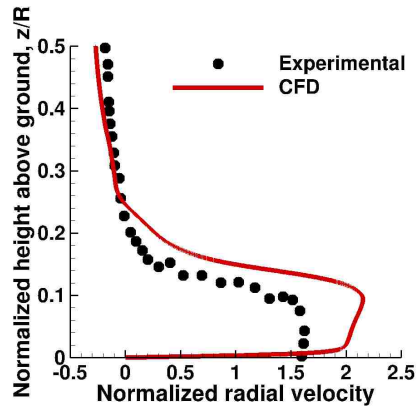
(c) $r/R = 1.25$
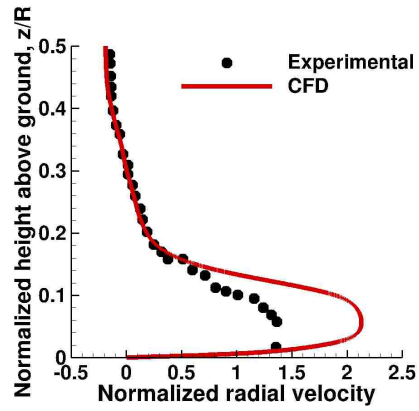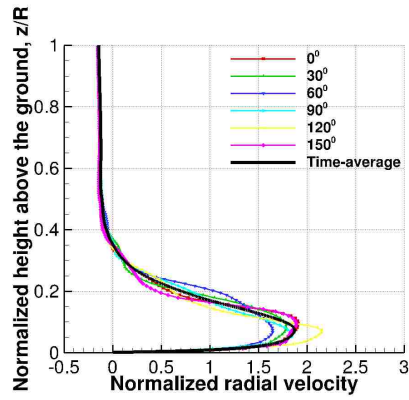
(d) $r/R = 1.5$
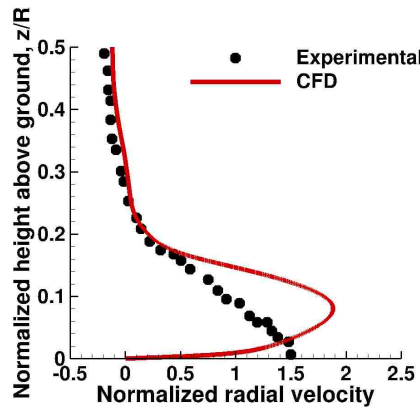
(e) $r/R = 1.75$
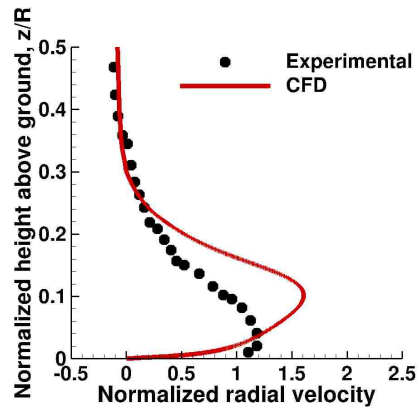
(f) $r/R = 2.0$

Figure 3.15: Comparison of CFD predicted time-averaged velocity profile with experimental data [48] at several radial locations for a rotor height of $h/R = 0.5$.

3.7 Phase-Averaged Velocity Profile Comparison

A more detailed validation of the calculation is performed by comparing the phase-averaged radial-velocity profiles (normalized by the ideal hover induced velocity for the corresponding thrust value). Figures 3.16–3.17 show the computational results in comparison with the experimental data for the rotor height of $1R$ above the ground at six radial locations ($r/R = 0.8$, $r/R = 1.0$, $r/R = 1.25$, $r/R = 1.5$, $r/R = 1.75$ and $r/R = 2.0$). The phase-averaged radial-velocity profiles are plotted along with the time-averaged radial-velocity profiles, which were discussed earlier. Note that the time-averaged velocity is approximately equal to the average of all the phase-averaged velocities. The fluctuations seen in the phase-averaged radial velocity profiles are due to the local velocity induced by the presence of the tip vortex as it passes by the radial station. These fluctuations are indicative of the unsteadiness of the flow at the ground plane. An accurate prediction of these fluctuations is important to capture the resulting dust entrainment correctly. These fluctuations do not show up in the time-averaged values due to the averaging out of the transients. The predicted phase-averaged velocities agree extremely well with the experimental data. The fluctuations become smaller at the outboard stations as compared to directly underneath the rotor tip. Furthermore, the computed phase-averaged velocity profiles for $0.5R$ and $1.5R$ rotor heights are seen in figs. 3.18 and 3.19. The plots show similar patterns as that for the $1R$ rotor height. Note that only the computational results are shown for these two rotor heights as the experimental results are not available.
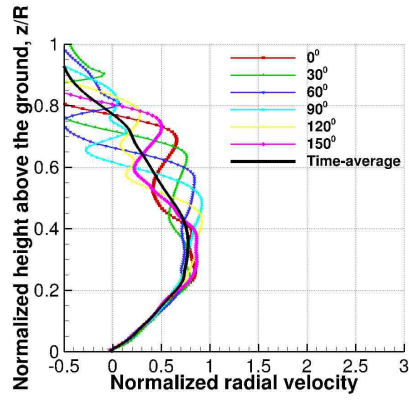
(a) Computational, $r/R = 0.8$ (b) Experimental, $r/R = 0.8$
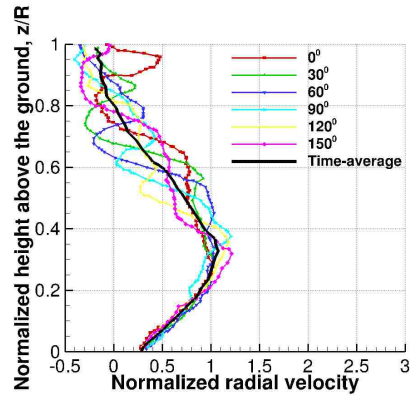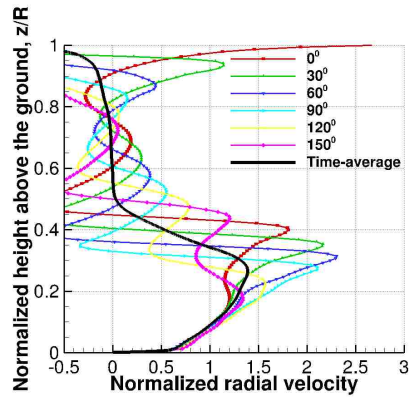
(c) Computational, $r/R = 1.0$ (d) Experimental, $r/R = 1.0$
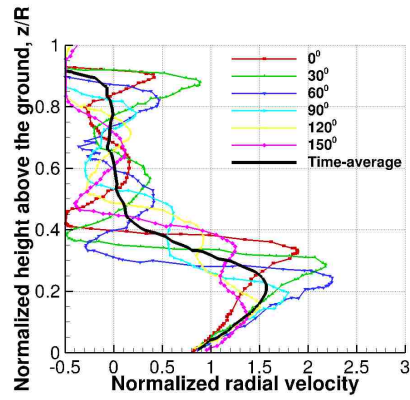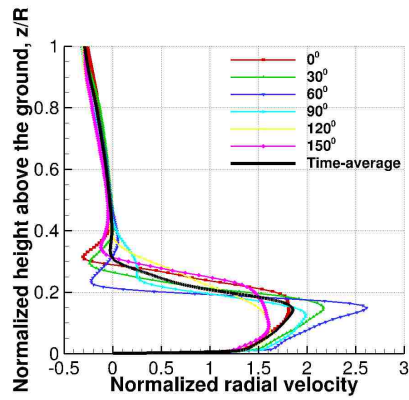
(e) Computational, $r/R = 1.25$ (f) Experimental, $r/R = 1.25$
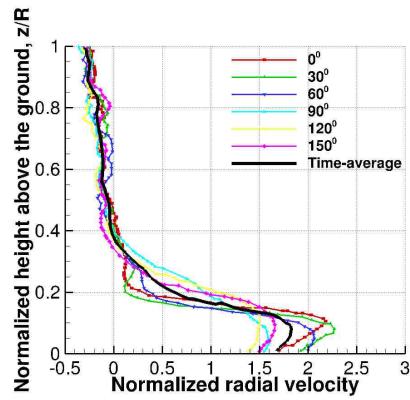
Figure 3.16: Comparison of CFD predicted phase-averaged velocity profiles with exper imental data [48] at several radial locations for a rotor height of $h/R = 1.0$.
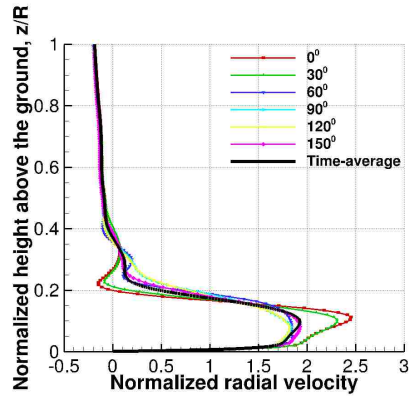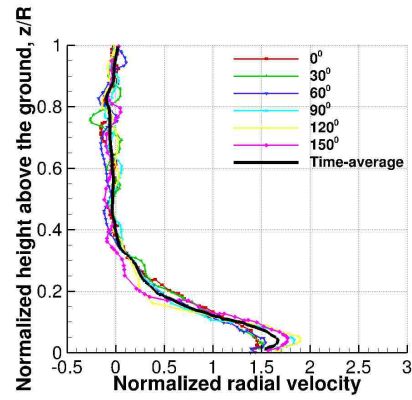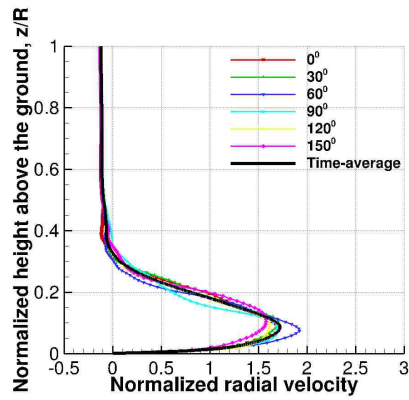
(a) Computational, $r/R = 1.5$
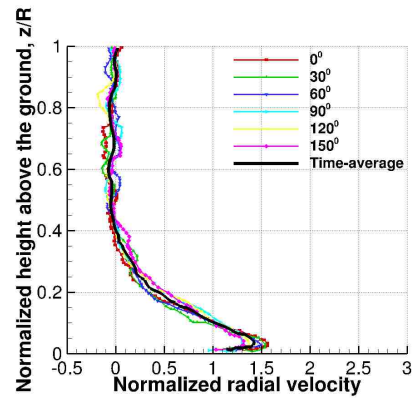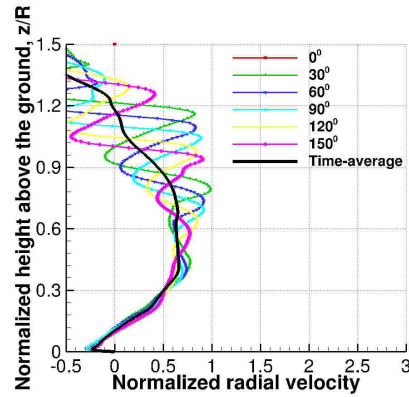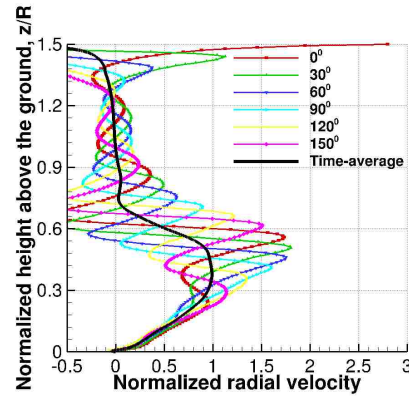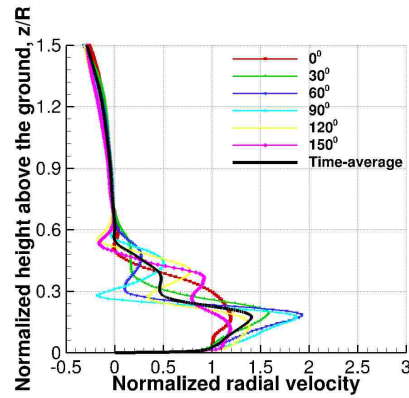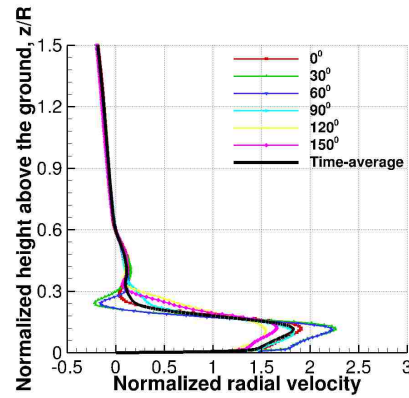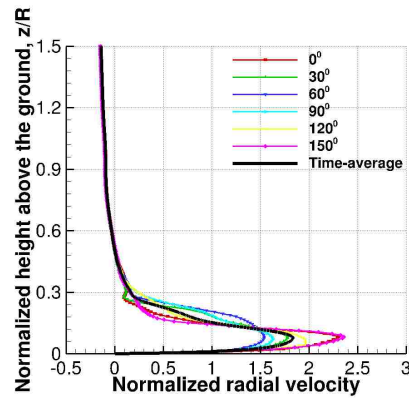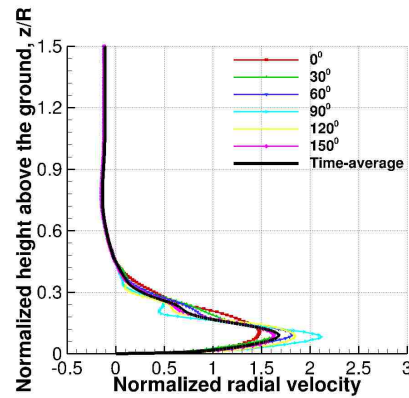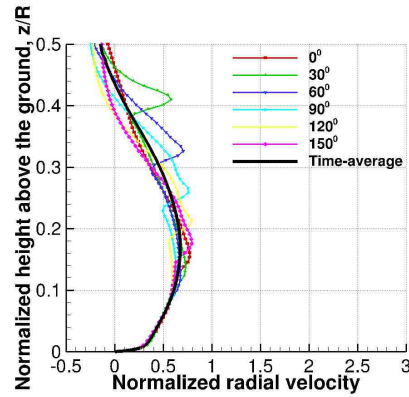
(b) Experimental, $r/R = 1.5$

(c) Computational, $r/R = 1.75$

(d) Experimental, $r/R = 1.75$

(e) Computational, $r/R = 2.0$

(f) Experimental, $r/R = 2.0$

Figure 3.17: Comparison of CFD predicted phase-averaged velocity profiles with exper imental data [48] at several radial locations for a rotor height of $h/R = 1.0$.

(a) $r/R = 0.8$

(b) $r/R = 1.0$
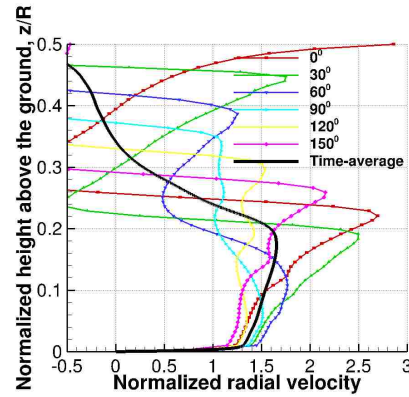
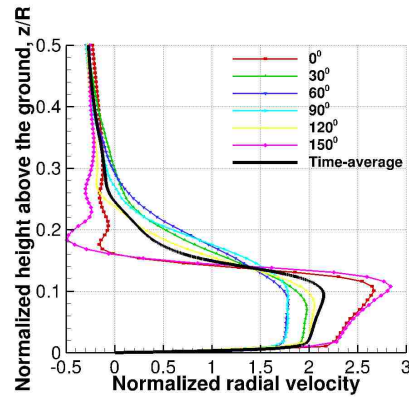(c) $r/R = 1.25$

(d) $r/R = 1.5$

(e) $r/R = 1.75$

(f) $r/R = 2.0$

Figure 3.18: CFD predicted phase-averaged velocity profiles at several radial locations for a rotor height of $h/R = 1.5$. (Note: Experimental data not available for this rotor height).
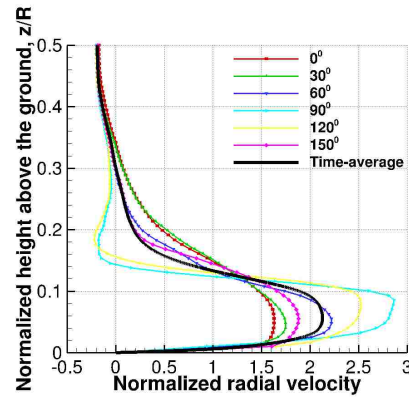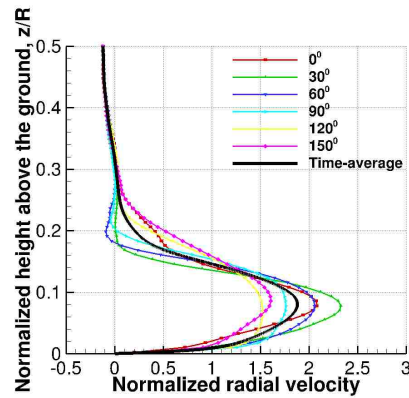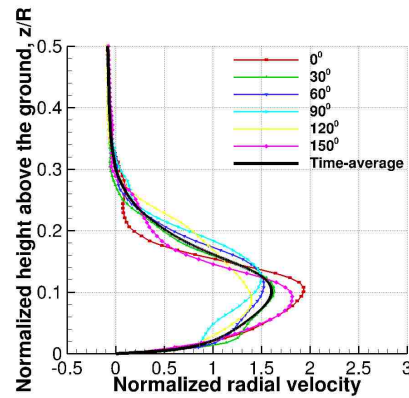
(a) $r/R = 0.8$

(b) $r/R = 1.0$

(c) $r/R = 1.25$

(d) $r/R = 1.5$

(e) $r/R = 1.75$

(f) $r/R = 2.0$

Figure 3.19: CFD predicted phase-averaged velocity profiles at several radial locations for a rotor height of $h/R = 0.5$. (Note: Experimental data not available for this rotor height).

3.8   Predicted Global Vortical Structure

The overall vortical structure of the flow field can be best visualized by plotting an isosurface of q-criterion [86] shaded by vorticity contours. Figure 3.20 compares the instantaneous computational predictions of the three-dimensional structure of the tip-vortex trajectory for the three different rotor heights above the ground. For clarity, the flow field from the entire domain is shown even though the simulation is done only using half the domain. The tip vortices can be seen to be well preserved all the way to the ground in all cases. From the plots, it can be noticed that at early wake ages, the tip vortex is tightly braided. At later wake ages, the vortices start to develop instabilities, primarily due to the interaction of strong vortices (intensified from rapid wake expansion near the ground) with the ground as well as with the vortices from other blade passages.
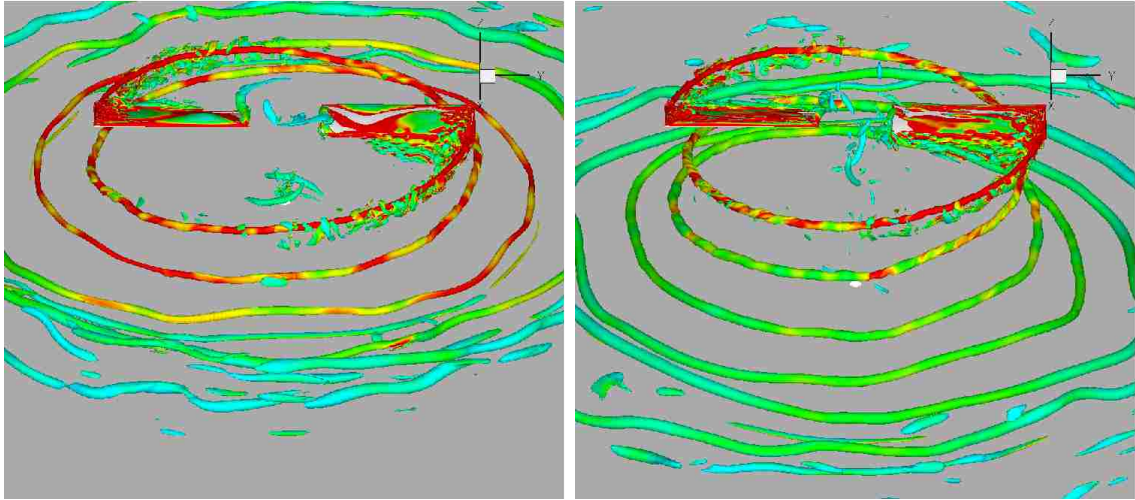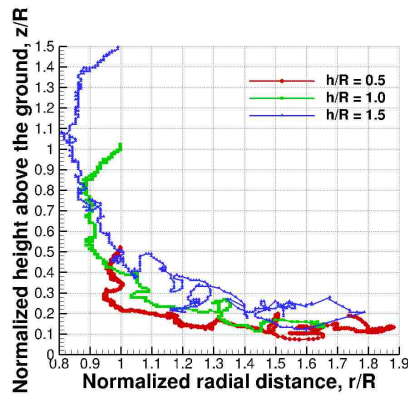
(a) $h/R = 0.5$ (b) $h/R = 1.0$
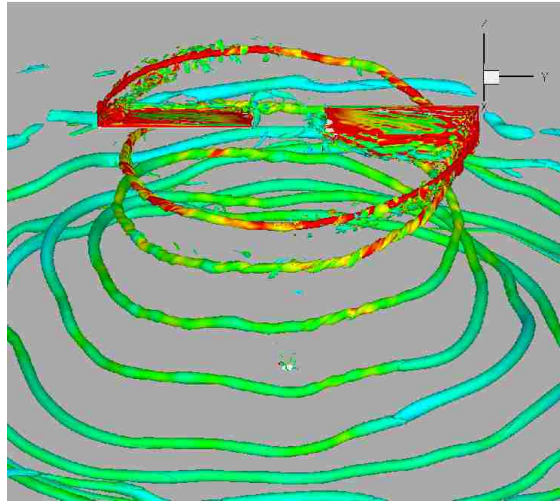
(c) $h/R = 1.5$

Figure 3.20: Iso-contours of q-criterion, $q = 0.25$ for different rotor heights above ground.

The aperiodicity of the wake is an inherent characteristic of rotor flows, and can be quantified by plotting the wake trajectories in both the radial and vertical directions. Figure 3.21(a) and(b) show the radial and vertical positions of the tip vortices as a function of wake age for all rotor heights at an instant in time. Figure 3.21(c) shows the radial variation of the wake trajectory for the three different heights above the ground. The instantaneous tip-vortex trajectory clearly shows high levels of instability for all three rotor heights. To understand the extent of tip-vortex wandering, Fig. 3.22 shows the scatter of the wake trajectory predicted over one revolution along with the phase-averaged trajectory for all three rotor heights. Clearly, a significant amount of wake wandering is observed in all cases. The vortex shows increased wandering in both the radial and vertical directions at later wake ages, as it approaches the ground. The scatter occurs more on the outer portion of the curves (above and to the right) than on the inner portion. This is possibly due to the limit imposed by the ground surface and the center of rotation on the amount of excursion. The tip vortex wanders more for smaller rotor heights at a given wake age because of its closer proximity to the ground, but the scatter is comparable at a particular height from the ground for the various rotor heights. Looking at the phase-averaged trajectories, one can observe that they are much smoother as compared to the instantaneous trajectories for all cases. Remember that the VTGs are generated based on the phase-averaged trajectories along with further smoothing based on a Laplacian-based operator. To quantify the extent of the tip-vortex wandering, the root mean square (rms) deviation of the wake trajectory from the phase-averaged radial and vertical positions is shown as a
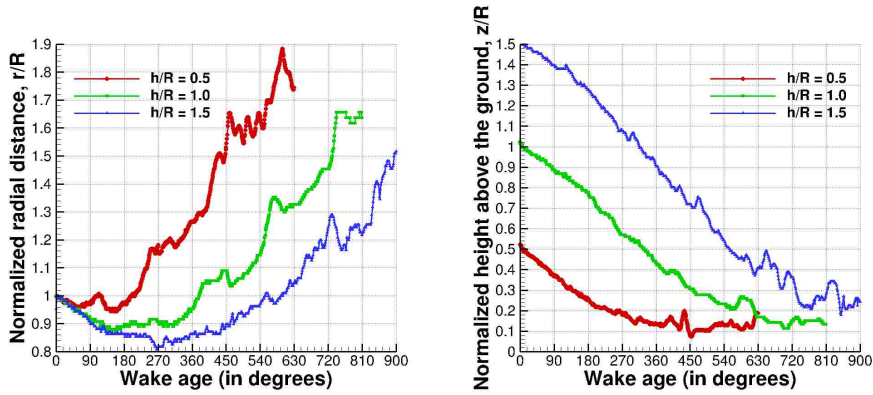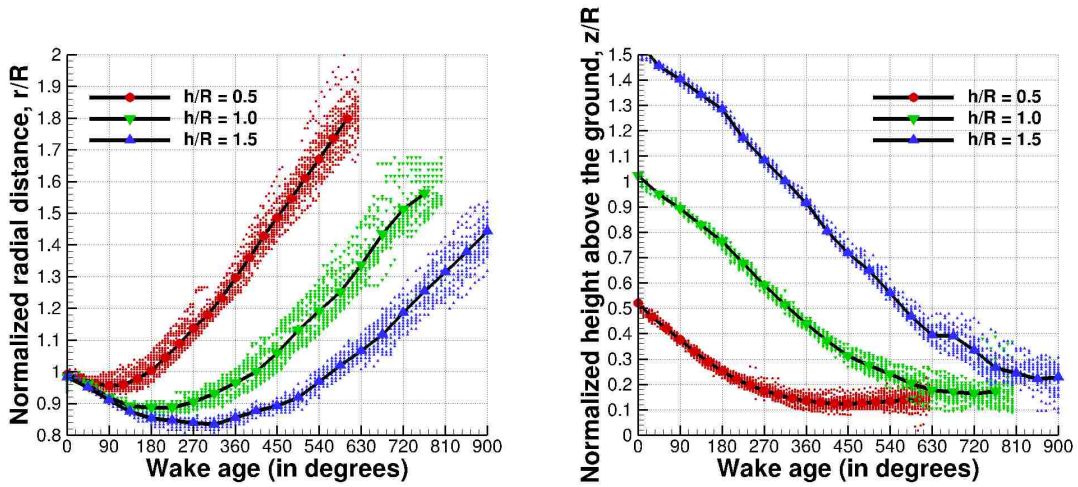
(a) Variation of tip vortex radial dis- (b) Variation of tip vortex height with

tance with wake age   wake age

(c) Variation of tip vortex height with

radial location

Figure 3.21: Instantaneous wake trajectory predictions using CFD.

function of wake age in fig. 3.23. As seen earlier, the extent of wake wandering in

both the radial and vertical directions increases with wake age for all rotor heights.

Interestingly, only the radial wake scatter compared at a particular wake age is

smaller for larger rotor heights, whereas the vertical wake scatter at a particular

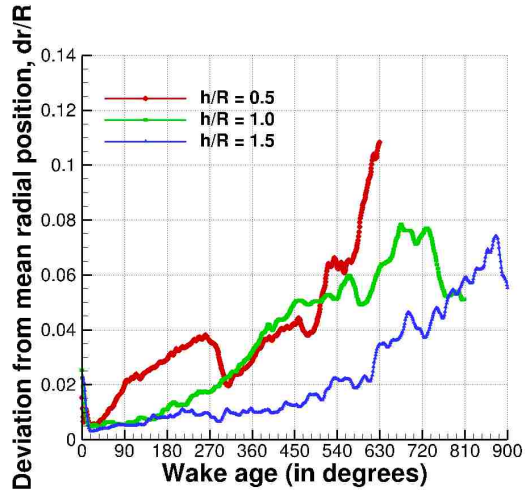wake age is comparable for all rotor heights.

(a) Variation of phase-averaged tip vortex radial distance with wake age

(b) Variation of phase-averaged tip vortex height with wake age
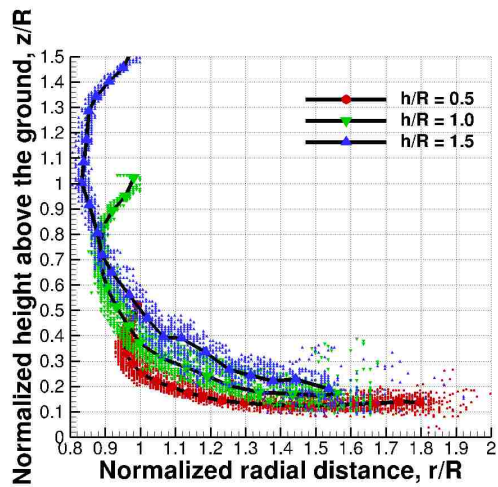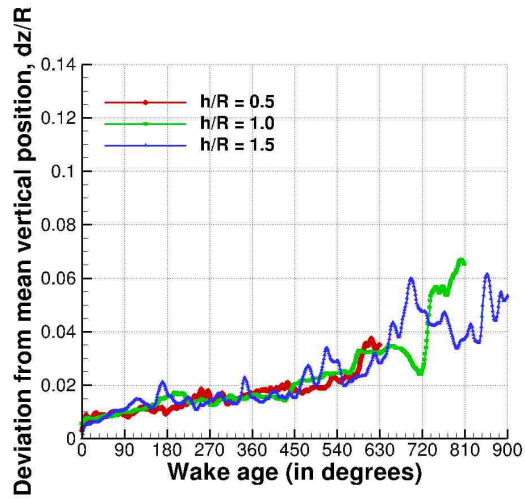

(c) Variation of phase-averaged tip vortex height with radial location

Figure 3.22: Wake scatter and phase-averaged wake trajectory (in black line) predictions using CFD.

110

(a) Deviation from mean radial position for all

cases

(b) Deviation from mean vertical position for all

cases

Figure 3.23: Root mean square deviation of wake trajectory from mean position.
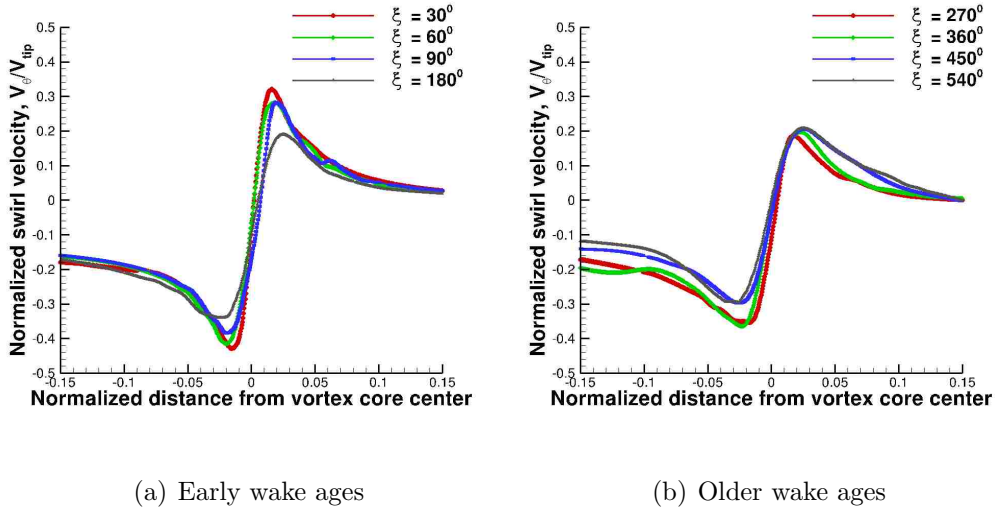
(a) Early wake ages   (b) Older wake ages

Figure 3.24: CFD predicted normalized swirl velocity at different wake ages.

3.9 Tip Vortex Characteristics

The tip vortex can be characterised by looking at swirl velocity profiles across a line passing through the center of the vortex. Figure 3.24 shows the instantaneous normalized swirl velocity profile as a function of normalized distance from the vortex core center at different wake ages for the rotor height of $1R$. The swirl velocity is normalized by the tip speed and the distance is normalized by the rotor radius. At early wake ages, as seen in Fig. 3.24(a), the peak swirl velocity decreases and the core radius increases rapidly. However, at older wake ages (shown in Fig. 3.24(b)), the rate of peak swirl decay and the core growth decreases due to the re-intensification process.
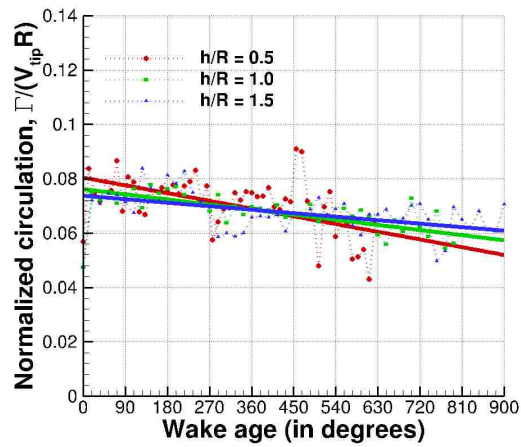
Figures 3.25 (a) and (b), which respectively show the variation of peak swirl velocity and vortex core radius as a function of wake age for all three rotor heights at one instant in time, confirms the above observation. The actual predicted values

112
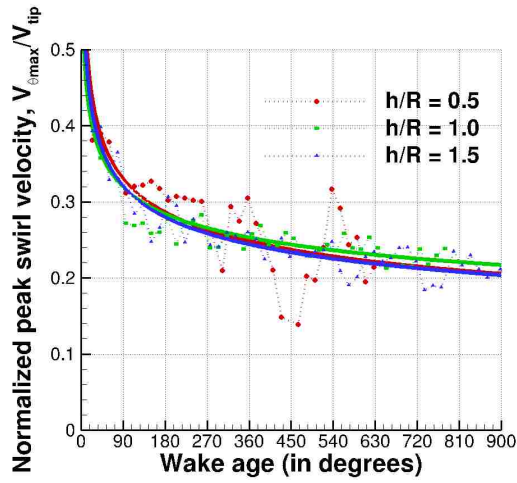
(a) Peak swirl velocity
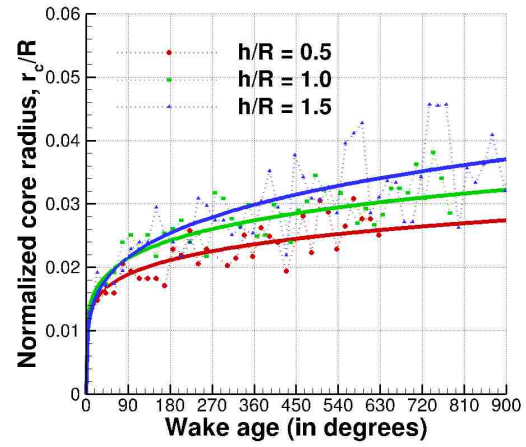
(b) Vortex core radius growth

(c) Circulation

Figure 3.25: Variation of the tip vortex characteristics as a function of wake age for the micro-scale rotor: (a) Peak swirl velocity (b) Vortex core radius (c) Circulation.

are shown by dotted points and a curve fit through these points is shown by a solid line. Note that the peak swirl velocity is normalized by the tip speed and the core radius is normalized by the rotor radius. The peak swirl decay is comparable at all rotor heights, however, for the smaller rotor heights, the vortices exhibit faster core growth. Correspondingly, the circulation (normalized by the tip speed and the rotor radius) decays at a faster rate at smaller rotor heights (Figure 3.25(c)). As compared to larger rotor heights, smaller rotor heights have larger circulation levels at early wake ages due to the higher thrust generated by the rotor, but have smaller values at later wake ages. The reason for the slightly faster drop in circulation and increase in core growth for smaller rotor heights is because of increased turbulence levels in the wake (shown later).

3.10   Velocities at the Ground

Due to the relatively thin boundary layer region at the ground (less than 5% of rotor radius), the experiments did not explore the nature of the boundary layer in much detail. When the boundary layer is thin, PIV requires very fine spatial resolution near the ground and must minimize laser reflections, both of which pose extreme challenges. Therefore, there is no experimental validation for the velocities predicted by the current simulation methodology near the ground. However, the current CFD solution can still be used to explore some of the physics near the ground.

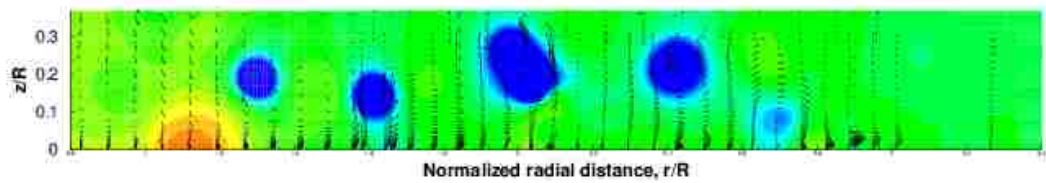Figures 3.26, 3.27, and 3.28 show the velocity vectors along with the pressure

114

(a) $\zeta = 0°$
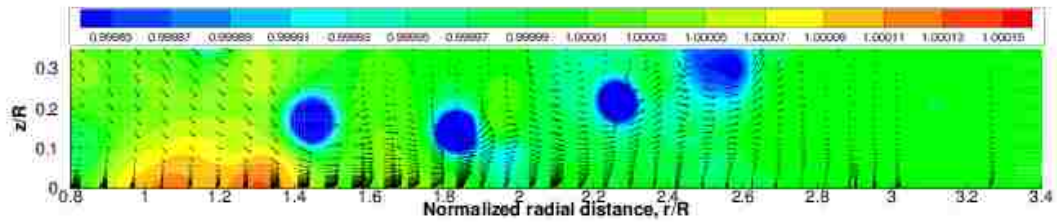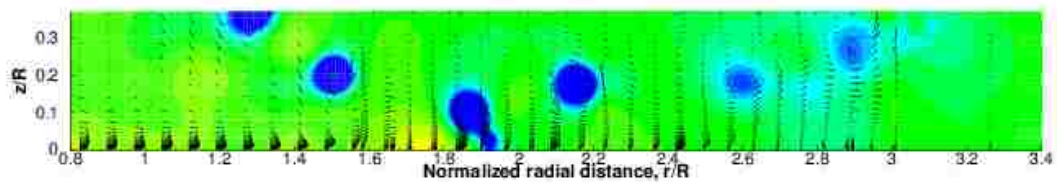
(b) $\zeta = 60°$

(c) $\zeta = 120°$

Figure 3.26: Instantaneous pressure contours (normalized by freestream value) along with velocity vectors for a rotor height of $h/R = 1.5$.

(a) $\zeta = 0°$

(b) $\zeta = 60°$

(c) $\zeta = 120°$

Figure 3.27: Instantaneous pressure contours (normalized by freestream value) along with velocity vectors for a rotor height of $h/R = 1.0$.

(a) $\zeta = 0°$

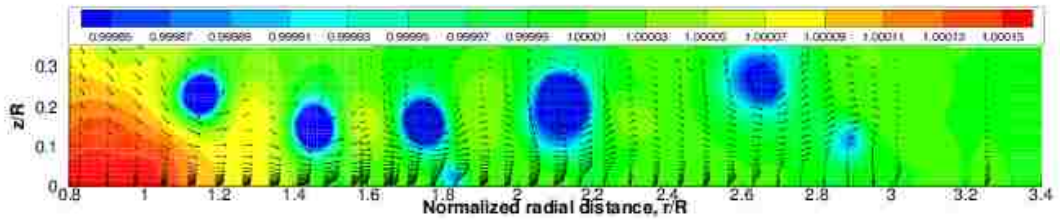(b) $\zeta = 60°$
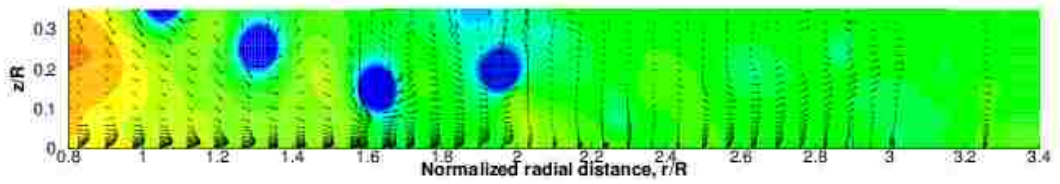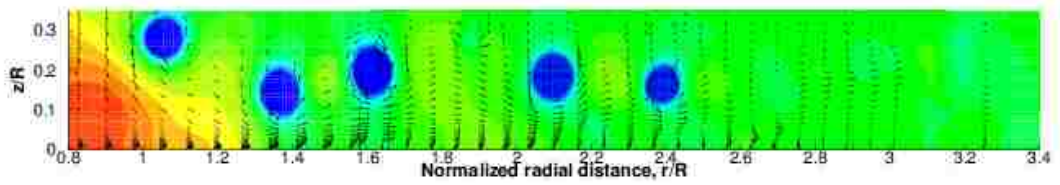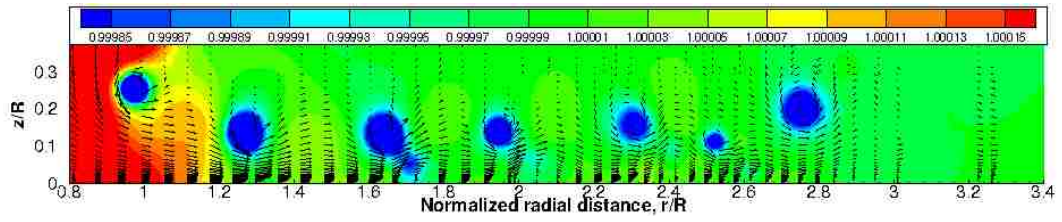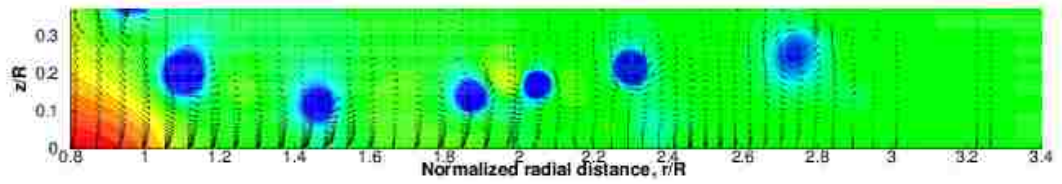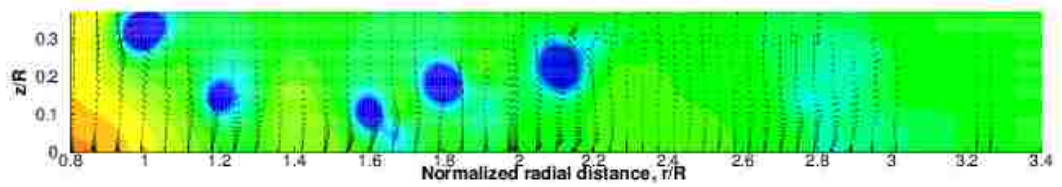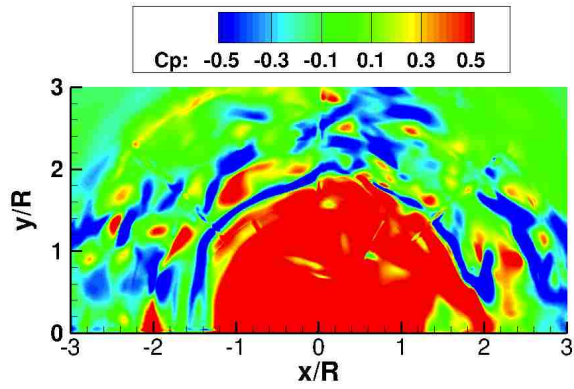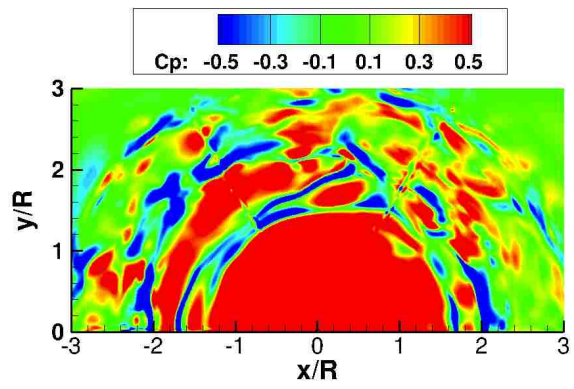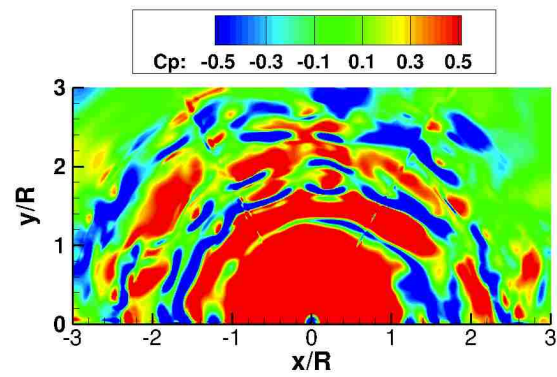

(c) $\zeta = 120°$

Figure 3.28: Instantaneous pressure contours (normalized by freestream value) along with velocity vectors for a rotor height of $h/R = 0.5$.

(a) $h/R = 1.5$

(b) $h/R = 1.0$

(c) $h/R = 0.5$

Figure 3.29: Pressure coefficient at the ground plane for one instant in time.

contours (normalized by freestream value) for the rotor heights of $1.5R$, $1.0R$ and $0.5R$ above the ground, respectively. For the purpose of clarity, the vectors are plotted only one in every four points in the normal direction and one in every eight points in the radial direction from the mesh used for the simulation. In all the cases, the tip vortex can be easily identified by the low pressure region. There is a region of high pressure on the ground corresponding to the stagnation location. The jet flow at the ground is directed outwards at locations outboard of the stagnation point and and inwards inboard of it. It can be noticed that the position of the tip vortex does not change smoothly from one wake age to the other and the flow is highly aperiodic. This form of viscous vortex/boundary layer interaction was observed even in the experiments of Johnson et al. [15] and has been described by Harvey and Perry [87] for conditions in which a trailing wing-tip vortex came under the influence of the ground. At certain wake ages for all the three rotor heights, the induced velocity from the tip vortices close to the ground causes the jet flow on the ground to separate and form a separation bubble. The region of separation bubble is also marked by low pressure. This separation bubble, formed at one wake age, peels off from the ground plane at a later wake age forming an opposite sign vortex. The opposite sign vortex interacts with the tip vortex, thereby further developing instabilities. Another interesting feature to notice for the rotor height of $0.5R$ above ground is the large high pressure region produced by the blade directly below the rotor at $0°$ wake age. Such large pressure can accelerate the jet flow near the ground.

The unsteady pressure variation at the ground plane can be a contributing factor for the sediment mobilization as discussed earlier. Figure 3.29 shows pressure

coefficient variation at the ground plane for the three rotor heights at a single instant in time. The striations in the pressure values represent the presence of the tip vortex. It can be observed that the least amount of pressure variation is for the rotor height of $1.5R$ above the ground. Both the $1.0R$ and $0.5R$ show a more considerable amount of pressure variation.
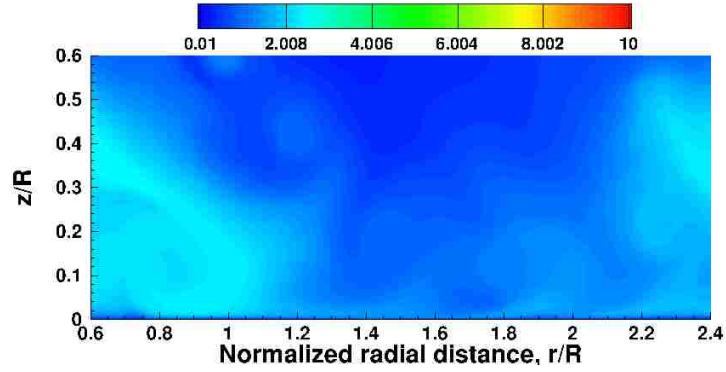
3.11   Eddy Viscosity and Friction Velocity Contours

Eddy viscosity contours can be used to better view the turbulence levels at the ground. Figures 3.30, 3.31 and 3.32 show the eddy viscosity contours (normalized by laminar viscosity) in a vertical plane at 0^0 wake age as well as the ground friction velocity contours (normalized by tip speed) for the rotor heights of $1.5R$, $1.0R$ and $0.5R$ above ground, respectively.

Comparing the eddy viscosity contours from the simulations for the various rotor heights above ground, it is seen that the magnitude of eddy viscosity increases as the rotor height above the ground decreases. Also for all the rotor heights above the ground, the higher eddy viscosity region from the vortex (eddy viscosity gets fed into the vortex from the inboard sheet) interacts with the higher eddy viscosity region formed near the ground, resulting in an intermixing of the turbulence levels.

Particle upliftment at the ground is directly proportional to the friction velocity at the ground [9]. Once a threshold friction velocity is reached, it can cause the minimum shear stress required to overcome the gravitational and cohesive forces and lead to particle mobilization. Figures 3.30(b), 3.31(b), and 3.32(b), respectively,

(a) Contours of eddy viscosity normalized by laminar viscosity for a vertical plane at 0° wake age

(b) Contours of friction velocity normalized by tip speed at the ground

Figure 3.30: Instantaneous contours of eddy viscosity and ground friction velocity f or a rotor height of $h/R = 1.5$.

121

(a) Contours of eddy viscosity normalized by laminar viscosity for a vertical plane at 0° wake age

(b) Contours of friction velocity normalized by tip speed at the ground

Figure 3.31: Instantaneous contours of eddy viscosity and ground friction velocity for a rotor height of $h/R = 1.0$.

(a) Contours of eddy viscosity normalized by laminar viscosity for a vertical plane at 0° wake age

(b) Contours of friction velocity normalized by tip speed at the ground

Figure 3.32: Instantaneous contours of eddy viscosity and ground friction velocity for a rotor height of $h/R = 0.5$.

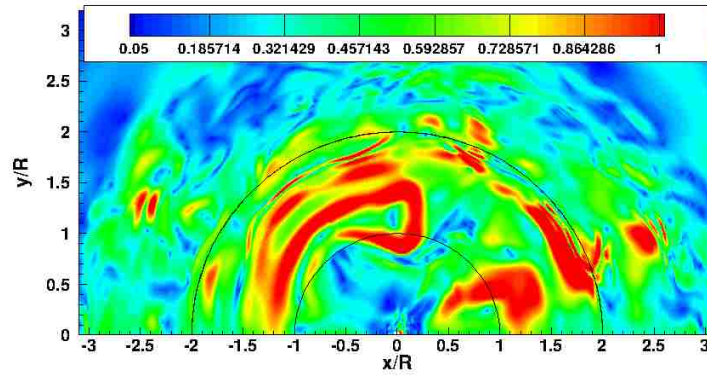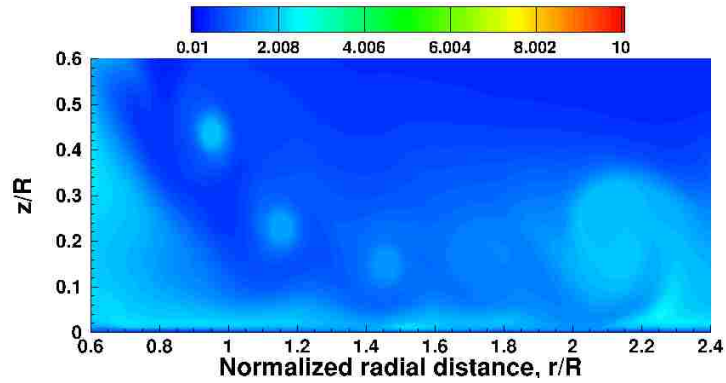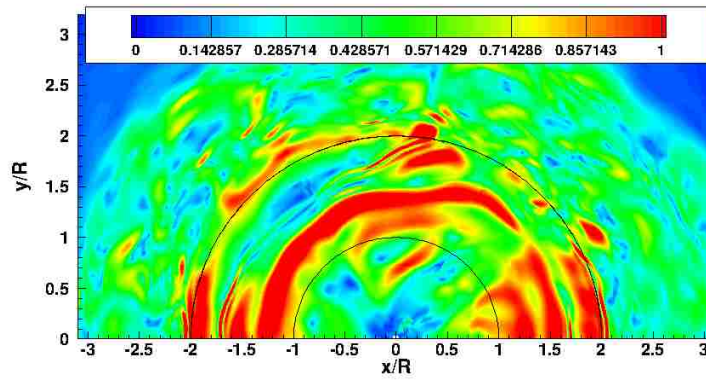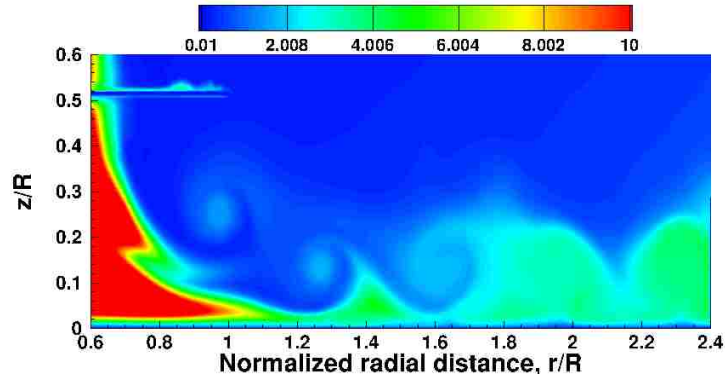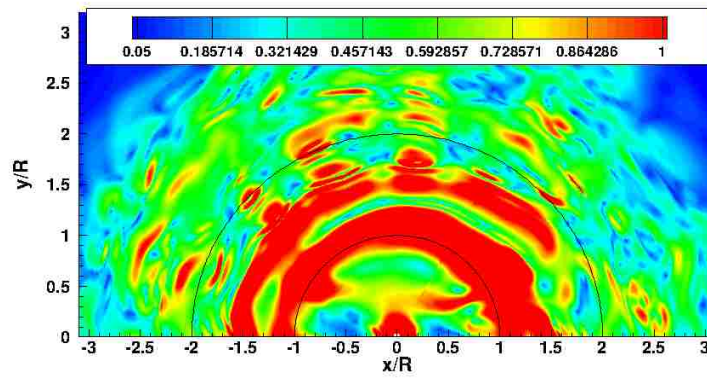show the ground-friction-velocity contours (normalized by tip speed) for the rotor heights of $1.5R$, $1.0R$, and $0.5R$ above the ground. The friction velocity contours show a striated pattern for all rotor heights, with high values directly below the tip vortex. The friction velocity is also seen to be higher for smaller rotor heights, for which the tip vortices were seen to come closer to the the ground as compared to that for larger rotor heights.

3.12 One-bladed Micro-Scale rotor

The previous sections described the computations from a two-bladed micro-scale rotor. Another case is described in this section that employs a one-bladed micro-scale rotor. The experiments on a one-bladed micro-scale rotor were performed by Baharani et al.[88]. The study of a one-bladed micro-scale rotor is advantageous compared to a multi-bladed rotor because the resulting flow field is less aperiodic. This enables the experimentalists to focus on the processes that affect the sediment uplift in the presence of a sediment bed rather than on the rotor parameters. The experiments were conducted on a rotor operating at a height of $1R$ above the ground. The blades are set at a collective pitch of 12 deg. A similar airfoil shape was used as described above for the two-bladed experiments. The aspect ratio of the blade was 4.052 and the rotor operated at a tip Mach number of 0.118 and a tip Reynolds number of $49,000$.

Table 3.5: Number of points used in various meshes for simulation for a $h/R = 1.0$.

Mesh	Dimensions	Mesh points (in millions)
Blade Mesh	$267 \times 93 \times 50$	1.2
Main Background Mesh	$247 \times 220 \times 315$	5.4
Overset Mesh 1	$367 \times 173 \times 146$	5.1
Overset Mesh 2	$367 \times 104 \times 21$	0.4
Overset Mesh 3	$367 \times 65 \times 21$	0.2
Overset Mesh 4	$367 \times 24 \times 21$	0.1
Total		29.11

3.13   One-blade Micro-Scale rotor setup

The mesh system for this case consists of a blade mesh, a main background mesh and a system of overset meshes. Modeling of a single rotor blade requires that the wake capturing meshes need to model the entire 360° of the domain contrary to modeling half the domain for a two-bladed rotor. This adds to the computational cost of CFD modeling. Table 3.33 shows the number of mesh points used in this computation. The grid spacing for all the different meshes and the computational setup remain similar for this case as described above for the two bladed rotor.

3.14   Results of the one-bladed micro-scale rotor case

The experiments measured an integrated thrust coefficient of 0.0087 while the computed thrust coefficient is 0.0095. Power values were not reported in the
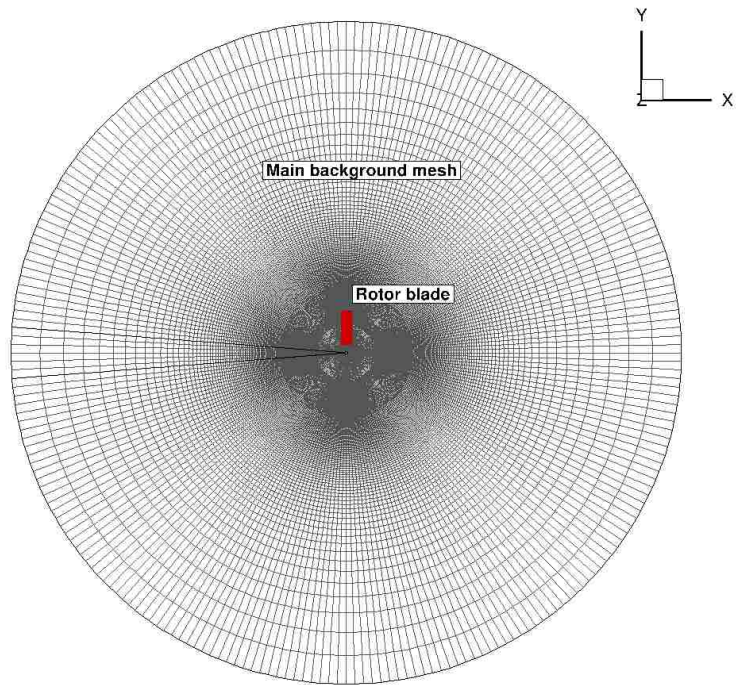
(a) Top view of the main background and blade mesh
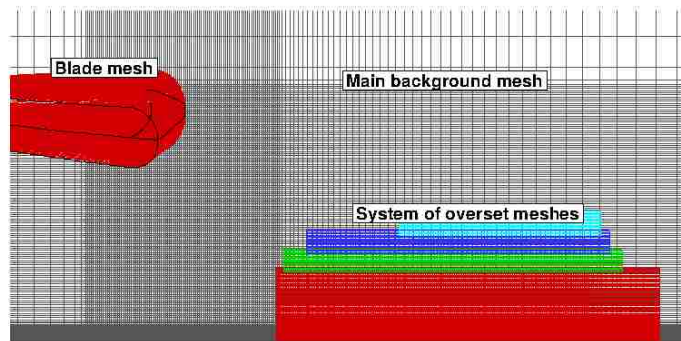
(b) Blade mesh, main background mesh, and a system of overset meshes for a rotor placed at $1R$ above the groundackground mesh

Figure 3.33: Mesh system for single bladed rotor system.
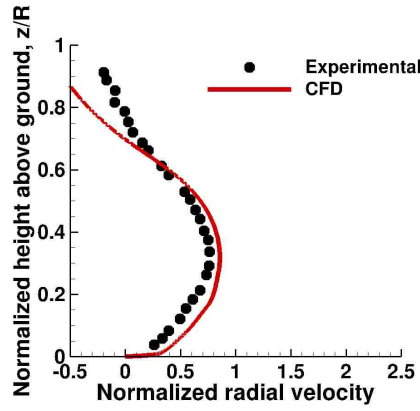
(a) $r/R = 0.8$
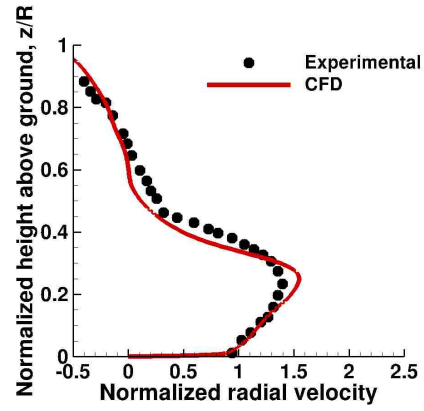
(b) $r/R = 1.0$
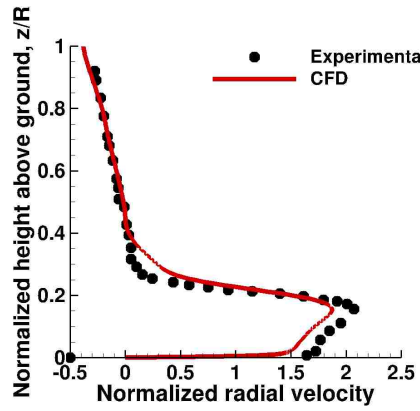
(c) $r/R = 1.25$
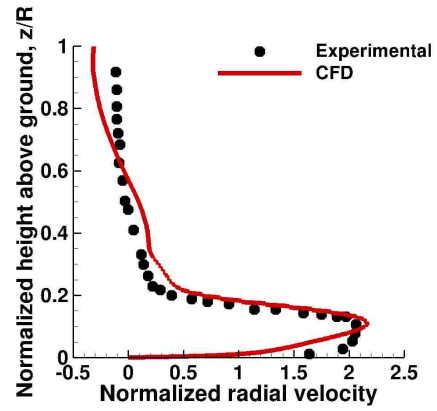
(d) $r/R = 1.5$
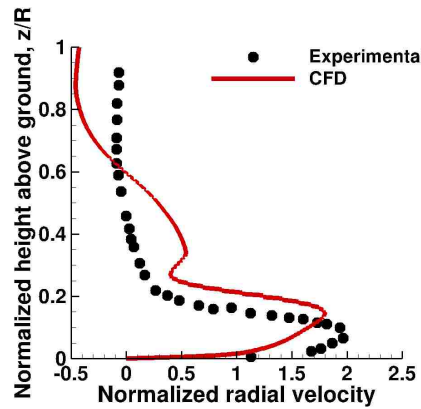
(e) $r/R = 1.75$

Figure 3.34: Comparison of CFD predicted time-averaged velocity profiles with exper imental data [48] at several radial locations for a rotor height of $h/R = 1.0$.

experiment. CFD predicted an integrated power coefficient of 0.00148. Furthermore, the time-averaged radial velocity profiles are compared at various radial locations. The wall jet height decreases as one moves outwards resulting in an increase of peak radial velocity. Notice that the agreement between the experimental measurements and the computational results has improved for this one-bladed rotor case at all radial locations as compared to the two-bladed case (shown in figs. 3.14). This is a result of the reduced aperiodicity in the rotor wake in experiments for the one-bladed case as each vortex is now shed off at a difference of 360° wake age compared to 180° wake age for the two-bladed case. This leads to reduced interaction (pairing or merging) between consecutively emanated vortices and provides a more periodic flow field.

3.15   Summary of Chapter

In this chapter, OVERTURNS was used to simulate a hovering micro-scale rotor operating at a very low tip Reynolds number in ground effect, with the primary objective of demonstrating its capability to provide good flow field predictions for a hovering rotor operating close to the ground. The simulations were performed using a system of overset meshes that are strategically placed to accurately capture the formation and evolution of the tip vortex to sufficiently long duration. The computations were validated with experimentally measured mean thrust and power. This was followed by a detailed validation of the tip-vortex flow field with the experimental particle-image-velocimetry data. In addition, the computational-fluid-

dynamics (CFD) data were used to explore the details of the wake characteristics, the wake trajectory, and the ground-wake interactions at various rotor heights. The detailed investigation of this two-bladed micro-scale rotor was followed by presenting CFD predictions for a single-bladed rotor. The next chapter will present the results from a hovering sub-scale rotor IGE.

Chapter 4

Sub-Scale Rotor Modeling

In this chapter, results are shown from the computations performed on a hovering sub-scale rotor operating in ground effect(IGE) at a rotor height of $1R$ rotor radius above ground. The sub-scale rotor is twice the aspect ratio of the micro-scale rotor. The challenges in capturing the sub-scale rotor wake are addressed by modifying the existing turbulence model. Different tip shapes are tested on the sub-scale rotor and their resulting wake is compared in details with available experiments. Flow field is analyzed close to the ground to understand the effect of rotor wake interaction with the ground plane.

4.1   Sub-Scale Rotor Configuration

The experimental setup of Milluzzo et al.[50] shown in Figure 4.1 is used to validate the flow field of a hovering one-bladed rotor operating in-ground effect(IGE). The rotor consisted of an untwisted rectangular blade with NACA 2415 airfoil. The rotor blade had a chord length of 44.5mm and a radius of 0.408m resulting in an aspect ratio of 9.132. The blades were operated at a collective pitch of 4.5^0. The rotor operated at a tip Mach number of 0.24 and a chord Reynolds number of $250,000$. The experiments were performed on four different blades obtained by varying the blade tip shapes. The rotor blades operated at a rotor height of $1R$
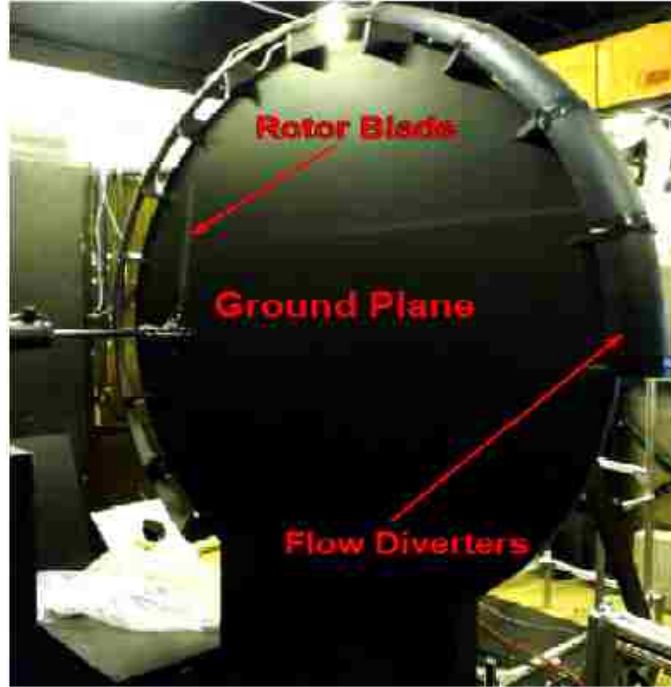
Figure 4.1: Experimental setup of 1-bladed sub-scale rotor of Milluzzo et al.

above the ground.

4.2 Mesh System for Sub-Scale Rotor Modeling

4.2.1 Blade meshes for four different tip shapes

The blade mesh comprises of a body conforming C-O type mesh. Figure 4.2(a) shows the four experimental blades with their varying blade tips. For validation purposes, the computational blade meshes are generated to match the surface geometries as seen in figure 4.2(b). The first type of blade consists of the rectangular tip. The second type is the swept tip consisting of a 20^0 leading edge sweep angle beginning at 78.95% of span. The third type is a BERP-like tip [50] which is generated by placing varying airfoil sections along the span of the blade beyond 84.2% of

the span. The computational BERP-like tip uses uses a finite chord in the last cross section of the blade, unlike the experiments. A finite chord length is maintained at the tip for obtaining non negative cell volumes while the C sections collapse to close the tip in the computational mesh. The fourth type of tip shape used in the experiments is the slotted tip. A slotted tip is constructed to eject momentum in the flow field with the purpose of diffusing vorticity. The experimental slotted tip blade comprised of four internal slots of circular cross section. The slots connected the leading edge of the blade to its side edge, shown in Fig. 4.3. The computational slotted tip uses slots with a square cross section to avoid the cell volumes from going to zero at the center. Figure 4.3 shows the slotted tip blade used in the computations. The cross-sectional areas of the slots are matched with the values used in the experiments. The center of each slot follows a trajectory starting from the leading edge to the side edge, and is used to place 2-D square cross-sections to form the slot meshes. The slot meshes extend out both from the leading edge and the side edge into the blade mesh to ensure that there is a sufficiently large fringe layer for the exchange of information between the blade mesh and the slot mesh.

4.2.2 Overset Meshes for Wake Capturing

The earlier chapter showed the details of the rotor wake in-ground effect for the micro-scale rotor using 28 million points. For capturing a similar resolution of tip vortices in the flow field of the sub-scale rotor system, one would require 128 million points. This leads to a prohibitive calculation with the available compu-
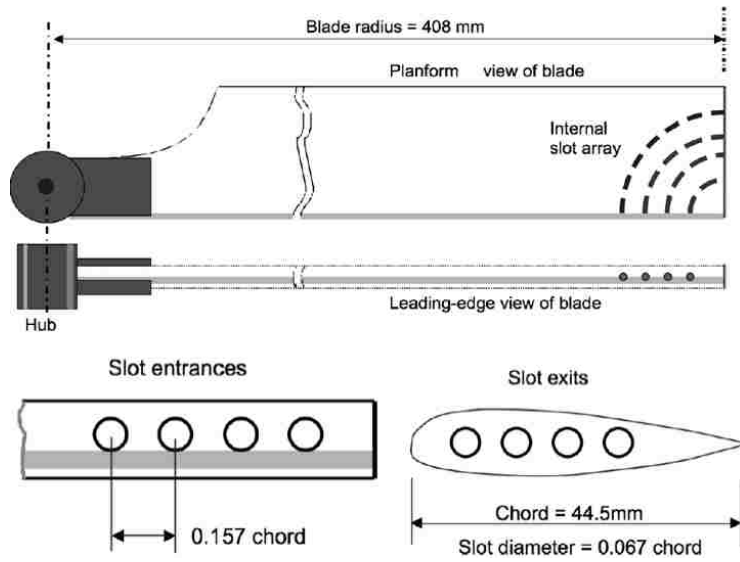
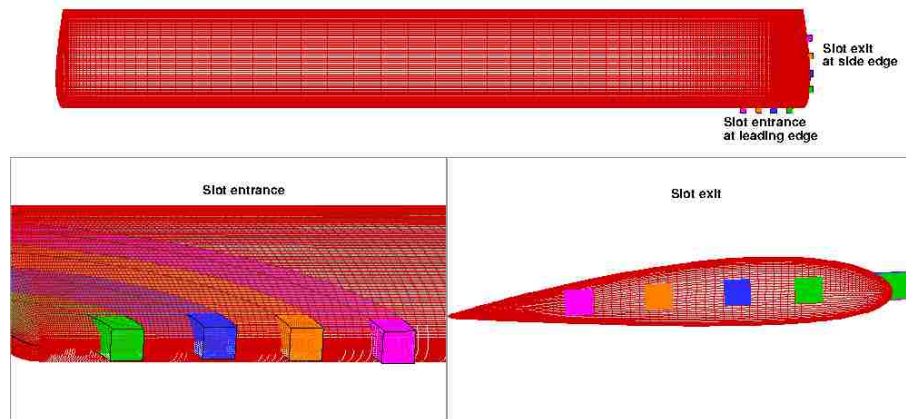(a) Experimental blades
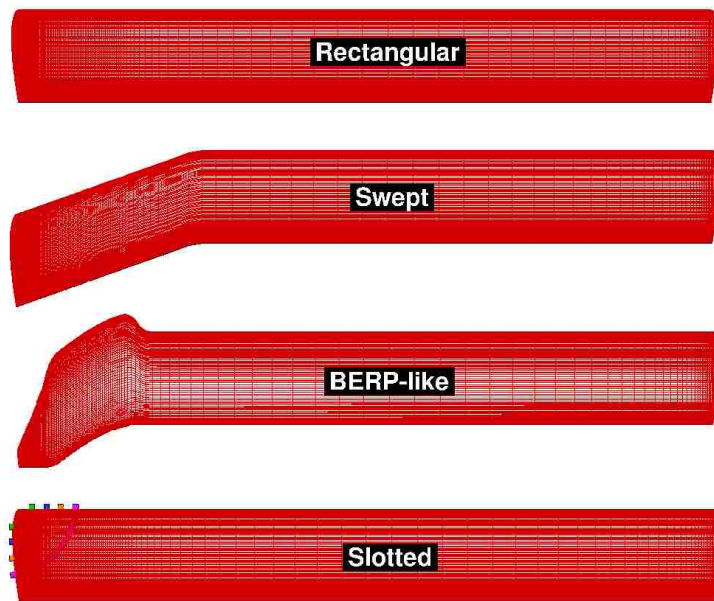
(b) Computational blades

Figure 4.2: Four different blade tips for comparison.

(a) Experimental slot mesh


(b) Computational slot mesh

Figure 4.3: Experimental and computational slot tips.

tational resources. Consequently, a new mesh methodology is developed for the current sub-scale rotor mesh system. First, the wake capturing is done by using a single cylindrical background mesh (figure 4.4(a)) and the simulation is performed for fifteen revolutions. The background mesh has a constant spacing of $0.04c$ in the radial direction between $0.8R$ to $2.0R$. The flow field is reasonably well developed after fifteen revolutions. It is then used to obtain the instantaneous tip vortex trajectory by searching for maximum vorticity magnitude corresponding to the vortex center at all wake ages. Once the tip vortex trajectory is obtained, the background mesh is modified to follow the path of the rotor wake to reduce the number of mesh points in the radial direction. The resulting modified background mesh is shown in 4.4(b) and is referred as the main background mesh.

In addition to the strategic refinement of the main background mesh, a vortex tracking grid (VTG), seen in figure 4.5(a) is used to better the preserve the tip vortices along the path of the rotor wake. The VTG is a three dimensional helical mesh, which is generated by azimuthally extruding a 2-D Cartesian plane along the instantaneous tip vortex trajectory. These 2-D planes are placed at every $1.0°$ of the azimuth, which is two-thirds the azimuthal distance in the background mesh. The 2-D planar section of the VTG is a Cartesian mesh with equi-spaced mesh points near the middle, which stretches at the edges to reduce the cell size disparity between the VTG and the main background mesh. The extent of the 2-D plane is calculated by accounting for the expected wandering of the tip vortex. At the edge of the VTG, the cell spacing is equal to that in the new background mesh, while at the center the cell spacing is approximately one-fourth. If the VTG is obtained by using an
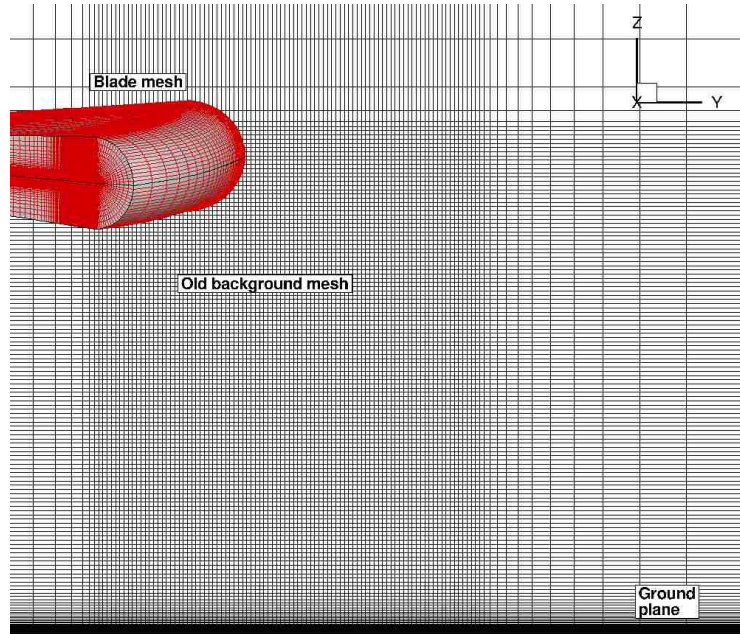
(a) Initial mesh system for the first fifteen revolutions
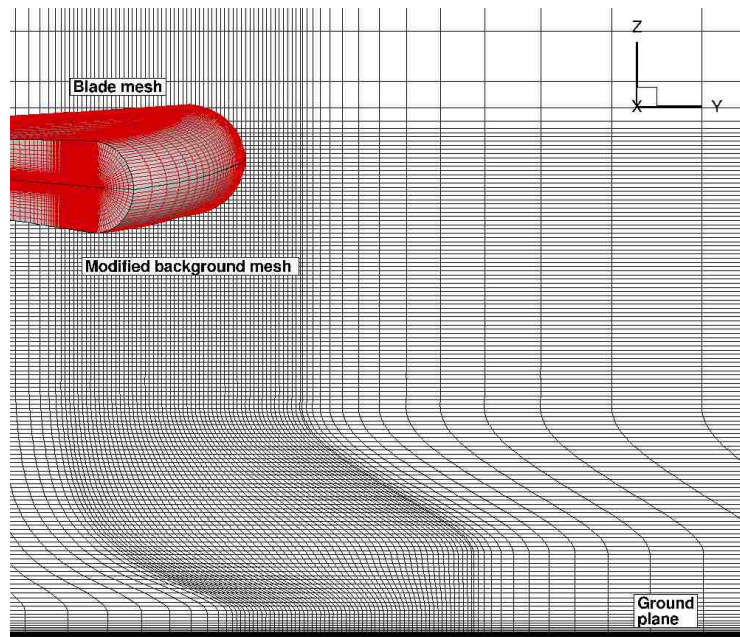
(b) Modified background mesh after first fifteen revolutions

Figure 4.4: Main background mesh modification.

Table 4.1: Number of mesh points for sub-scale rotor operating at $h/R = 1.0$.

Mesh	Dimensions	Mesh points (in millions)
Blade Mesh	$267 \times 185 \times 51$	2.52
Main Background Mesh	$247 \times 241 \times 341$	19.11
Vortex Tracking Grid	$145 \times 145 \times 1336$	28.21
Funnel Mesh	$367 \times 100 \times 325$	11.96
Total		61.82

instantaneous tip vortex trajectory, the resulting grid contains irregularities along the azimuth direction. These irregularities are damped out by using a Laplacian based smoothing.

The resolution of the vortices close to the ground is further improved by using a funnel mesh as in figure 4.5(b). The cross-sectional limits of the funnel mesh are based on the instantaneous tip vortex trajectory. It can be observed that the mesh is following a radially outward path as the vortices move radially outward close to the ground. The cell spacing in the azimuth direction is two-thirds of the main background mesh. The radial and vertical directions are refined twice as much as the main background mesh.

The combination of the blade mesh, main background mesh, vortex tracking grids and funnel mesh shown in fig. 4.6 form the complete mesh system for wake capturing. Table 4.1 shows the number of points in each type of mesh for the one-bladed sub-scale rotor cases.
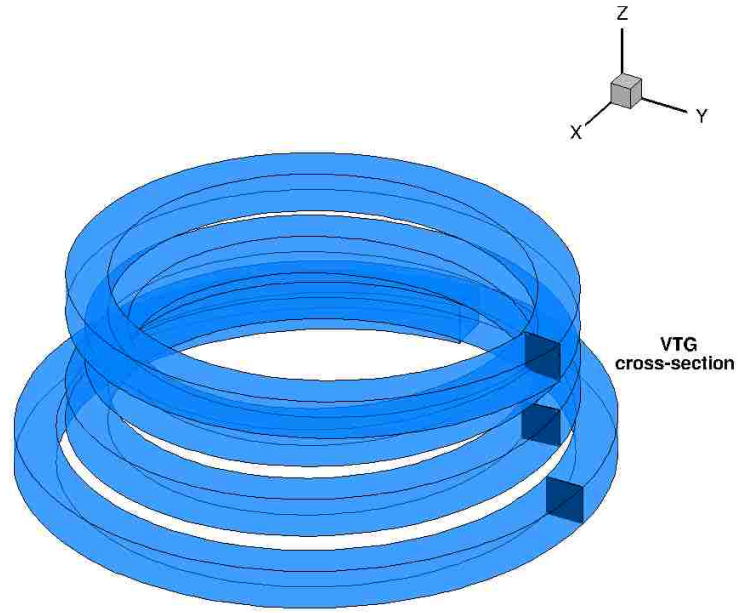
(a) Vortex tracking grid (VTG)
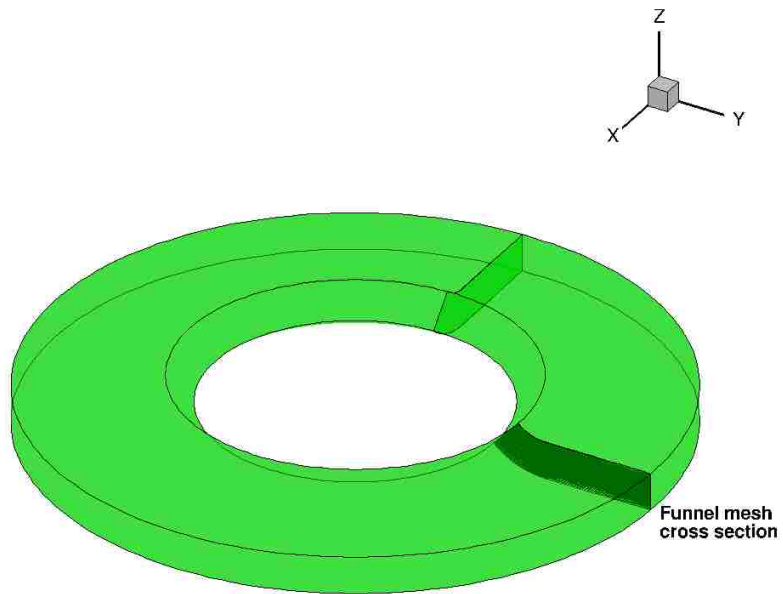
(b) Funnel mesh

Figure 4.5: Additional overset meshes.

Figure 4.6: Complete mesh system.

4.3 Sub-scale Rotor Setup Parameters and Computational Costs

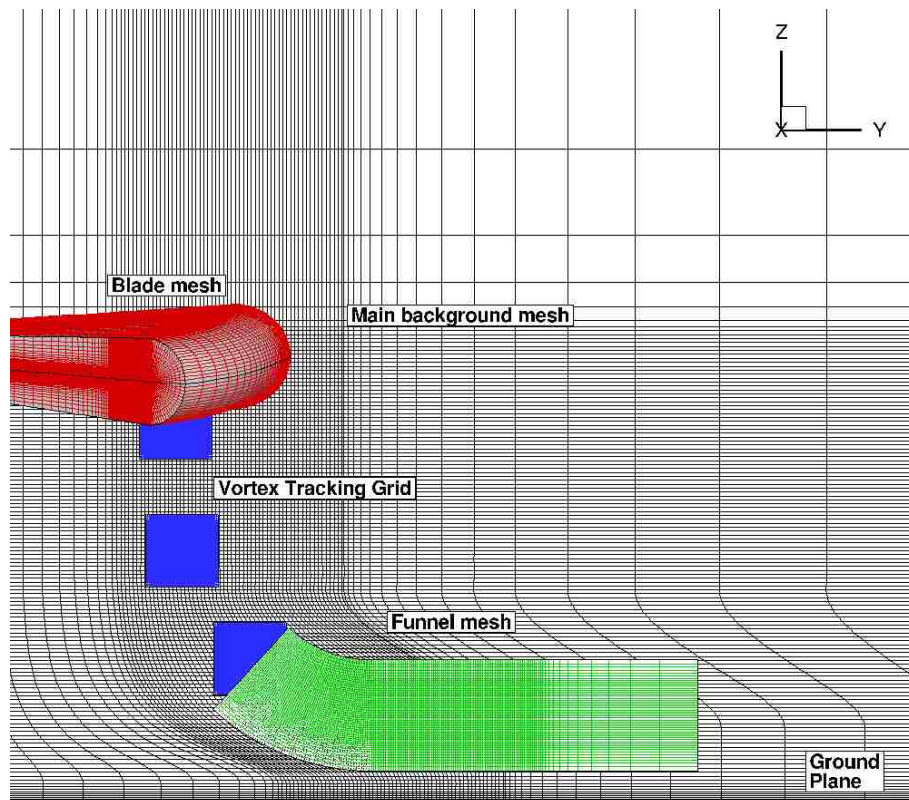The sub-scale rotor simulations employ the LUSGS method for inverting the system of equations as described in Chapter 2. The chosen time-steps correspond to 0.25^0 of azimuth for all the calculations. A constant CFL number is maintained along with a time step size of 10 for the Newton sub-iterations to provide stability throughout the iterations. In addition, at each time step, 6 sub-iterations are used to remove linearization errors. The preconditioning Mach number is set to the local Mach number contrary, to the tip Mach number used for the micro-scale rotor simulations. This is seen to improve convergence for the sub-scale rotor cases. Each simulation is run for a total of 19 revolutions. The first 15 revolutions only use the modified main background mesh and the funnel mesh and then the vortex tracking grids are added for another 4 revolutions. The VTGs are modified at each revolution during these last 4 revolutions. The calculations take about 6.25 days to complete 19 revolutions (ie. 3.04 revs per day) when run in parallel on 32 AMD Interlagos Opteron 2.3 GHz processors. A total of 240 processors were utilized in each of these simulations.

4.4 Performance Validation

The variation of spanwise thrust and power is plotted in figure 4.7 for all the tip shapes. As expected, the thrust and power values increase across the span because of the increasing rotational velocity of the rotor blade. At the tip of the rotor blade, the drop in thrust and power values signifies the presence of the tip

vortex. Note that in figure 4.7(b) the BERP-like tip shows an increase in power at the 84.2% span location followed by a sharp decrease in power values. This variation follows the change in the chord length for the BERP-like tip beyond 84.2% span as described in the geometry section earlier. For the slotted tip, an increase in power values beyond 50% span is observed compared to the other three tip shapes. This increase can be attributed to the higher power requirements in the presence of the slotted tips.

To gain confidence in the predictive capability of CFD methodology, the predictions of the integrated thrust and power are compared with available experiments. Table 4.2 shows the comparison of the predicted thrust along with the experimentally measured thrust coefficient; the predicted power coefficients are also tabulated. Note that the experimental and computational thrust values are in good agreement for the rectangular and swept tip. The BERP-like tip shows a 17% higher thrust value in the experimental measurement as compared to that calculated from the simulations. A possible reason for this discrepancy can be attributed to the difference in the finite radius at the blade tip in the computational mesh. Furthermore, the slotted tip in the computations predicts a much higher thrust value than that measured in experiments.

As mentioned, the CFD predicted rotor power coefficient is also shown in the table; whereas the experiments did not measure the power values. The rectangular, swept and BERP-like tip show similar power values. The slotted tip case shows a 22% higher power than the rectangular tip case.
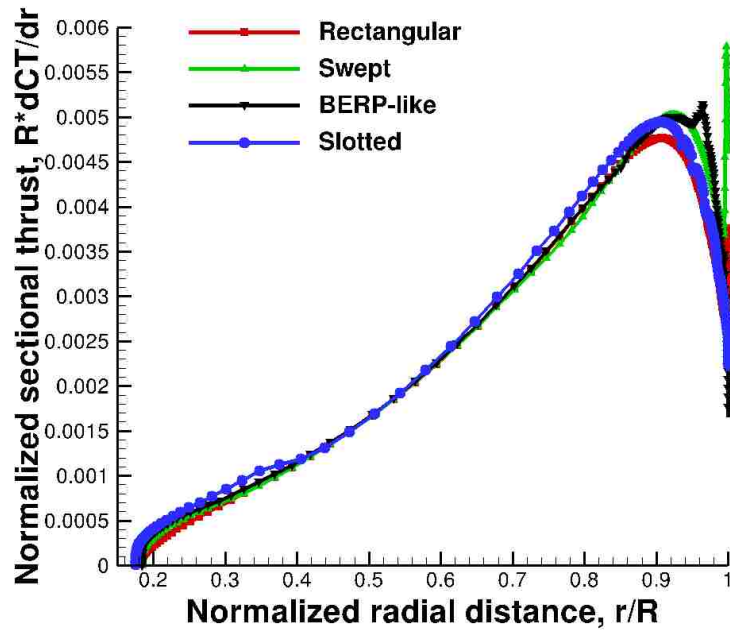
(a) Thrust coefficient
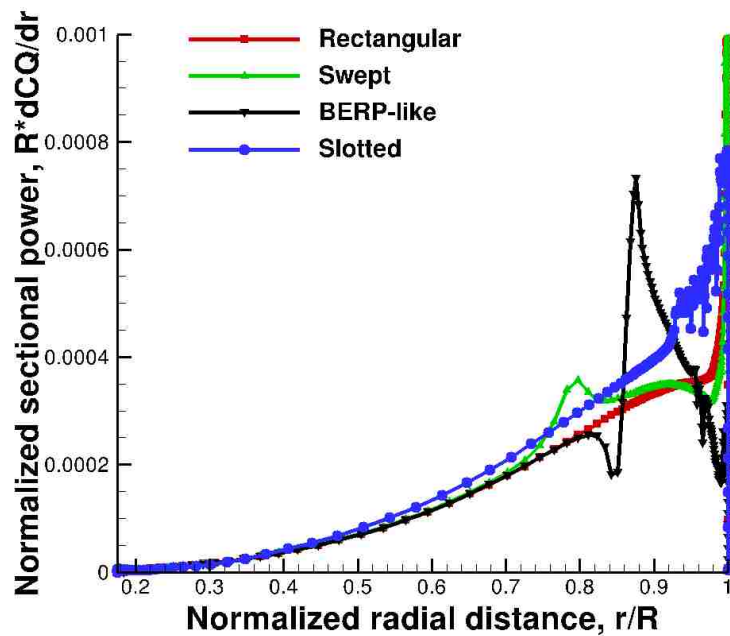
(b) Power coefficient

Figure 4.7: Spanwise variation of performance parameters for various tip shapes.

Table 4.2: Thrust and power comparison with experiment [50] for various rotor tip shapes.

| Blade tip shape	C_T (Computed)	C_T (Experimental)	C_P (Computed)
Rectangular	0.0019	0.0018	0.000122
Swept	0.0020	0.0020	0.000130
BERP-like	0.0019	0.0023	0.000127
Slotted	0.0020	0.0014	0.000149

4.5   Tip Vortex Characteristics

Following the performance comparison, one can get an estimate of the tip vortex characteristics by calculating the circulation, peak swirl velocity and core radius at various wake ages for the simulations and comparing with the experimental data. Figure 4.8 shows the variation of circulation values with different wake age for both the experiments and the computations, respectively. Circulation is non-dimensionalized by the tip speed and rotor radius. The experimental results in figure 4.8(a) show a slightly higher value of the circulation for the BERP-like blade compared to the rectangular and swept tip shapes. However, in the computations in figure 4.8(b), the circulation levels remain fairly constant with varying wake age for the rectangular, swept and BERP-like blades. This is expected because the total amount of thrust predicted in the computations is similar for the three tip shapes; whereas, the experiments measured a slightly higher thrust value for the BERP-like blade. The circulation for the slotted tip experiment was measured until only a

143

wake age of 270^0 due to the difficulty in identifying the highly diffused vortex core after that wake age. The computations face a similar issue and the circulation is predicted until 500^0, beyond which the vortex core is hard to identify.

Figure 4.9 shows the comparison of the experimental measurements and computational results for the variation of peak swirl velocity with wake age. The peak swirl velocity is non-dimensionalized by the tip speed of the rotor blade. The experiments show a decrease in peak swirl velocity until a wake age of 360^0. This is followed by a slight increase in peak swirl velocity for the rectangular, swept and BERP-like tip cases, due to in-ground effect. Compared to the experiments, the computations show a rapid decrease in peak swirl velocity with increasing wake age. Even at an early wake age of 180^0, the peak swirl velocity predicted by the computations is twice as low as the experimental values for the rectangular tip case. Similarly, this pattern is observed for the swept and BERP-like tip as well and this shows that the RANS computations are consistently under-predicting the peak swirl velocity values. However for the slotted tip, the peak swirl velocity is considerably lower in the experiments as compared to the computations especially at early wake ages. This implies that the slots in the computations are not able to inject enough turbulence into the flow field such that it eventually diffuses the vortex cores, as observed in the experimental results. Because of the highly diffused vortex cores in the slotted tip case, one cannot calculate the peak swirl velocity values at lateer wake ages.

Figure 4.10 shows the variation of the vortex core radius as a function of wake age for the different tip shapes. The core radius is non-dimensionalized by
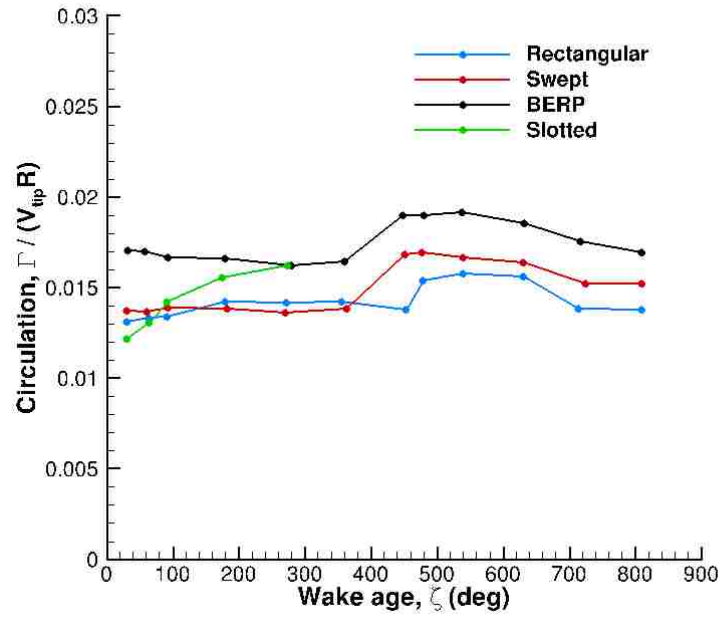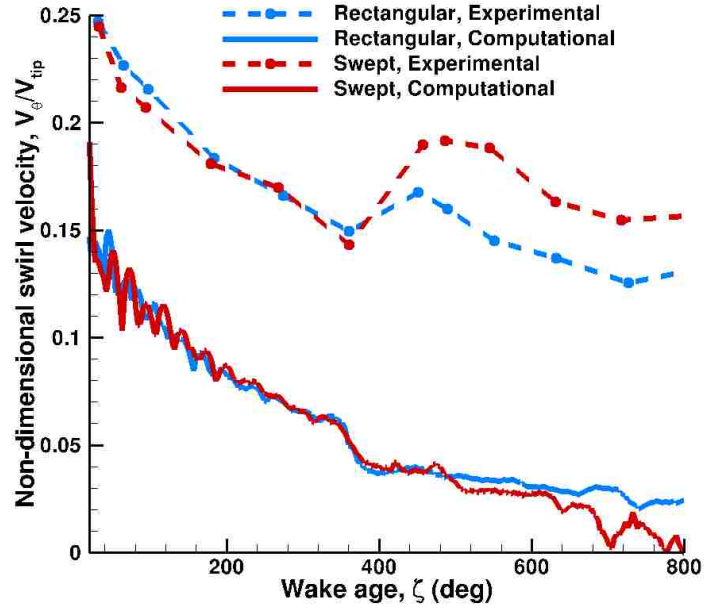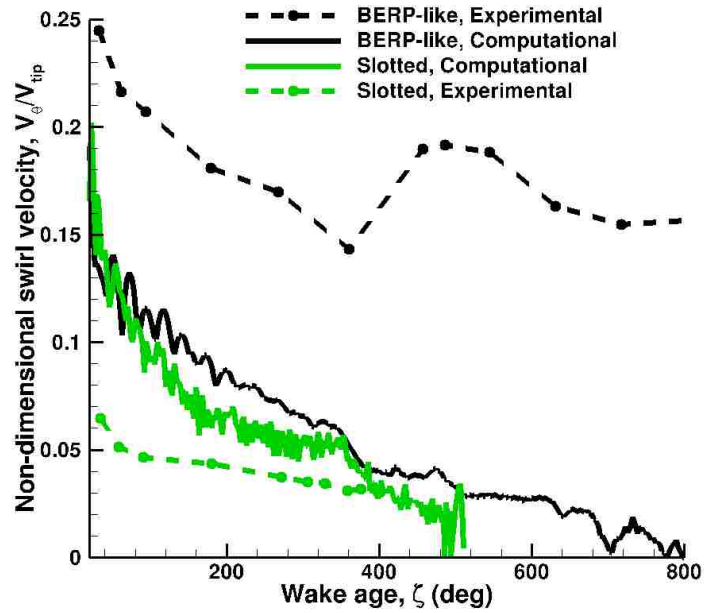
(a) Experimental, circulation
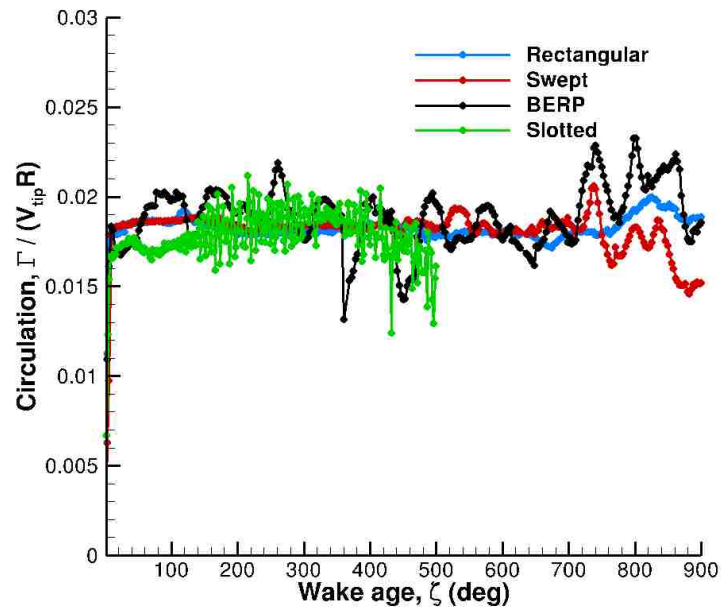
(b) Computational, circulation

Figure 4.8: Comparison of CFD (RANS) predicted circulation as a function of wake age for different tip shapes.
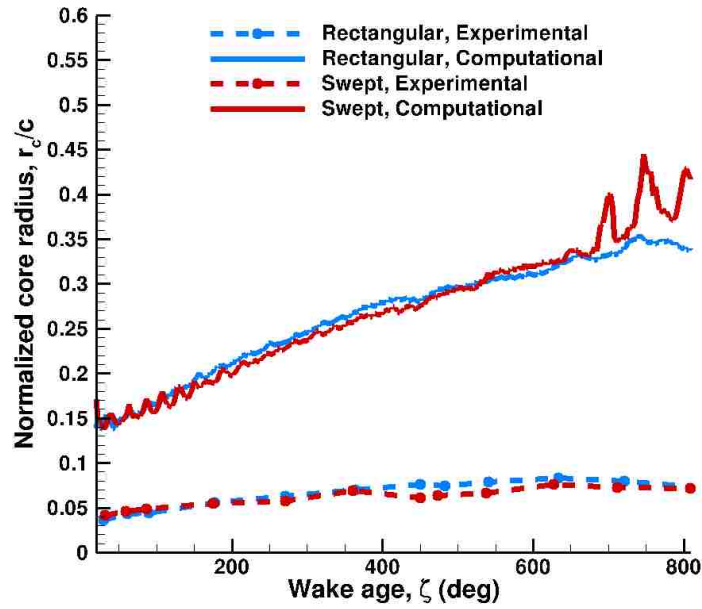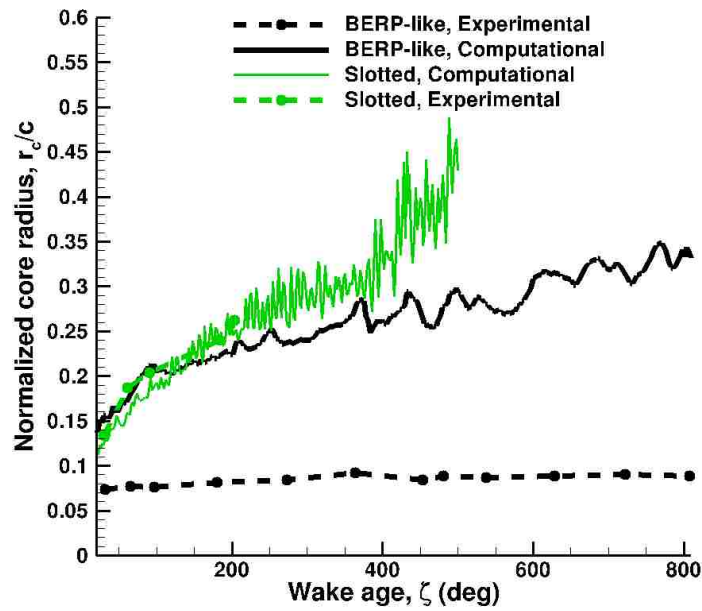
(a) Experimental, peak swirl velocity

(b) Computational, peak swirl velocity

Figure 4.9: Comparison of CFD (RANS) predicted peak swirl velocity as a function

of wake age for different tip shapes.

(a) Experimental, core radius

(b) Computational, core radius

Figure 4.10: Comparison of CFD (RANS) predicted peak swirl velocity as a function of wake age for different tip shapes.

the rotor blade chord. It can be noticed that the core radius grows much faster in the computations as compared to the experimental results, for all tip shapes. For instance, the core radius at the 720° wake age in the computations grows to an order of 0.3 chords for the rectangular tip, while the experiment only has a core size of the order 0.075 chords.

The results from the peak swirl velocity and core radius values show that the tip vortices are not being captured well, even at early wake ages, in the RANS computations; thus, further investigation of the CFD methodology is necessary.

## 4.6   Modeling Difficulties with Sub-scale Rotor

In chapter 3, the micro-scale rotor regime simulations were validated with an excellent agreement with available experimental results. However, the sub-scale rotor predictions do not show a good agreement with the experimental results and the vortices are seen to diffuse too much at early wake ages. The difficulties in obtaining reasonable agreement for the sub-scale regime compared to the micro-scale rotor regime (operating at $1R$ rotor height) can be understood in detail by examining the eddy viscosity contours for both cases. Figure 4.11 shows the computed eddy viscosity contours at a wake age of 0^0 for both the micro-scale rotor and the sub-scale rotor, respectively. It can be observed that the flow is close to laminar for the micro-scale rotor except for the region close to the ground. However, the sub-scale rotor computations show a much more highly turbulent flow field. One can even observe high levels of eddy viscosity at the center of the vortex cores; whereas

theoretically, the vortex cores are expected to be laminar in nature[64]. This implies that the turbulence model (i.e. the Spalart-Allmaras turbulence model with rotational correction) being used in the RANS equations to solve for the eddy viscosity values is leading to an excessive diffusion of the vortex core.

It is a known fact that the RANS equations were formulated to predict attached or thin shear layer flows well. This causes modeling limitations using the RANS equations when predicting flows that involve large amounts of flow separation. For such flows, a higher fidelity approach, such as LES (Large Eddy Simulation), is expected to be more suitable. Section 2.4 discusses the differences between the LES and RANS approaches. Since the LES approach is seen to be prohibitively expensive for practical engineering applications, one way to use a higher level of approximation to account for turbulence above that in RANS is to use a hybrid approach between LES and RANS. In a hybrid approach, the boundary layer/near wall regions (small scale turbulence) are modeled using RANS and regions of massive separation (large scale turbulence) are resolved using LES. The existing RANS methodology can be extended to include the hybrid approach by modifying the distance function in the S–A model. The modified distance function is based on grid spacing, to provide the switch between the RANS and LES limits. Accordingly, a grid spacing based limiter approach was developed by Spalart et al. [89] and is referred to as Dettached Eddy Simulations (DES) [89]. To apply, DES a simple modification to the distance function, d, is made in the S–A turbulence model that depends upon both the wall
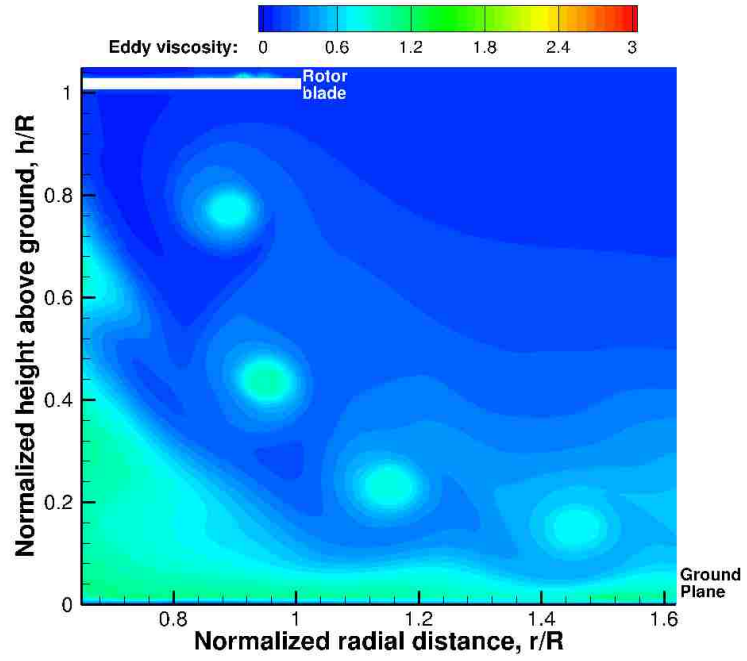
(a) Micro-scale rotor
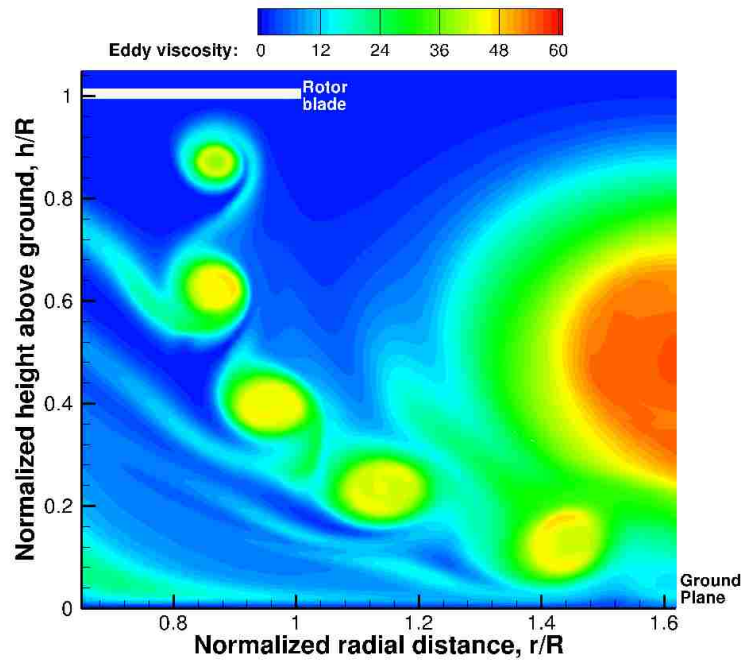
(b) Sub-scale rotor

Figure 4.11: Comparison of CFD (RANS) predicted eddy viscosity contours at an azimuthal plane of 0^0.

distance and the local grid spacing. The modified distance function is:

$$\tilde{d} = min(d, C_{DES}\Delta) \tag{4.1}$$

where, C_{DES}=0.65 and Δ is given by:

$$\Delta = max(\Delta x, \Delta y, \Delta z) \tag{4.2}$$

Note that the Δ function described above is based on the maximum of the grid spacing and is designed to work well for isotropic grids. In the current work, the grid spacing is highly anistropic especially for the vortex tracking grids. The minimum grid spacing in the VTGs for the sub-scale rotor consists of a spacing of $0.01c$ in the vertical and radial direction while the maximum grid spacing in the azimuthal direction is approximately 0.16 chords (1° of azimuth). This leads to a maximum value of the aspect ratio for the VTGs to be 16 : 1. This means that the isotropic definition of the Δ function would not hold true for such a highly anistropic grid system. Scotti et al. [92] define a modified value of the Δ function that accounts for anistropy of the grids and is defined as:

$$\Delta = f(a_1, a_2) \times max(\Delta x, \Delta y, \Delta z)^{\frac{1}{3}} \tag{4.3}$$

$$f(a_1, a_2) \approx \cosh\sqrt{\frac{4}{27}[(\ln(a1))^2 - \ln(a1)\ln(a2) + \ln(a2)^2)]} \tag{4.4}$$

where a_1 and a_2 are the aspect ratio of the grid. They showed that such a grid spacing function is more appropriate for LES.

Furthermore, the application of DES in cases with thick boundary layers or shallow separation regions causes the local grid spacing even inside the boundary

layer to get chosen in the modified distance function; this results in an early onset of the LES mode. This causes a reduction in the eddy viscosity levels and this phenomena is termed as "Modeled Stress Depletion". To overcome this issue in DES, Spalart et al. [90] introduced Delayed Dettached Eddy Simulations (DDES). The modified distance function based on DDES depends on:

$$\tilde{d} = d - f_d \max(d, C_{DES}\Delta) \tag{4.5}$$

where

$$f_d = 1 - tanh([8r_d]^3)$$
$$r_d = \frac{\nu_t + \nu}{(U_{i,j}U_{i,j})^{0.5}k^2d^2} \tag{4.6}$$

and $U_{i,j}U_{i,j}$ is the inner product of the velocity gradient tensor, k is the Kármán constant, ν_t is the kinematic eddy viscosity, ν is the molecular eddy viscosity, and d is the distance to the wall. Such a formulation results in r_d dropping to zero towards the edge of the boundary layer, giving f_d a value of one there and thus transitioning to the LES mode. Inside the logarithmic layer r_d=1 making f_d=0, ensuring that the RANS mode is activated.

This modified distance function has been implemented into the S–A turbulence model in the OVERTURNS solver and the computations for the sub-scale rotor are subsequently revised. The results from the revised computations are referred to as obtained from the SA-DDES methodology. The following sections discuss the results of the revised computations.

4.7 Revised computations with SA-DDES methodology

The modeling difficulties noticed earlier in the computations using the S–A turbulence model in the RANS equations are overcome by employing the SA-DDES methodology. To gain confidence using the SA-DDES methodology, the turbulence levels are compared between the S–A and SA-DDES formulations in the revised computations and figure 4.12 shows the eddy viscosity levels from both simulations for the sub-scale rotor.

Note that the levels of eddy viscosity have dropped by almost an order of magnitude. The location of the tip vortices in both the S–A and SA-DDES results look similar for early wake ages; however, with the additional diffusion occuring in the S–A results, the tip vortex locations start to differ. In addition to that, the vortex centers are seen to be more laminarized, as expected theoretically [64], using the SA-DDES methodology. Further, a computation is performed using the SA-DDES methodology with the micro-scale rotor blade. It is observed that the levels of eddy viscosity are lower for the SA-DDES computation as compared to the results from the S–A computation (fig. 4.13) but not to the same extent as observed for the sub-scale rotor. Note that the micro-scale rotor operates at a much lower tip Reynolds number of $32,500$ where the viscous effects are more dominating, compared to a tip Reynolds number of $250,000$ for the sub-scale rotor. Since the laminar viscous effects dominate in the case of the micro-scale rotor the S–A turbulence modeling is sufficient to not let the vortices diffuse to a large amount, as compared to the too large diffusion observed during the S–A turbulence modeling of the sub-scale rotor.
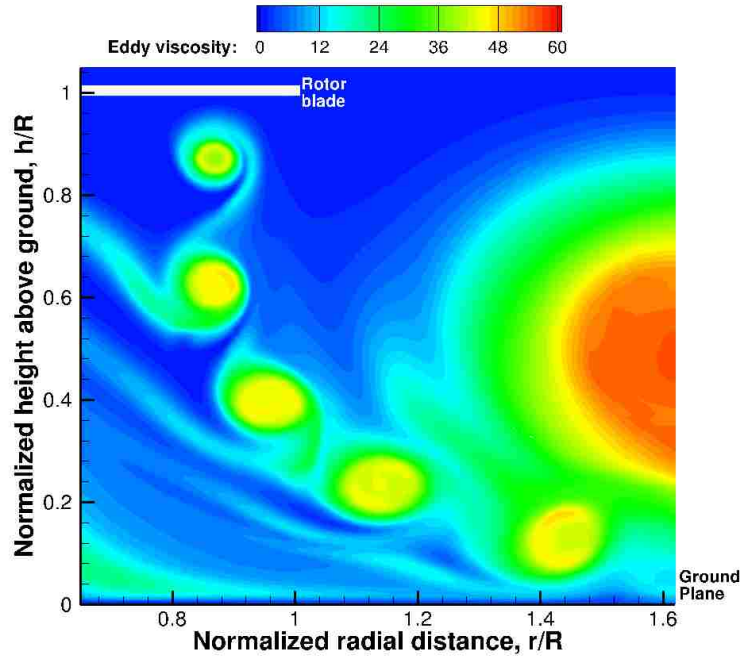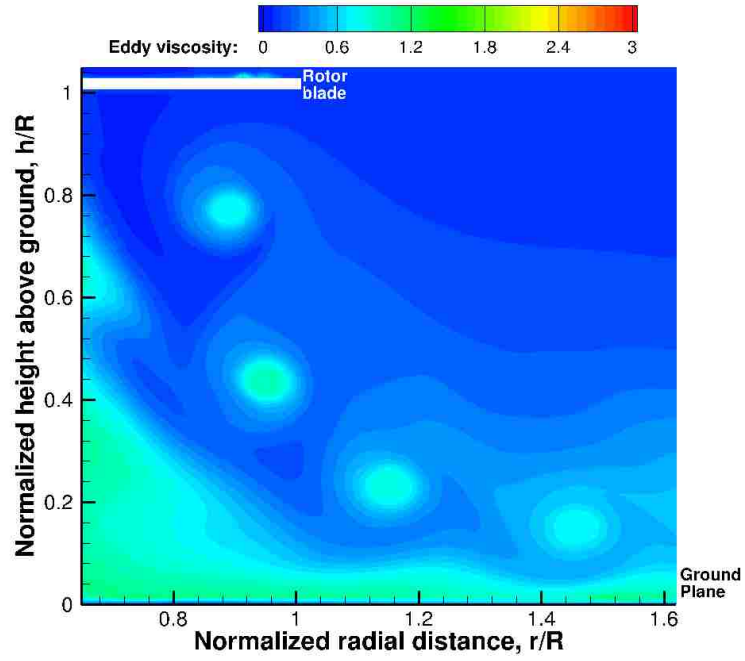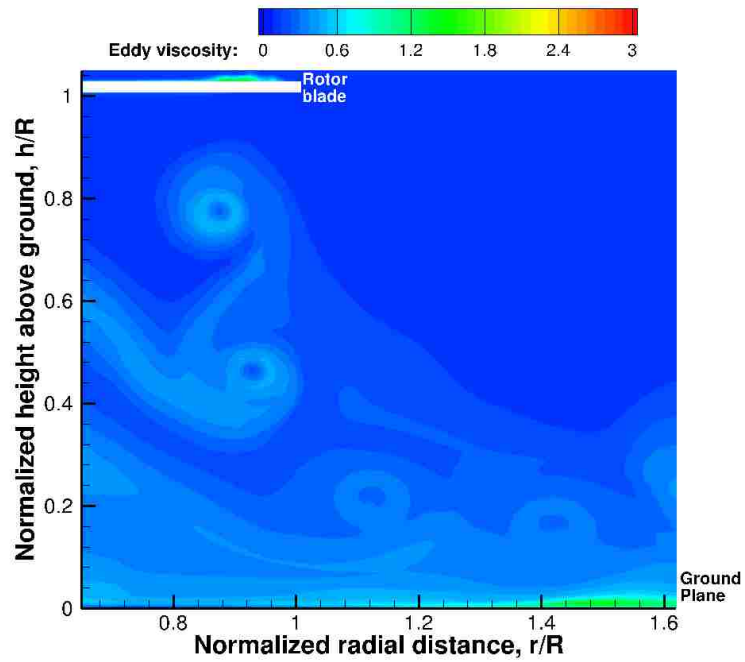
(a) Sub-scale rotor with S–A simulation
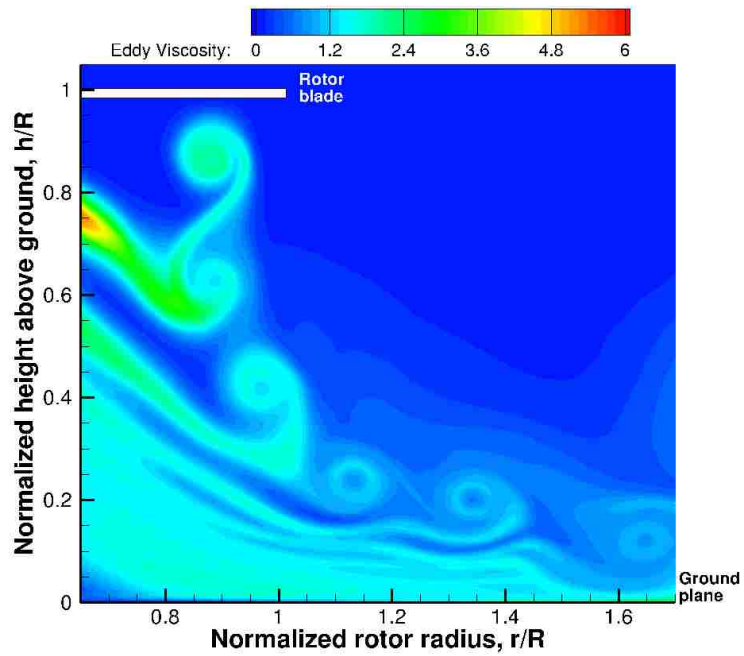
(b) Sub-scale rotor with SA-DDES simulation

Figure 4.12: Comparison of CFD predicted eddy viscosity contours at an azimuthal plane of 0^0 for the sub-scale rotor.

(a) Micro-scale rotor with S–A simulation

(b) Micro-scale rotor with SA-DDES simulation

Figure 4.13: Comparison of CFD predicted eddy viscosity contours at an azimuthal plane of 0^0 for the micro-scale rotor blade.

The SA-DDES methodology is clearly required for the sub-scale rotor simulations.

The next few sections in this chapter will discuss the results from the revised computations for the hovering 1-bladed sub-scale rotor with the SA-DDES methodology in detail.

4.8   Performance Validation and Computational Setup of SA-DDES simulations

The peformance results (both spanwise and integrated) using the SA-DDES methodology are not significantly different from the ones predicted by the S–A methodology (not shown). Note that the computational cost of the SA-DDES implementation provides an insignificant change from the S–A turbulence model based computations, since one is only solving for a few more analytical equations as shown in section 4.6.

4.9   Tip Vortex Formation

Looking at the computed flow fields provides a more detailed qualitative insight into the tip vortex formation process for the different blade tips. Figure 4.14 shows the vorticity magnitude contours at various chordwise locations for the four blade tips. The blade mesh is clustered at the tip to accurately capture the tip vortex. Notice that in figures 4.14(a) and (b), the tip vortices emanating from the rectangular and swept tip have similar vortex strength. In contrast, the BERP-like tip shown in fig. 4.14(c) has a reduced vortex strength. Furthermore, the slotted
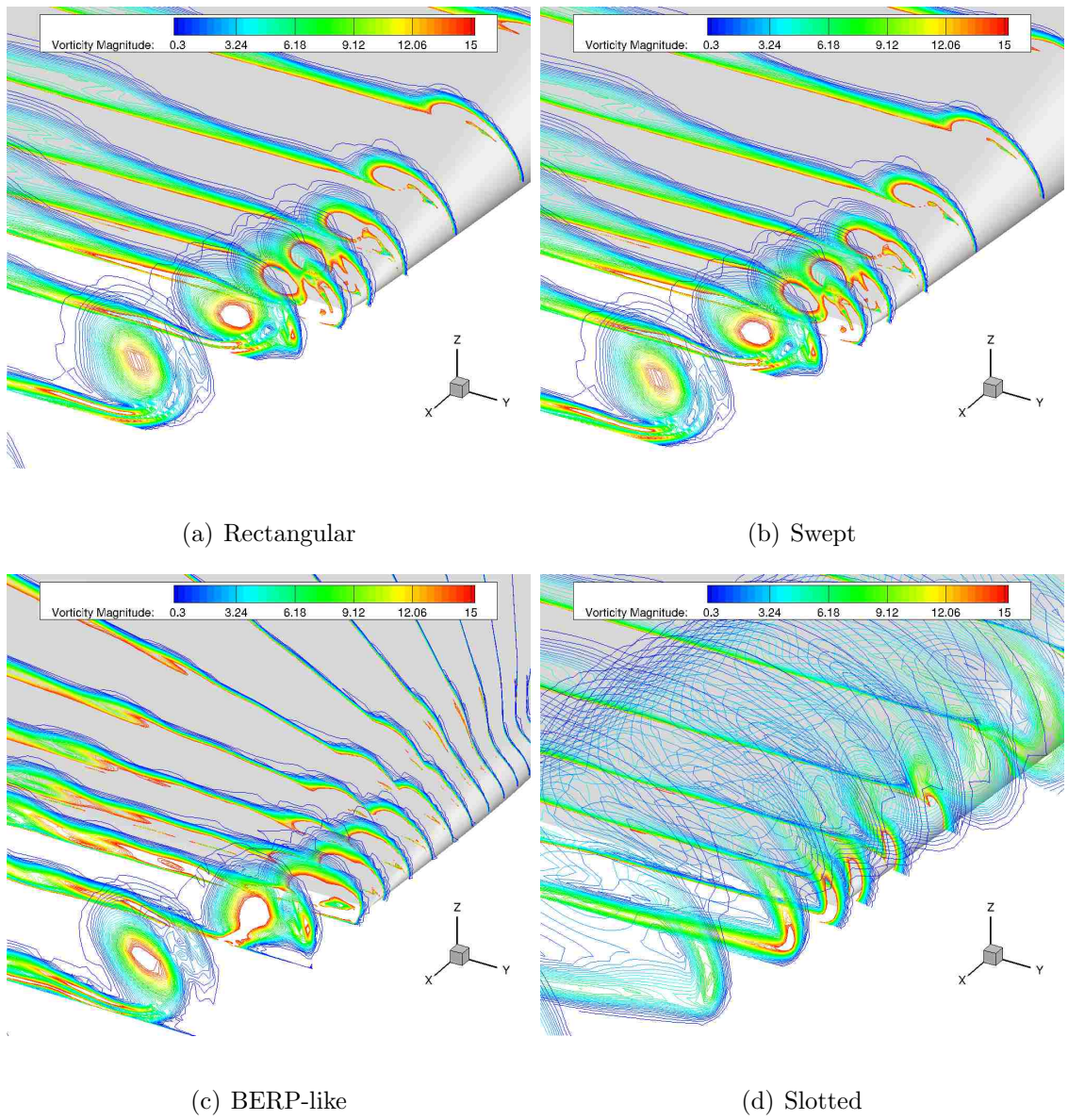
156

(a) Rectangular

(b) Swept

(c) BERP-like

(d) Slotted

Figure 4.14: Near wake flow field visualization using vorticiy magnitude for the 1-bladed sub-scale rotor using different tip shapes.

(a) Rectangular
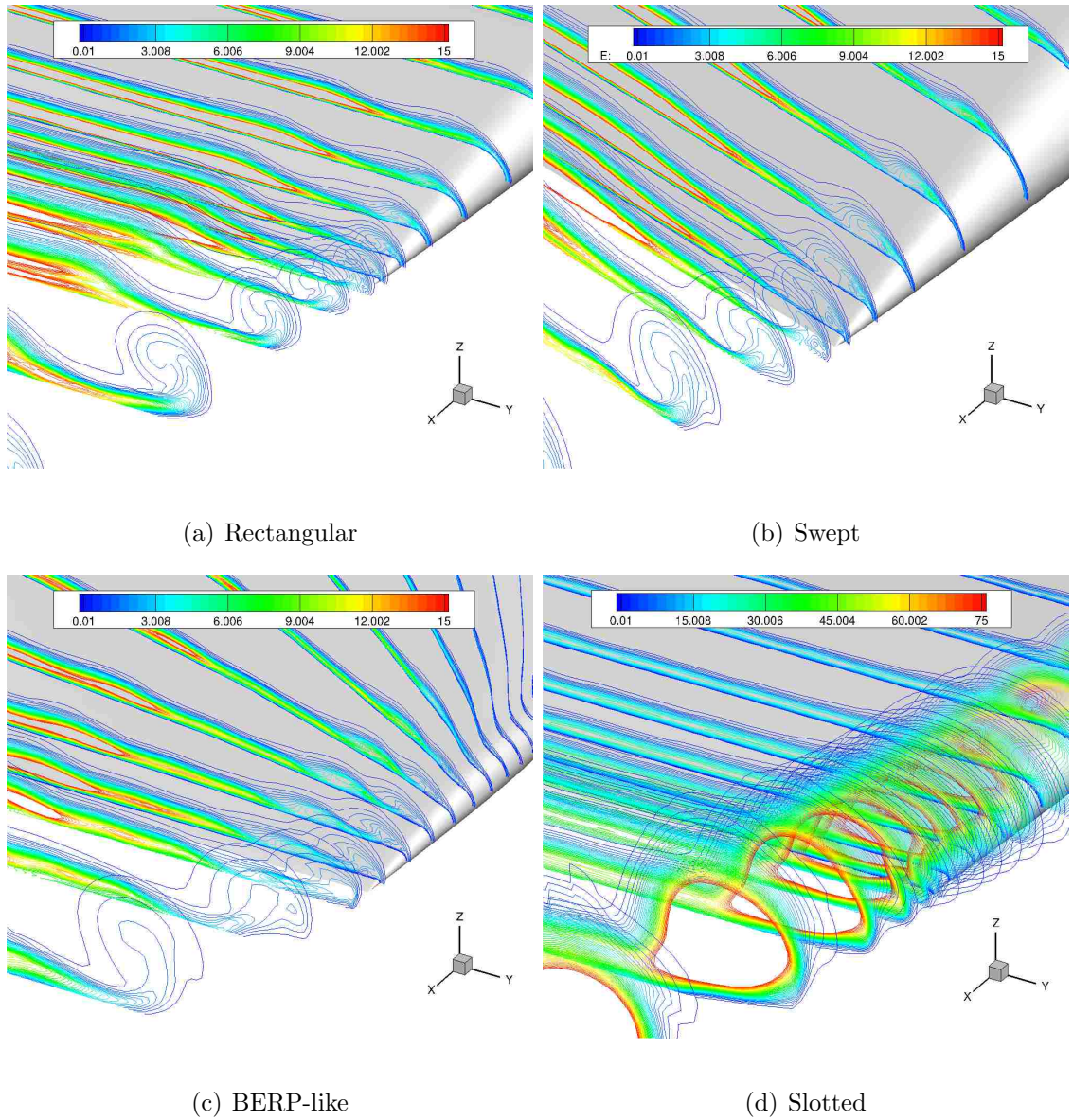
(b) Swept

(c) BERP-like

(d) Slotted

Figure 4.15: Near wake flow field visualization using eddy viscosity contours for the 1-bladed sub-scale rotor using different tip shapes. (Note the difference in levels for slotted tip).

tip seen in fig. 4.14(d) produces a highly diffused vortex core, which occurs because of the turbulence produced by the internal slots at the tips of the blade and the subsequent turbulent mixing produced in the otherwise close to laminar tip vortex. The levels of turbulence are visualized by looking at the computed eddy viscosity levels for all tip shapes in figure 4.15. The eddy viscosity levels for the rectangular, swept and BERP-like tip shape simulations are of similar magnitude. However, the turbulence levels for the slotted tip shape are five times that from the other tip shapes resulting in a large amount of diffusion. A detailed understanding of the flow physics inside the slots is studied in the following section.

4.10   Flow Through the Slots

The flow physics through the slots is analyzed by extracting quantities from the middle plane through each of the slots. Figure 4.16(a) shows the contours of velocity magnitude through all the slots along with velocity vectors. The velocity magnitude at the exit for slots a, c and d are equal or above 0.24. This value is representative of the incoming flow velocity because the velocity is non-dimensionalized by the speed of speed inside OVERTURNS solver. The high velocity magnitude aids in injecting momentum into the flow field. Note that a large recirculation zone exists for the outermost slot (labeled as slot A) in fig. 4.16(a). This recirculation zone decreases as the slot length increases as one goes from the outermost, slot A, to the innermost, slot D. For slot A, the flow needs to turn much more sharply and hence there is a large recirculation zone as compared to slot D. Figure 4.16(b) shows the amount of
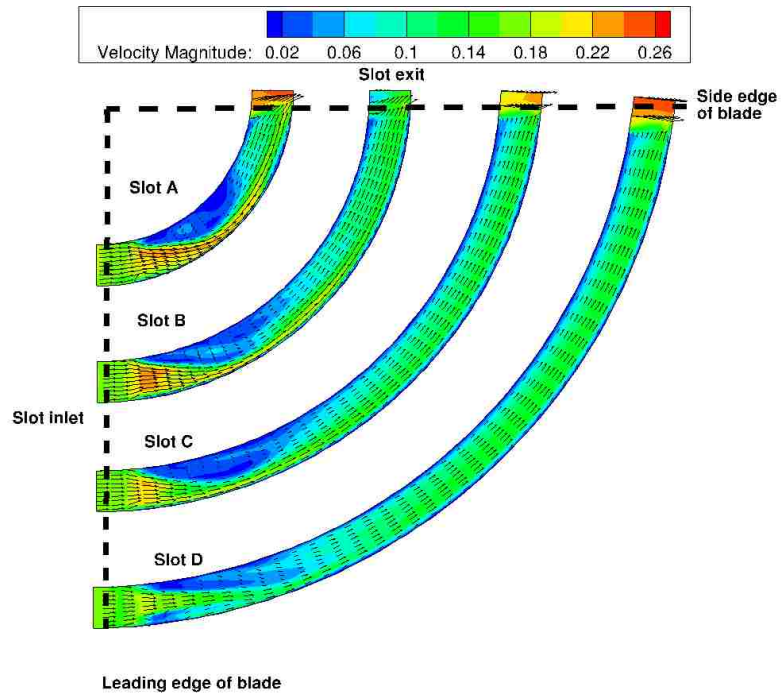
(a) Velocity magnitude
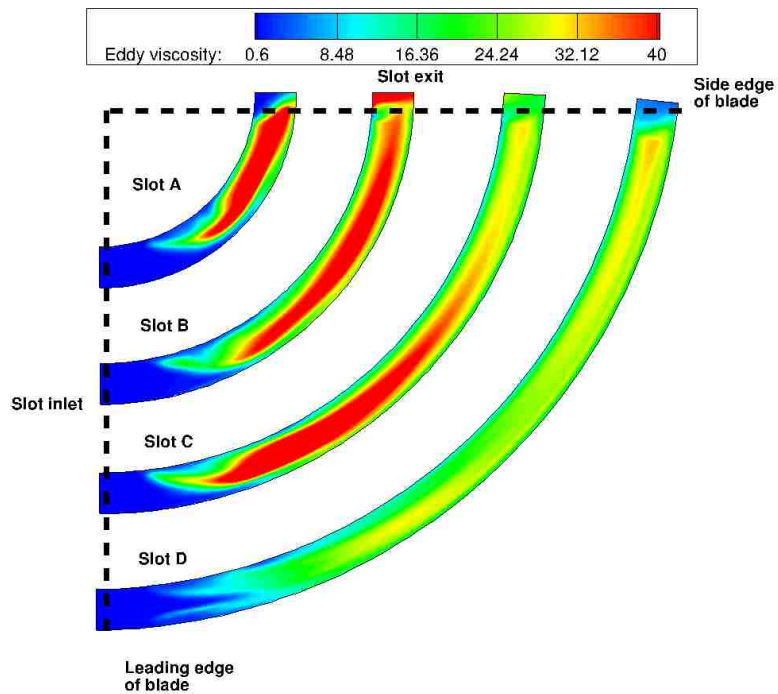
(b) Eddy viscosity level

Figure 4.16: CFD predicted flow field through the slots of the slotted tip case.

turbulence indicated by the eddy viscosity levels. It can be seen that the turbulence levels increase by almost six times from the inlet to the exit. This turbulence mixing causes the diffusion of the otherwise close to laminar tip vortex.
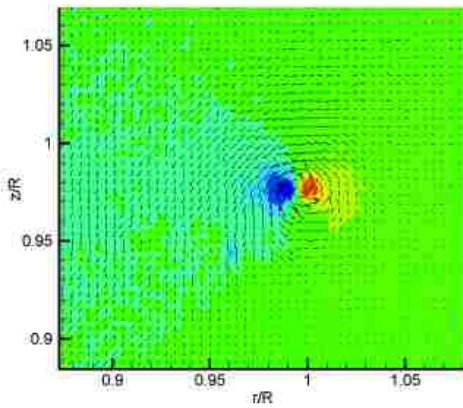
4.11   Vertical Velocity Comparison

A qualitative comparison between the CFD and experiments can be further studied by observing the instantaneous vertical velocity contours at 30^0 wake age for the four different tip shapes in Figures 4.17 and 4.18 The tip vortex in the computations is observed to be located slightly higher (z/R) and slightly more radially outward (r/R) compared to in the experiments for all the tip shapes. Overall, the vertical velocity magnitude is in good agreement between the computations and the experiments for both rectangular and swept tip shapes (fig. 4.17). However, the vertical velocity magnitude for the BERP-like tip in fig. 4.18 is seen to haves slightly lower values in CFD than in experiments. The lower vertical velocity values can be a result of the lower thrust prediction in the CFD results for the BERP-like tip that causes a lower tip vortex strength, leading to a decrease in the vertical velocity values. The slotted tip in fig. 4.18 is seen to have diffused the vortex core in both CFD and experiments, but the diffusion is observed to be higher in experiments than in CFD.
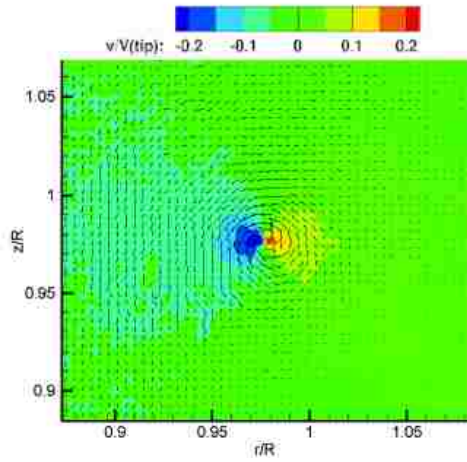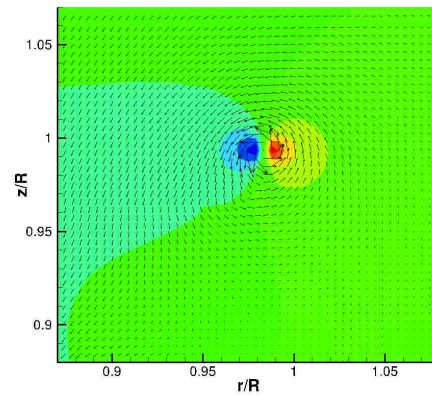
(a) Rectangular, Experimental
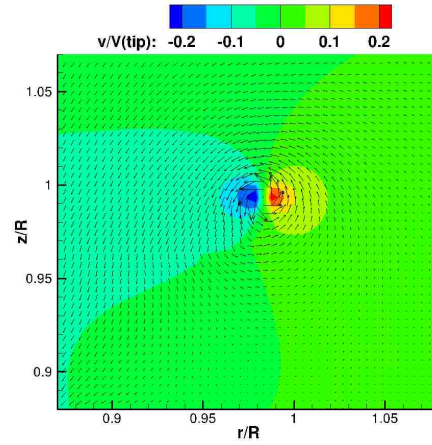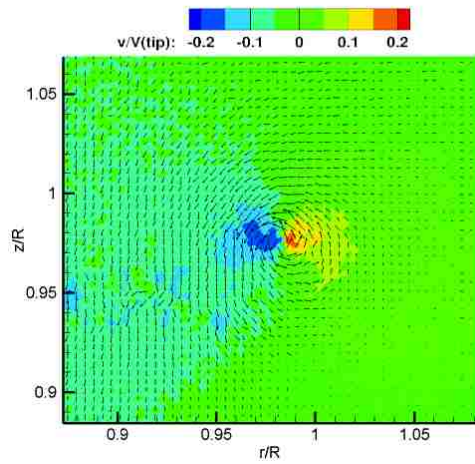
(b) Rectangular, Computational
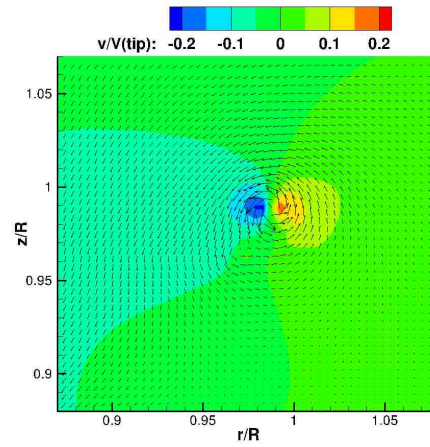
(c) Swept, Experimental

(d) Swept, Computational

Figure 4.17: Vertical velocity contours at a 30^0 azimuthal plane for different tip shapes of 1-bladed sub-scale rotor.

(a) BERP-like, Experimental

(b) BERP-like, Computational

(c) Slotted, Experimental

(d) Slotted, Computational

Figure 4.18: Vertical velocity contours at a 30^0 azimuthal plane for different tip shapes of 1-bladed sub-scale rotor.

(a) Rectangular, Experimental

(b) Rectangular, Computational

(c) Swept, Experimental

(d) Swept, Computational

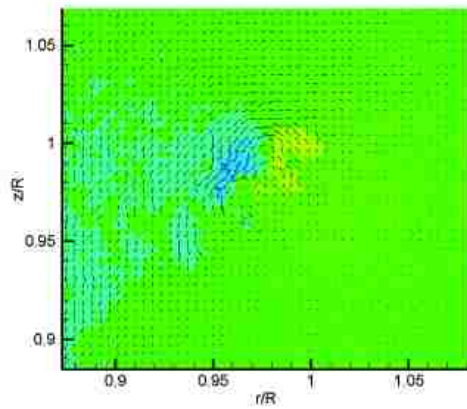Figure 4.19: Total velocity contours at a 30^0 azimuthal plane for different tip shapes of 1-bladed sub-scale rotor.
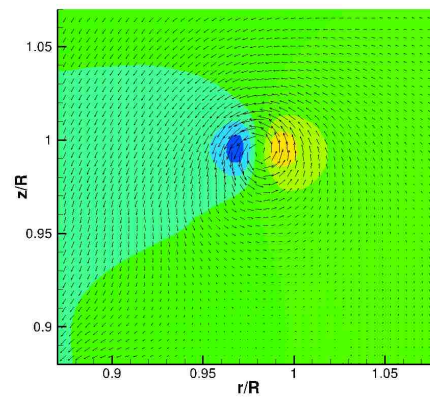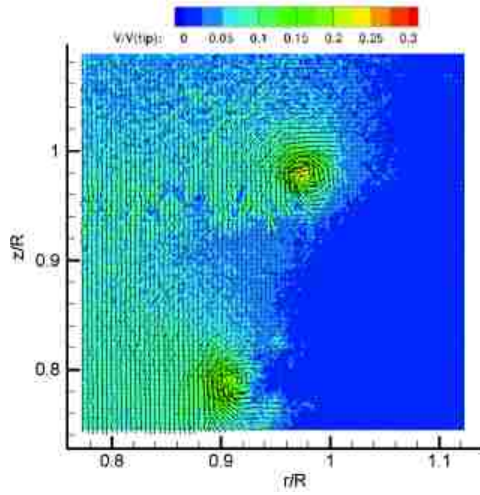
(a) BERP-like, Experimental
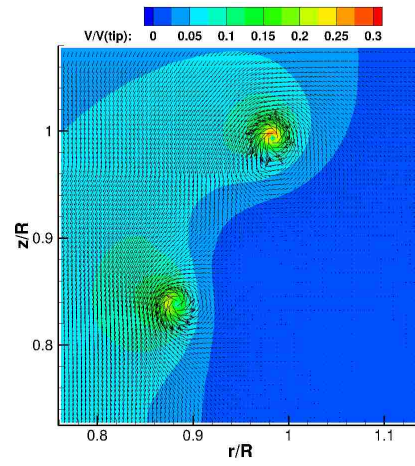
(b) BERP-like, Computational

(c) Slotted, Experimental

(d) Slotted, Computational

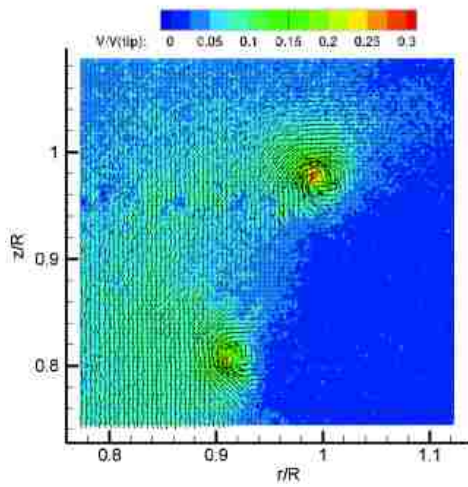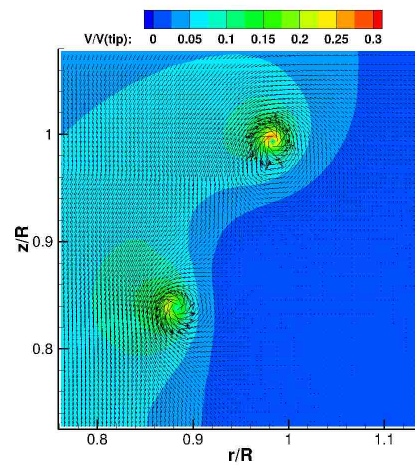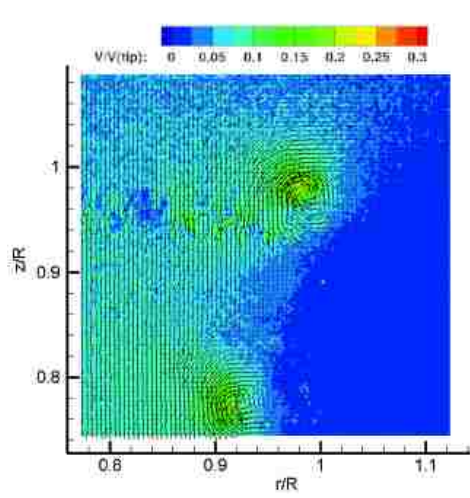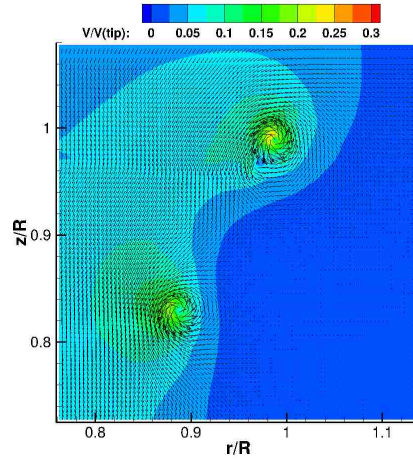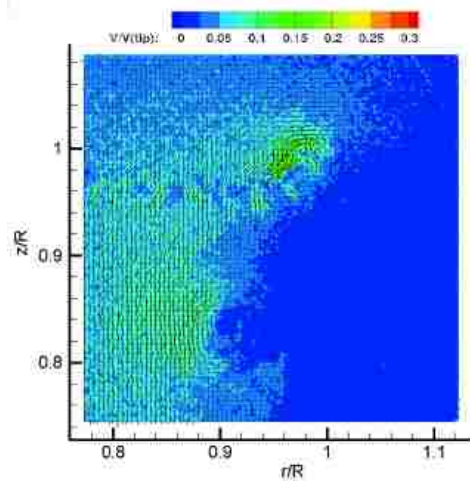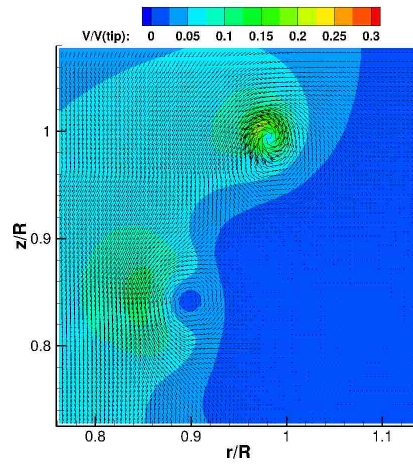Figure 4.20: Total velocity contours at a 30^0 azimuthal plane for different tip shapes of 1-bladed sub-scale rotor.

4.12   Total Velocity Magnitude Comparison

Following the qualitative comparison of vertical velocity magnitudes, a qualitative comparison between the CFD results and the experimental measurements is further made by comparing the total velocity contours for the four tip shapes in Figures 4.19 and 4.20. The plots show the tip vortices located at 30^0 and 390^0 wake age, respectively. The difference in the location of the tip vortices between CFD and experiments is observed to have increased from 30^0 to 390^0 wake age. For the rectangular tip, the CFD predicted tip vortex at 390^0 is seen to be located at $(r/R, z/R) = (0.86,0.84)$, whereas the experimental location is at $(r/R, z/R) = (0.92,0.80)$. This implies that the tip vortices in the computations are descending slower and are still contracting under the effect of the rotor wake; whereas in the experiments, the tip vortices have already started to follow a radially expanding path. This observation is seen for the rest of the tip shapes as well. However, the difference between the experimental and computational location of the tip vortices at 390^0 is least for the slotted case and maximum for the BERP-like tip. Overall the sCFD predicted locations for all tip shapes seem to be having a little variation.

4.13   Instantaneous Swirl Velocity

Following the qualitative comparison of results from CFD and experimental measurements, a more quantitative comparison of the rotor wake is done by comparing the instantaneous swirl velocity profiles from the experiments and computations for various wake ages. The instantantaneous swirl velocities are non-dimensionalized
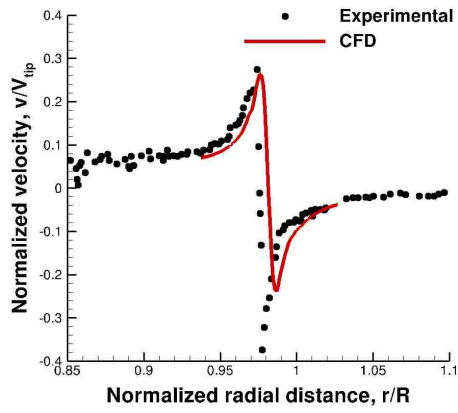
(a) $\zeta = 30°$ (b) $\zeta = 60°$
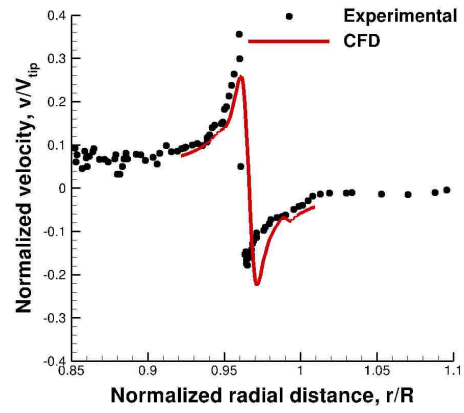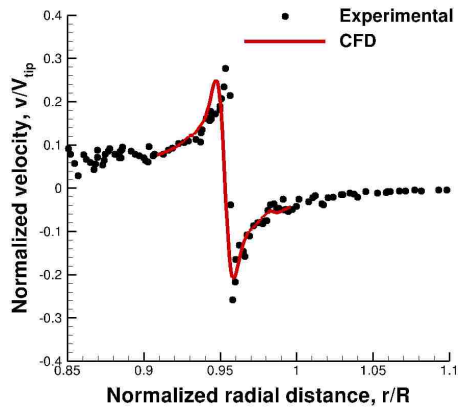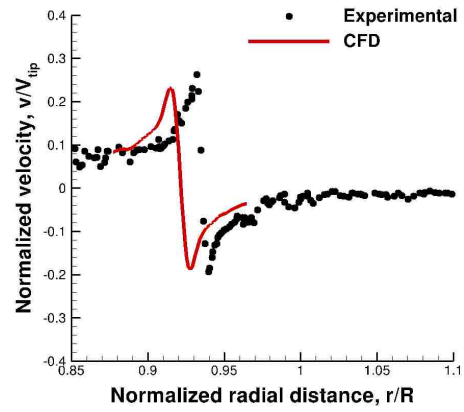
(c) $\zeta = 90°$ (d) $\zeta = 180°$
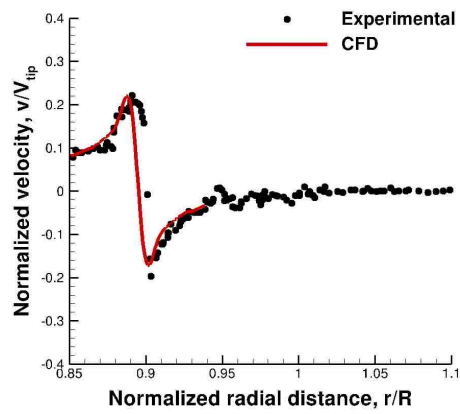
(e) $\zeta = 270°$

Figure 4.21: Instantaneous swirl velocity profile for rectangular tip at different wake

ages.   167

(a) $\zeta = 30°$

(b) $\zeta = 60°$

(c) $\zeta = 90°$
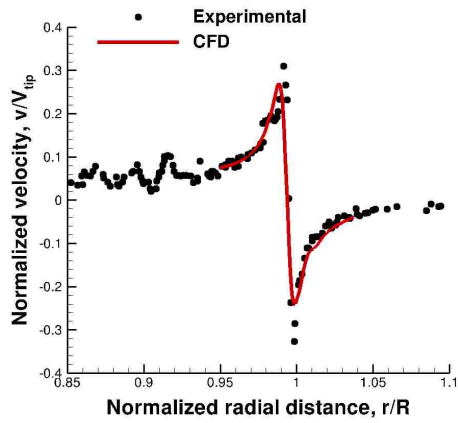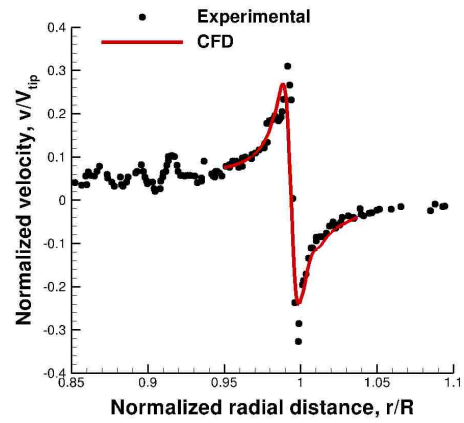
(d) $\zeta = 180°$

(e) $\zeta = 270°$

Figure 4.22: Instantaneous swirl velocity profile for swept tip at different wake ages.

(a) $\zeta = 30°$

(b) $\zeta = 60°$

(c) $\zeta = 90°$
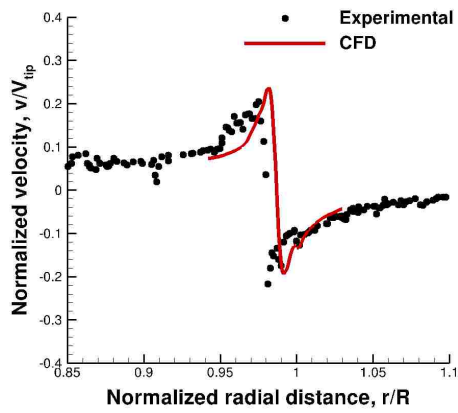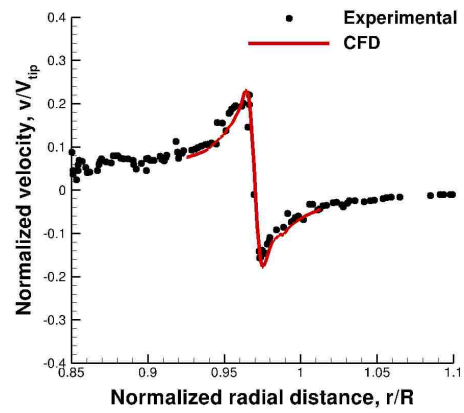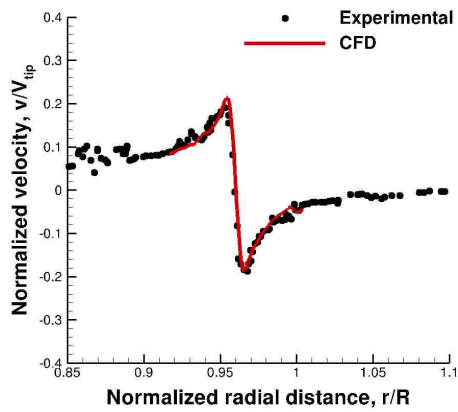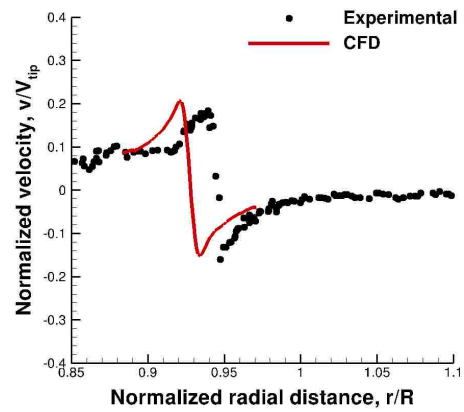
(d) $\zeta = 180°$
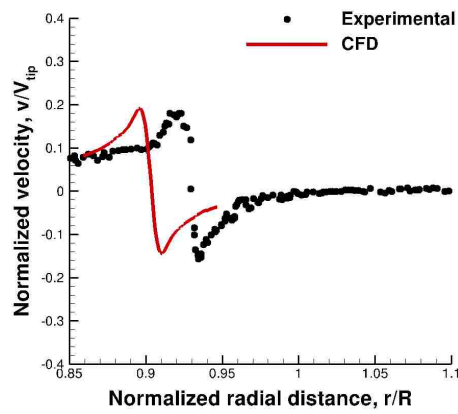
(e) $\zeta = 270°$

Figure 4.23: Instantaneous swirl velocity profile for BERP-like tip at different wake

ages.

169
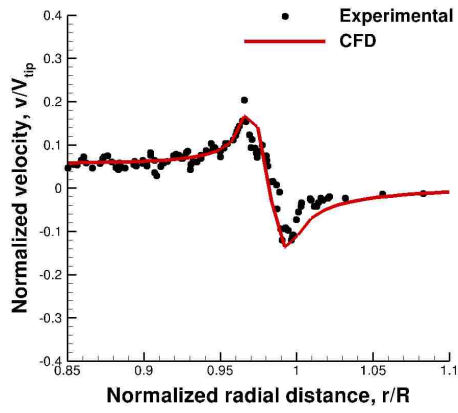
(a) $\zeta = 30°$ (b) $\zeta = 60°$
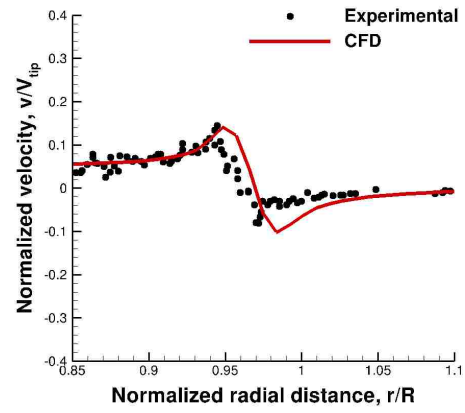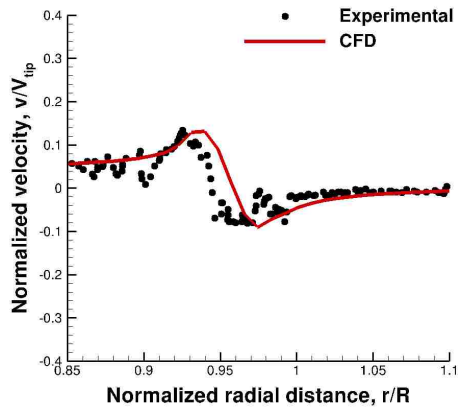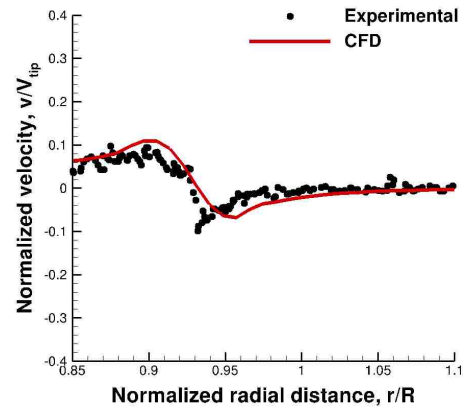
(c) $\zeta = 90°$ (d) $\zeta = 180°$
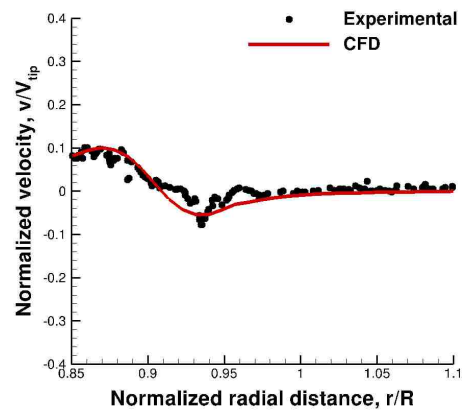
(e) $\zeta = 270°$

Figure 4.24: Instantaneous swirl velocity profile for slotted tip at different wake ages.

by the freestream tip Mach number. Figures 4.21–4.24 show the profiles for the rectangular, swept, BERP-like and slotted tips, respectively. The rectangular and swept tip shape computations show an under prediction of peak to peak swirl velocity as compared to the experimental results for all wake ages. The position of the wake is predicted well in the computations for wake ages of $\zeta = 30°$, $60°$ and $90°$. However, the position of the predicted wake for $\zeta = 180°$ and $270°$ shows an additional amount of contraction in the computations reflected by the shift of the curves to the left of the experimental values. It can be observed that the vortices move inwards as they age and reach $0.9R$ at $\zeta = 270°$. This also marks the slipstream boundary of the rotor wake path. The results are in agreement with the observations drawn by looking at the flow field using the velocity magnitudes, where the computations were showing a contracted position of the rotor wake but the experiments showed a radially outboard location of the tip vortices.

Note that the CFD predicted values for BERP-like tip (seen in figure 4.23) show good comparison of peak to peak swirl velocity with experiments for all wake ages. Similar to the rectangular and swept tip, the BERP-like tip shows an excellent agreement of wake position for all wake ages ranging from $\zeta = 30°$ to $270°$. The slotted tip results, in figure 4.24, show an excellent agreement for the peak to peak magnitude of swirl velocity along with the positon of the rotor wake.
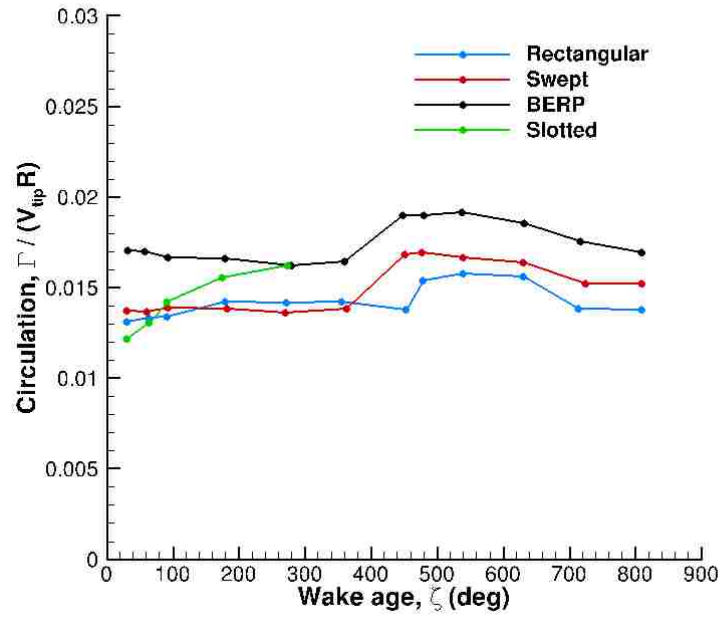
(a) Experimental, circulation
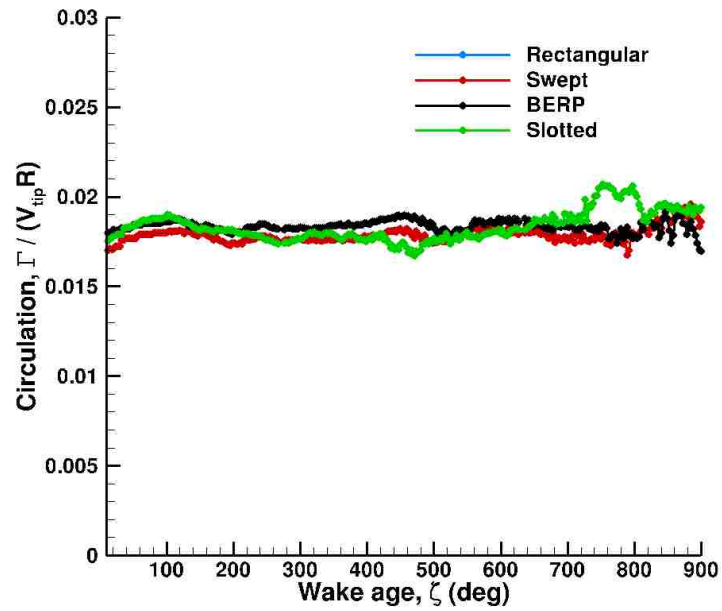
(b) Computational, circulation

Figure 4.25: Comparison of CFD (SA-DDES) predicted circulation as a function of wake age for different tip shapes.
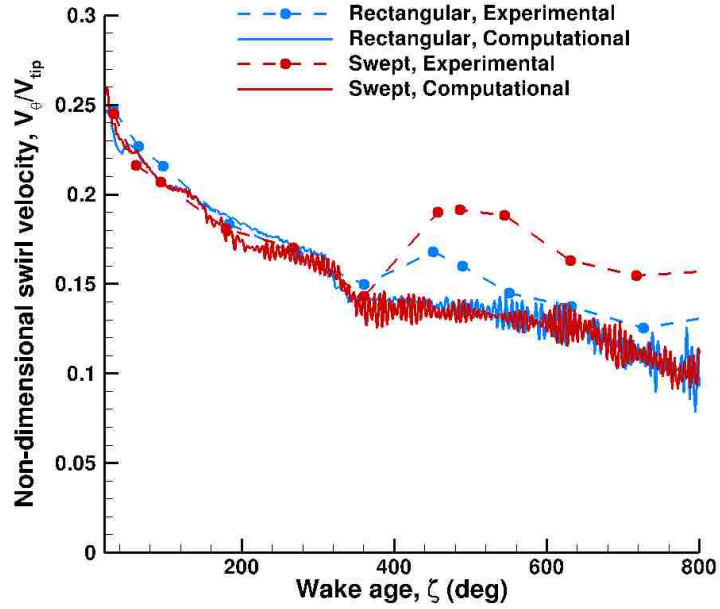
(a) Non-dimensional peak swirl velocity
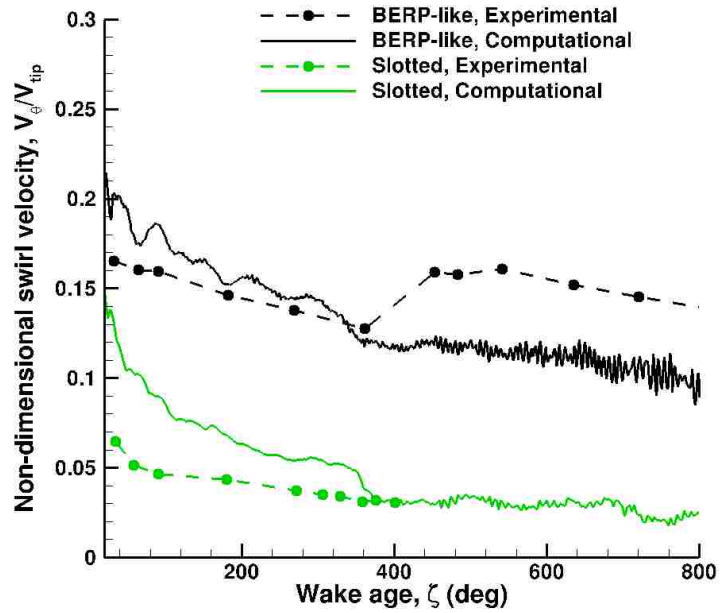
(b) Non-dimensional peak swirl velocity

Figure 4.26: Comparison of CFD (SA-DDES) predicted peak swirl velocity as a function of wake age for different tip shapes.
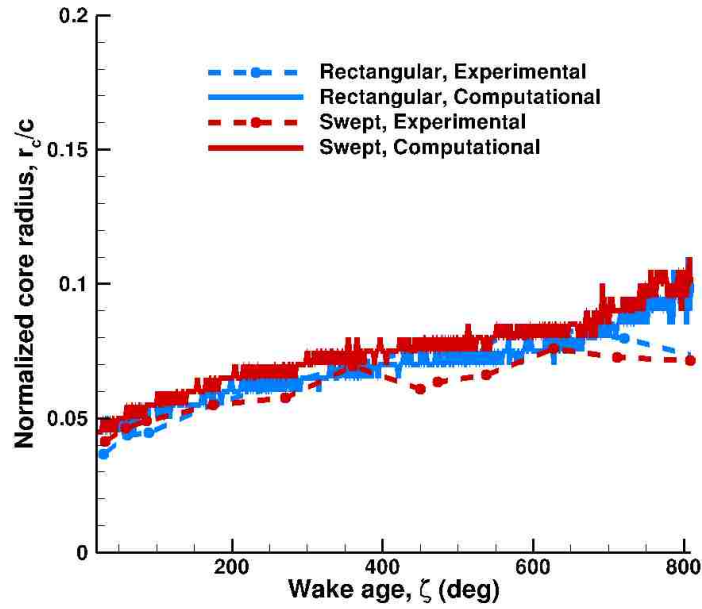
(a) Normalized core radius comparison
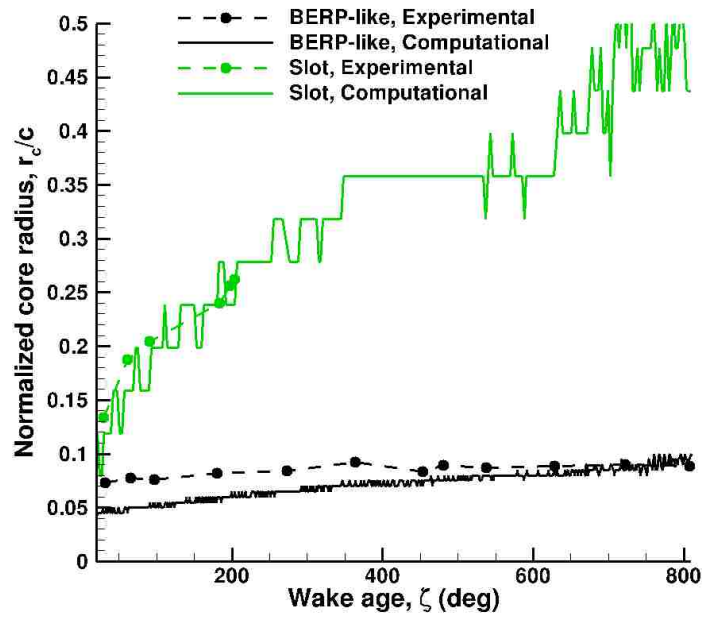
(b) Normalized core radius comparison

Figure 4.27: Comparison of CFD (SA-DDES) predicted peak swirl velocity as a function of wake age for different tip shapes.

4.14 Revised tip vortex charactersitics with SA-DDES methodology

Tip vortex characteristics can be studied in detail by looking at the circulation, peak swirl velocity and core radius growth with wake age. Figure. 4.25 shows the variation of circulation values with wake age for both experiments and computations, respectively. Circulation is non-dimensionalized by the tip speed and rotor radius. The experimental results in fig. 4.25(a) show a slightly higher value of the circulation for the BERP-like blade compared to the rectangular and swept tip shape. However, in the SA-DDES computations in fig. 4.25(b), the circulation levels remain fairly constant with wake age for the rectangular, swept, BERP-like blade and slotted tip. This is expected because the total amount of thrust predicted in the computations is similar for the three tip shapes (rectangular, swept and slotted) whereas the experiments predict a slightly higher thrust value for the BERP-like blade. Contrary to the experiments, where the circulation values are not available beyond 270° wake age, the SA-DDES computed circulation values are obtainable over the entire 800° wake age. This is possible; because, while the vortices get highly diffused as the wake age increases they still retain some level of coherence, making it possible for the computations to detect its presence.

Figure 4.26 shows the comparison between the experiments and computations for the variation of peak swirl velocity with wake age. The peak swirl velocity is non-dimensionalized by the tip speed of the rotor blade. Both the computations and experiments show a good agreement for the decreasing peak swirl velocity with wake age until 360° wake age. After 360° wake age, the effect of the ground leads

to a slight increase in peak swirl velocity in the experiments; whereas, it continues to drop in the computations. Overall, the CFD predicted peak swirl velocity profile is noticed to be similar for the rectangular and swept tip shapes. The BERP-like tip computations start at a higher peak value than experiments. Similar to results from the rectanguar and swept tip shapes, the peak swirl velocity profiles for the BERP-like tip keep decreasing with increasing wake age in CFD. The slotted tip case shows a higher peak swirl velocity in the computations but eventually decays and matches the experimental values at 400° wake age. Overall it can be noticed that the SA-DDES methodology is able to predict a reasonable peak swirl velocity comparison between the CFD and experiments; especially as compared to the RANS results shows earlier.

Figure 4.27 shows the variation of vortex core radius as a function of wake ages for the four different tip shapes. The core radius is non-dimensionalized by the rotor blade chord. The core radius growth for the rectangular and swept tip computations agrees well for all wake ages with experimental results. The initial core radius for the BERP-like tip seems to be higher in the experiments than in the computations, but starts to compare well with experiments beyond 750°. The growth of the core radius for the slotted tip is seen to be measured only up until a wake age of 200°; however, CFD can still track the core radius for the entire range of wake age and the core radius is seen to double at $\zeta = 800°$ from its value obtained at 200°.

4.15 Instantaneous Radial Velocity Close to the Ground

A quantitative comparison of the experiments and computations close to the ground is made by plotting the instantaneous radial velocity profiles. Figures 4.28, –4.31 show the radial velocity profiles for the rectangular, swept, BERP-like and slotted tip shapes, respectively. The results are compared at five radial locations ($r/R = 1.25$, $r/R = 1.40$, $r/R = 1.53$ and $r/R = 1.60$) at a wake age of $0°$. It can be seen that the magnitude of the experimental and computational radial velocity profiles are in good agreement at all radial locations. The experiments show fluctuations in the radial velocity profiles for the three tip shapes - rectangular, swept and BERP-like tip shape at all radial locations. The fluctuations correspond to the presence of the tip vortex in the flow field. These fluctuations are under predicted in the computations at all locations. For the slotted tip, both the experimental measurements and computation results show a good agreement, as observed in figure 4.31. The radial velocity profiles show considerably lower fluctation, indicating the fact that the tip vortices are diffused by the time they get close to the ground plane in both the experiments and the computations. The lack of radial velocity fluctuations for the slotted tip can be an important factor to mitigate the uplift of sediment particles during brownout phenomenon.

4.16 Vertical Velocity Magnitude Comparison Close to the Ground

Figures 4.32 and 4.33 compare the instantaneous vertical velocity magnitude contours close to the ground for all tip shapes. CFD data shown in these figures
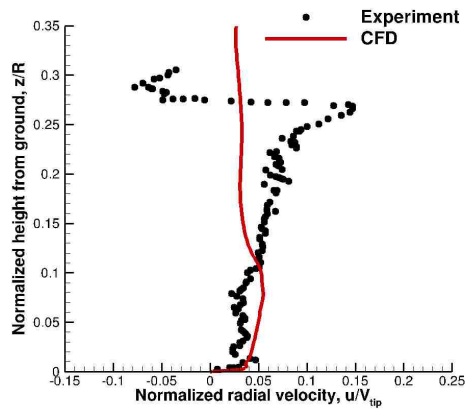
(a) $r/R = 1.16$
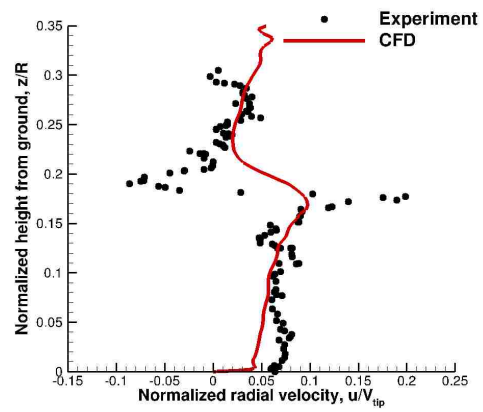
(b) $r/R = 1.29$
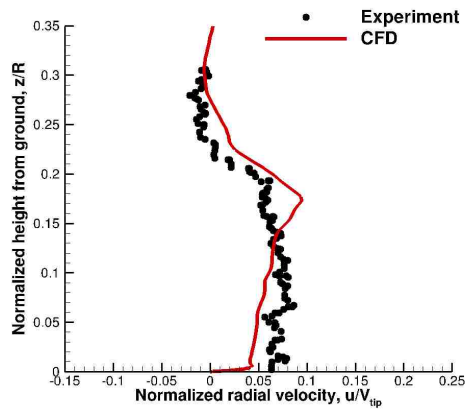
(c) $r/R = 1.40$
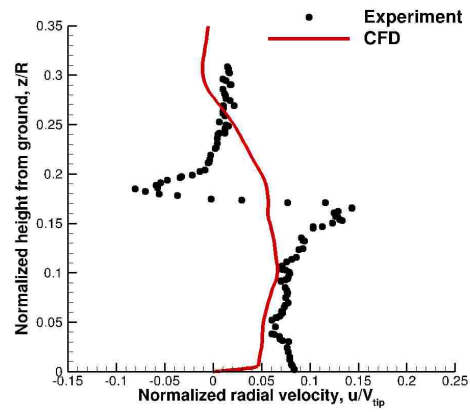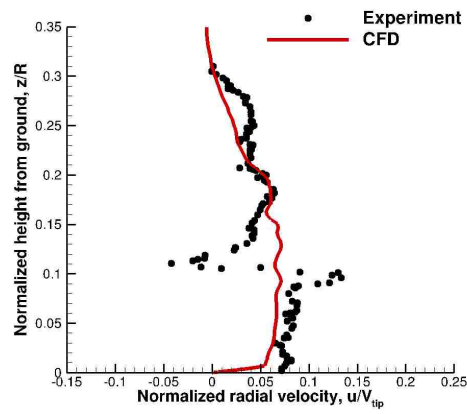
(d) $r/R = 1.53$

(e) $r/R = 1.60$

Figure 4.28: Instantaneous radial velocity profile comparison for rectangular tip at $\zeta = 0°$.

178
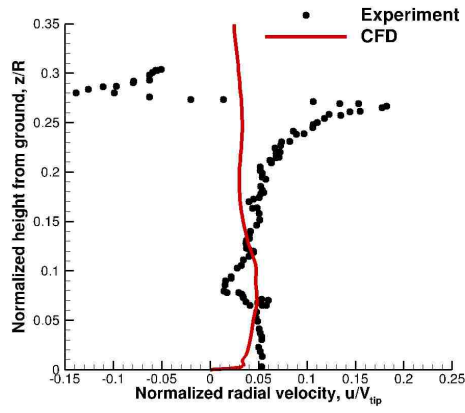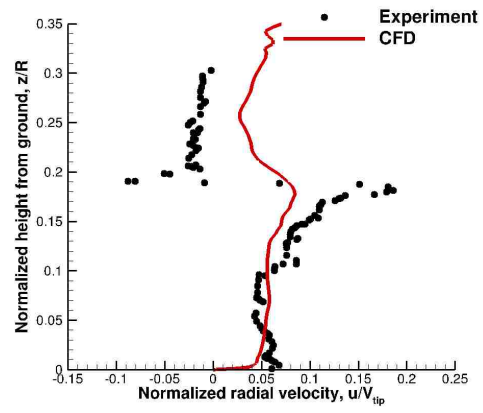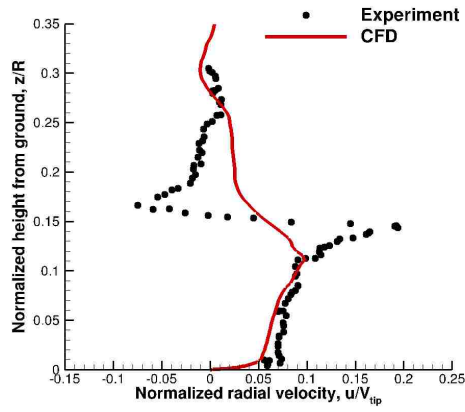
(a) $r/R = 1.16$
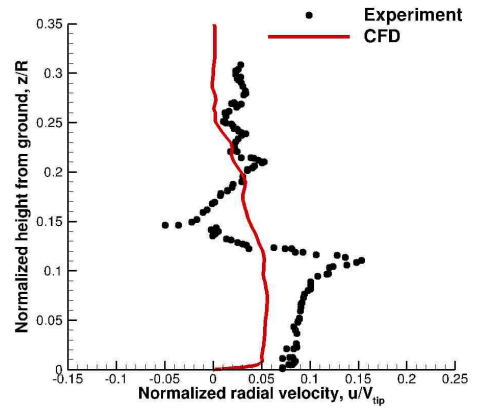
(b) $r/R = 1.29$
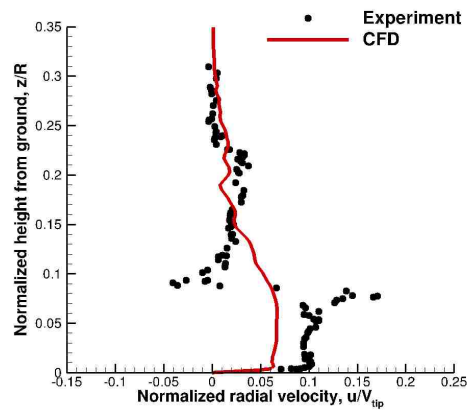
(c) $r/R = 1.40$

(d) $r/R = 1.53$

(e) $r/R = 1.60$

Figure 4.29: Instantaneous radial velocity profile comparison for swept tip at $\zeta = 0°$.
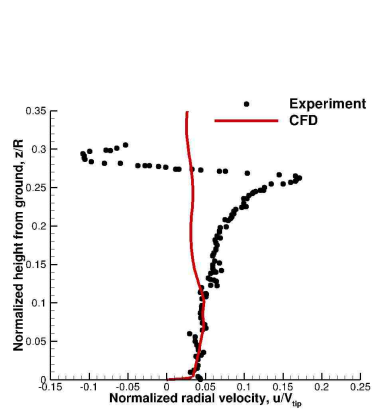
(a) $r/R = 1.16$
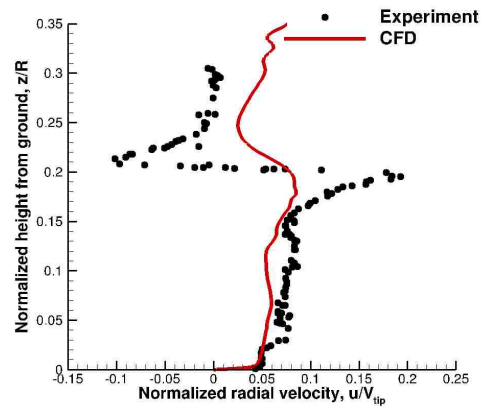
(b) $r/R = 1.29$
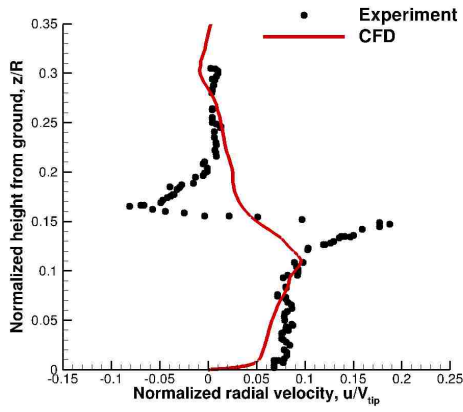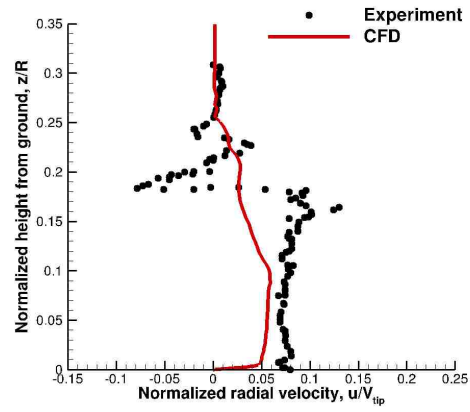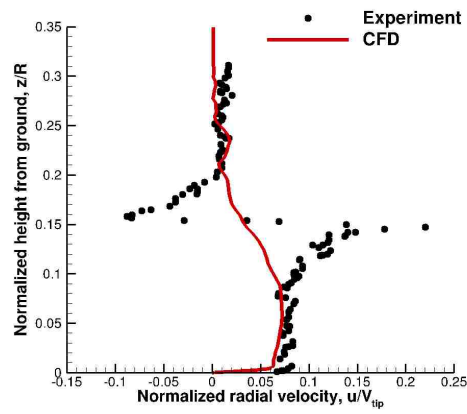
(c) $r/R = 1.40$

(d) $r/R = 1.53$

(e) $r/R = 1.60$

Figure 4.30: Instantaneous radial velocity profile comparison for BERP-like tip at

$\zeta = 0°$.
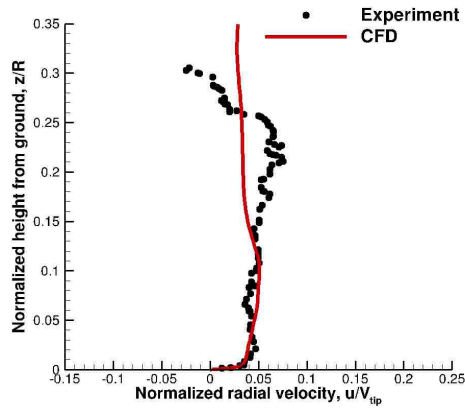
(a) $r/R = 1.16$
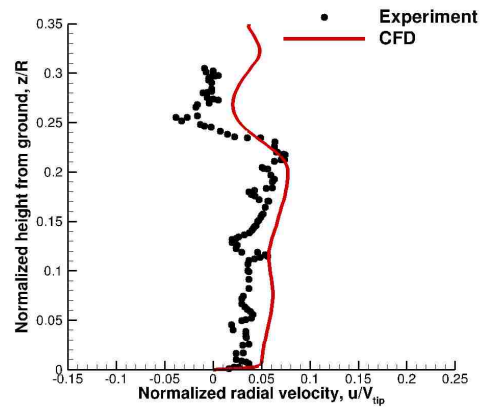
(b) $r/R = 1.29$
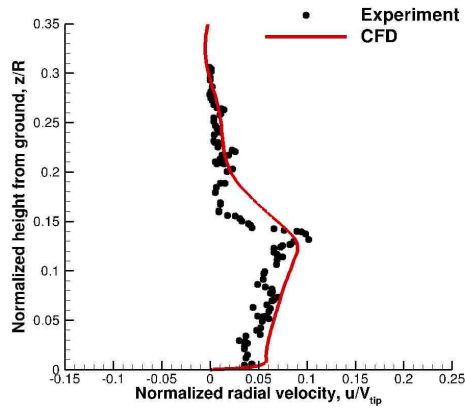
(c) $r/R = 1.40$
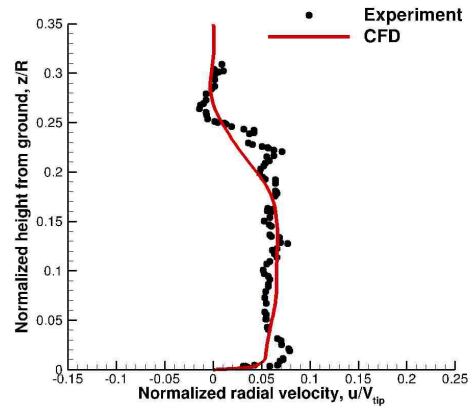
(d) $r/R = 1.53$
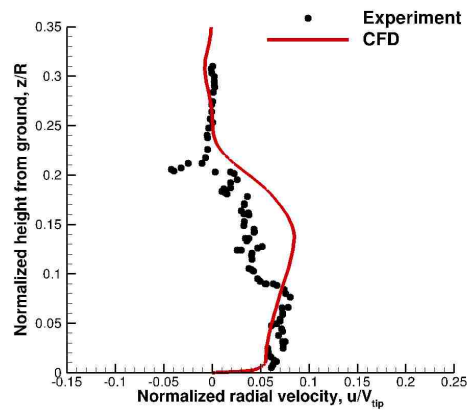
(e) $r/R = 1.60$

Figure 4.31: Instantaneous radial velocity profile comparison for slotted tip at $\zeta = 0°$.
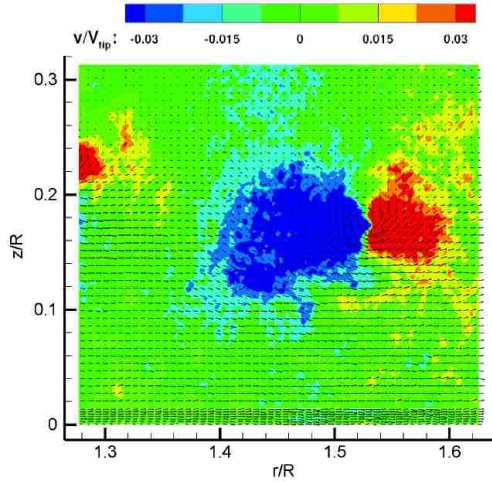
(a) Rectangular, Experimental
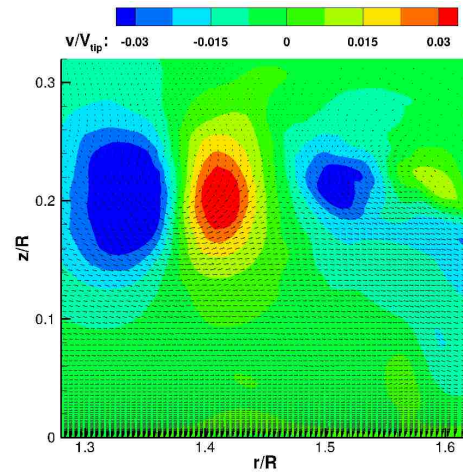
(b) Rectangular, Computational
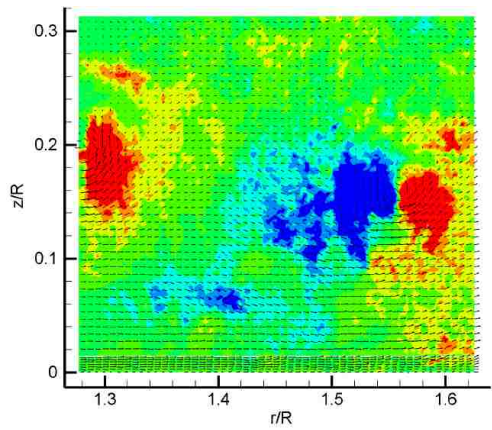
(c) Swept, Experimental
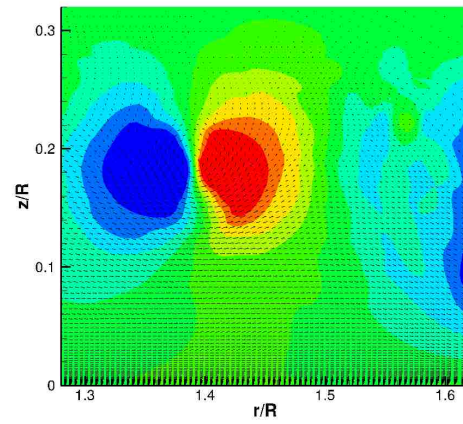
(d) Swept, Computational

Figure 4.32: Comparison of instantaneous vertical velocity close to the ground. (Note: CFD predicted data is extracted from $\zeta = 30°$ while experimental data is extracted from images that showed spatially correlated vortex positions).
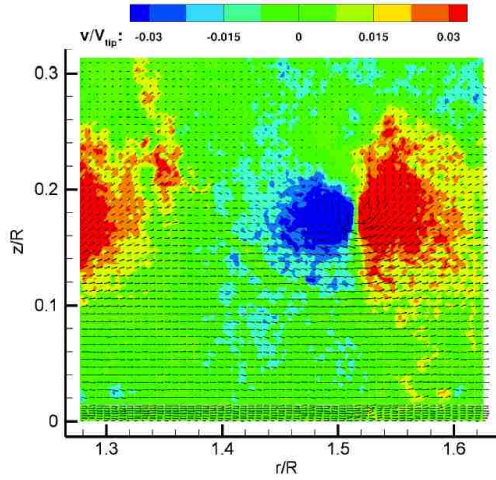
(a) BERP-like, Experimental   (b) BERP-like, Computational
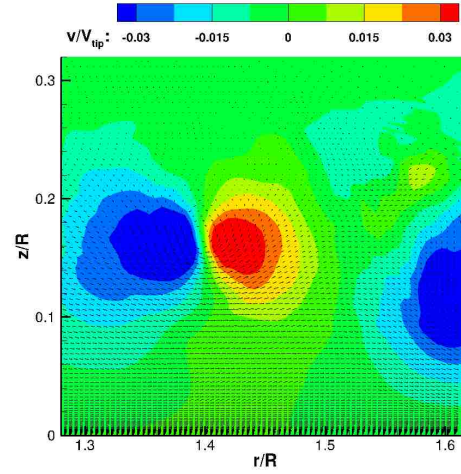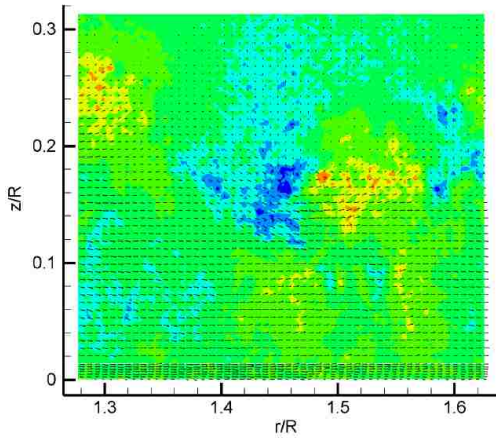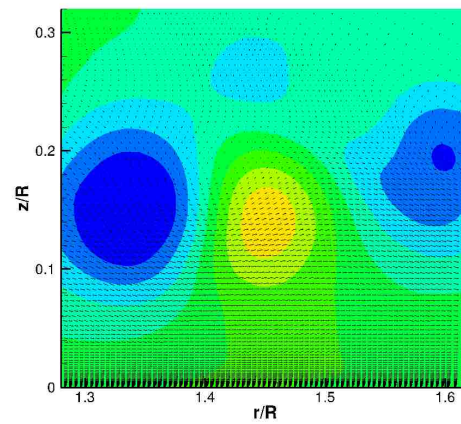
(c) Slotted, Experimental   (d) Slotted, Computational

Figure 4.33: Comparison of instantaneous vertical velocity close to the ground. (Note: CFD predicted data is extracted from $\zeta = 30°$ while experimental data is extracted from images that showed spatially correlated vortex positions).

183

corresponds to $\zeta = 30°$ wake age. Since the experiments observe a highly aperiodic flow close to the ground, the PIV data is obtained such that vortex positions correlate between different rotor tip shapes. This implies that the vortex positions between CFD and experiments cannot be compared. However, an estimate can be made about the nature of tip vortices close to the ground between different tip shapes. The red contours correspond to the vertical upwash velocity and blue contours show the downwash velocity. The experiments show highest upwash for the BERP-like tip and this pattern is also observed in computations. Note that BERP-like tip showed a reduced vortex strength at early wake ages when compared to rectangular and swept tips in both computations and experiments, however at older wake ages closer to the ground the flow field for BERP-like tip was is showing very similar strength to the ones obtained from rectangular and BERP-like tip. The slotted tip is seen to generate lowest upwash velocity close to the ground in both experiments and CFD. The lower upwash velocities from slotted tips seen signify that slotted tip can be a possible candidate for brownout mitigation.

4.17   Instantaneous Pressure Variation at Ground Plane

The unsteady pressure variation at the ground plane can be a contributing factor for the sediment mobilization as discussed earlier. Figure 3.29 shows the pressure coefficient variation at the ground plane for the four different tip shapes. The flow field is extracted in computations from an instantaneous solution. The circular region extending from $x/R = -1.0$ and $x/R = 1.0$ of red contour values

184

(a) Rectangular

(b) Swept

(c) BERP-like

(d) Slotted
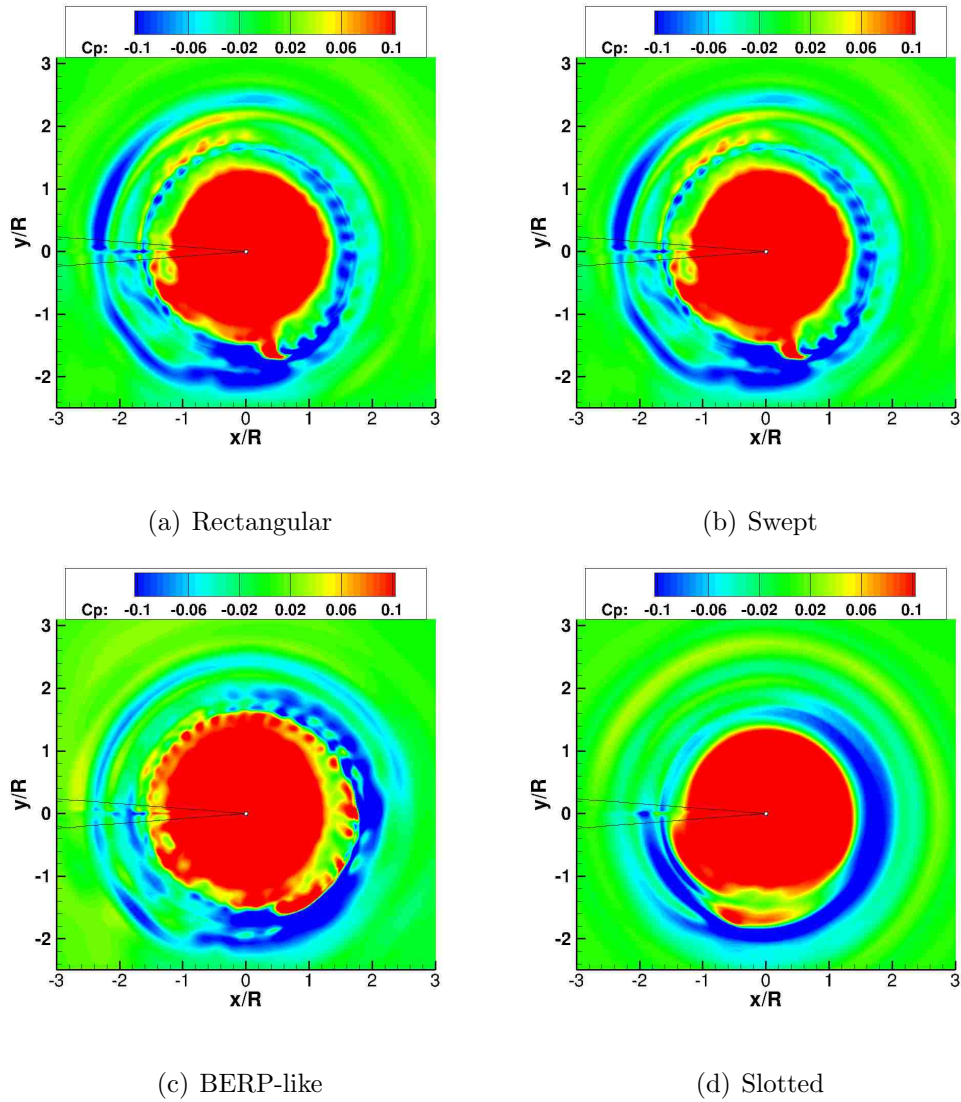
Figure 4.34: CFD predicted pressure coefficient by the 1-bladed sub-scale rotor blade for different tip shapes.

185

shows the high pressure in the inboard regions. Beyond that, lower pressure (shown in blue) contour levels is observed because of the presence of the tip vortex that tends to induce a lower pressure region as it passes over the ground plane. Notice the striations/flucutations in the pressure values for the rectangular tip which are not present in the slotted tip. The lack of fluctuations for the slotted tip flow field at the ground plane can possibly limit sediment mobilization during brownout.

4.18   Summary of Chapter

In this chapter, OVERTURNS was used to simulate a hovering 1-bladed sub-scale rotor operating at a tip Mach number of 0.24 and a tip Reynolds number of $250,000$ in ground effect with the primary objective of showing the effect of four different tip shapes on the resulting rotor wake. The four different tip shapes modeled were: rectangular, swept, BERP-like and slotted. The mesh system required novel strategies to efficiently capture the rotor with available computational resources. Use of the S–A turbulence model led to an overprediction of turbulence levels and a modification to the SA-DDES methodology was employed to accurately predict the turbulence levels. The computations were then compared with experimentally measured thrust. This was followed by a flow field comparison at early wake ages with the experimental particle-image-velocimetry data. The tip vortex characteristics (circulation, peak swirl velocity and core radius) were also compared for first $800°$ wake age. Analysis of the near wake flow field showed a high amount of diffusion in the tip vortices emanating from the slotted tip as compared to the other tip

shapes. Consequently, close to the ground minimal pressure variations occurred for the case of the slotted tip shape, indicating the absence of the effect of tip vortices. This showed that the slotted tip can be a good candidate for mitigating the effects of brownout phenomenon.

Chapter 5

Conclusions

This chapter summarizes the motivation of this work, key results and observations and provides recommendations for future work.

5.1   Summary

The overall objective of this dissertation was to validate a high fidelity computational methodology to study rotor wakes and their interaction with a ground plane. An accurate capturing of rotor wake and its affect on the ground plane gives a fundamental understanding of the flow physics that causes the brownout phenomenon. The 3-D MPI parallel, compressible Reynolds-Averaged Navier Stokes OVERTURNS solver was used for simulating the flow physics.

The computations were performed to model both a hovering micro-scale rotor as well as sub-scale rotors operating in ground effect (IGE). These two different scales of rotors operated in two different set of flow conditions with the sub-scale rotor having a higher tip Mach number and Reynolds number. The hovering micro-scale rotor was operated at three different rotor heights above ground. The sub-scale rotor was operated at one particular rotor height but with four different tip shapes. The computations were rigorously validated with experimentally measured performance data, wake trajectory, radial velocity profiles at the ground and with

tip vortex profile data. The key observations from the study of micro-scale and sub-scale rotor cases is discussed in the following section.

5.2 Key Observations

The key observations and conclusions drawn from the present work are summarized in this section. These conclusions are divided into the computational study of micro-scale and sub-scale rotors.

5.2.1 Micro-scale rotor

Simulations were performed for a 2-bladed hovering micro-scale operating IGE. The aspect ratio of the rotor blade was 4.387 and the rotors operated at a tip Mach number of 0.8 and a tip Reynolds number of $32,500$. The simulations were performed for the rotors operating at three different rotor heights above ground ($h/R=$ 1.5, 1.0, 0.5). The low Mach preconditioning was used with the value of pseudo-time step size on the order of the actual time step for both convergence and accuracy. The mesh system in the initial studies consisted of only a background and blade mesh. It was able to capture qualitative features of the wake and ground interaction but the solution was not mesh independent. Later, the mesh system evolved into the utilization of a blade mesh, a background mesh, a system of overset meshes and vortex tracking grids. The system of overset meshes at the ground helps in resolving the tip vortices to sufficiently outboard radial locations. The addition of vortex tracking grids helped in preserving the vortices for longer wake ages as well

as allowed for the background mesh to get coarsened. Furthermore, a fifth order WENO5 reconstruction was used. This complete mesh system was able to give satisfactory qualitative and quantitative predictions with available computational constraints. The various meshes were able to exchange the inoformation using the implicit hole cutting technique. The following are the specific conclusions drawn from the study of hovering micro-scale rotors IGE at various rotor heights:

1. The computations of rotor thrust and power coefficients showed good comparison with the available experimental data. With decreasing rotor height above ground, the thrust increased at a nominally constant power.

2. The phase-averaged predicted azimuthal vorticity contours for a range of wake ages showed good comparison with the experimental results in terms of wake trajectory and vortex strength. An instantaneous snapshot of azimuthal vorticity contour showed that the vortices are well captured even after six blade passages for $h/R = 1.5$.

3. Predicted time-averaged and phase-averaged radial velocity profiles at several radial locations showed reasonable correlation with the experimental data for all rotor heights. CFD predicts a slightly higher maximum radial velocity and at a slightly higher wall distance than that measured in experiment.

4. Flow visualization with the aid of q-criterion and analysis of the wake trajectory showed a large amount of wandering developing in the tip vortices at later wake ages. The wake showed increased scatter for larger rotor heights;

however, the RMS deviations of the trajectory from the phase-averaged radial and vertical position were smaller at larger rotor heights.

5. The tip vortices decayed rapidly in the early wake ages, but they decayed at a much slower rate as the wake expands near the ground. The tip vortices for smaller rotor heights showed faster decay compared to that for larger rotor heights.

6. The interaction of the tip vortex with the ground was observed for all rotor heights. The flow was found to be highly aperiodic. The increased induced velocity from the tip vortex causes the jet flow on the ground to periodically separate and form a separation bubble. The separation bubble formed at one wake age was seen to peel off at a later wake age forming a vortex with opposite sign to the tip vortices.

7. Eddy viscosity contours showed that the turbulence levels near the ground increase with a decrease in rotor height. However, in all cases the turbulence levels are not very high. Ground friction velocities were seen to be higher directly below the convecting tip vortices and were larger for smaller rotor heights.

In addition to the 2-bladed micro-scale rotor simulations, one case of a single micro-rotor operating at one rotor radius above ground ($h/R = 1.0$) was also simulated. The time-averaged radial velocity predictions at various radial locations showed better correlation with experimental radial velocity profiles as compared to

the 2-bladed simulations. This can be attributed to the fact that the single bladed rotor had lower interactions between two consecutive tip vortices as they are 360^0 apart in wake age as compared to being 180^0 apart for the two-bladed rotor case. This leads to lower aperiodicity in the flow field and results in a better capture of the radial velocity profiles at the ground.

5.2.2 Sub-scale rotor

The sub-scale rotor simulations were done using a hovering one-bladed rotor operating IGE. The aspect ratio of the rotor blade was 9.132 and the rotors operated at a tip Mach number of 0.24 and a tip Reynolds number of $250,000$. The simulations were performed for the rotor operating at a rotor height of one rotor radius above ground. Four different rotor blades were generated by using four different tip shapes (rectangular, swept, BERP-like and slotted tip). The slotted tip consists of four slots that had a 90^0 bent starting from the leading edge and ending in the side of the rotor blade. The low Mach preconditioning was used with a constant CFL condition for sub iterations to maintain both convergence and accuracy. Simulations of the sub-scale rotor become challenging because the physical distance of the wall boundaries and outer boundaries grows twice in size compared to the micro-scale rotor. The viscous wall spacing decreases due to a higher Reynolds number and this drives the need for finer mesh points even further. This makes the RANS simulations of the sub-scale rotor IGE challenging from the point of view of computational expense. A novel mesh system was explored that consisted of a blade mesh, a background mesh

along with, vortex tracking grids and a funnel mesh. The addition of vortex tracking grids helped in preserving the vortices for longer wake ages as well as allowed for the background mesh to get coarsened. The funnel mesh followed the path of tip vortices and was used to resolve tip vortices vortices at older wake ages. This mesh system combined with WENO5 reconstruction resulted in an optimum number of mesh points for simulating the sub-scale rotor given the computational constraints. The various meshes were able to exchange the inoformation using the implicit hole cutting technique.

It was observed that the OVERTURNS solver methodology that was successfully used for the micro-scale rotor was insufficient to accurately capture the rotor wake even at early wake ages for the sub-scale rotor. A comparison of eddy viscosity levels from both cases showed that the use of the S–A turbulence model led to very high eddy viscosity levels for the sub-scale rotor while the levels remained very small (close to the laminar flow regime) for the micro-scale rotor. The reason for the prediction of very small laminar eddy viscosity levels for the micro-scale cases stemmed from the highly viscous nature of the flow field owing to a very low tip Reynolds number ($Re = 32,400$). The domination of viscous effects is comparatively subdued in the operation of sub-scale rotor that operated at a higher Reynolds number regime ($Re = 250,000$) and consequently, the S–A model predicted much higher eddy viscosity levels. These high eddy viscosity levels further led to the excessive diffusion of the tip vortices. Since turbulence models "model" the eddy viscosity levels, one way to accurately predict the turbulence in the flow field was to resolve the eddies by using a LES approach. However, a LES approach was computationally

impractical for this problem. Therefore, a hybrid RANS-LES scheme was utilized to overcome this challenge. The hybrid approach also referred to as Delayed Detached Eddy Simulations (DDES) modified the distance function in the existing S–A model in the OVERTURNS solver. This led to reducing the eddy viscosity levels in the flow field by limiting the amount of turbulence production for the sub-scale rotor. The core of the tip vortices was then observed to be nearly laminar as would be expected from a theoretical standpoint. This work showed that one would require to explore improved ways of turbulence modeling for accurately capturing the rotor wake in the case of increasing Reynolds number. The following are the specific conclusions drawn from the modeling of the hovering sub-scale rotor IGE with varying tip shapes.

1. The use of the micro-scale rotor mesh system cannot be extended to the sub-scale rotor without avoiding prohibitive computational costs. This led to a different mesh system adapted to the sub-scale rotor problem.

2. Use of the S–A turbulence model showed diffused vortex strengths at early wake ages and this led to the use of SA-DDES based turbulence modeling.

3. CFD predictions showed a reasonable thrust comparison for both the rectangular and swept tip, whereas BERP-like and slotted tip predictions showed more disagreement with the available experiments. It is shown that the slotted tip requires the highest power among all the four tip shapes.

4. Flow field visualization of the computations from the slotted tip showed that CFD was able to capture in a highly diffused vortex core structure at early

wake ages. The flow inside the slots showed that the turbulence levels increase from inlet to outlet, thus the slots aid in injecting turbulence through the slots as well as momentum.

5. Circulation values obtained as a function of wake age showed a roughly constant and comparable value for all the tip shapes in the CFD computations. However in experiments, the BERP-like tip showed a higher circulation because of a higher measurement of thrust.

6. Overall, the variation of peak swirl velocity varying with increasing wake age showed a good comparison between CFD predictions and experimental results for all tip shapes. Similar to experiments, the slotted tip shape resulted in a rapid decrease of peak swirl velocity in the CFD computations.

7. Core radius growth with increasing wake age was well captured in the computations for all tip shapes. The core radius was seen to grow rapidly in the slotted tip in both computations and experiments.

8. The instantaneous peak to peak swirl velocity profiles showed a underprediction for the rectangular and swept tips, while the BERP-like and slotted showed a good agreement at various wake ages. In both computations and experiments, the slotted tip shape had a similar decrease in peak to peak swirl velocity with wake age.

9. The radial velocity profiles showed a diminished level of fluctuations in the computational results as compared to experimental measurements for the rect-

angular, swept and BERP-like tip shapes. The fluctuations were indictive of the presence of tip vortices. This showed that the computations were not able to resolve the vortices close to the ground as well as would be desired. Because the tip vortex diffused for the slotted tip shape, the radial velocity profiles in both the computational predictions and experimental results looked similar.

10. Analysis of pressure values for the rectangular, swept and BERP-like tips at the ground plane showed striations in the pressure contours indicating the passage of tip vortices. However, these striations were missing for the slotted tip indicating that the tip vortex had reduced unsteady pressure at the ground plane.

5.3 Recommendations for Future Work

The methodology and results presented in this thesis demonstrate the capabilities of high fidelity computations in capturing the rotor wake formation, evolution and and interaction with the ground plane. This provides a detailed insight into the underlying physical mechanisms that can cause brownout phenomenon. Successful validation with available experimental data provides confidence in the accuracy and robustness of the CFD methodology. However, it also highlights the possible challenges in modeling rotor flows in ground effect. Some suggested future studies and potential improvements to the current methodology are listed here:

- Current simulations assumed a smooth ground plane. The effect of a rough ground will provide a more physical level of turbulence near the ground and

thus should be incorporated in future turbulence modeling.

- The predicted core size and core growth data from the rotor simulations can be used to improve the empirical models in the free vortex models.

- The CFD data from the sub-scale rotor simulations can be used to provide inputs for the particle model developed by Syal [9]. This analysis can show the effects of various rotor tip shapes on the resulting sediment mobilization mechanisms.

- The influence of a fuselage and rotor hub can be modeled in the full RANS simulation, and compared with recently acquired experimental results, as well as results from surface singularity (panel) methods.

- Current simulations assume a rigid blade with no cyclic or blade flapping. While this assumption is a good one for small, laboratory-scale rotors, the assumption will not be valid for actual rotorcraft. This would require the need for coupling the CFD solver with a structural dynamics model to accurately model the blade aerodynamics.

- The present work assumed a hovering rotor to simplify the modeling by ignoring dynamic maneuvers. Therefore, future work can focus on modeling the rotor wake interaction with ground plane during a landing/takeoff manuever.

- The effects of scaling at different Reynolds numbers (such as chord based Reynolds number, vortex based Reynolds number and wall jet Reynolds number) can be studied to aid the formation of an appropriate design space for

optimization studies.

- The sub-scale cases were simulated using SA-DDES methodology which was based on modifying the distance function in the Spalart-Allmaras turbulence modeling. Although SA model is recommended for external flows, CFD simulations can also be performed by using an alternative turbulence model such as SST-k-omega model. This model is more suited for internal flows than SA model and can probably be a good candidate to simulate slotted tips.

- CFD flow field data for the sub-scale rotor cases obtained from this work can be fed to the sediment code to understand the effects of using different tip shapes on the resulting dust cloud. This can indicate the benefits of using a particular tip shape.

Bibliography

[1] Mapes, P., Kent, R., and Wood, R., "DOD Helicopter Mishaps FY85-05: Findings and Recommendations," US Air Force, 2008.

[2] Jansen, C., Wennemers, A., and Groen, E., "FlyTact: A Tactile Display Improves a Helicopter Pilots Landing Performance in Degraded Visual En- vironments," *Haptics: Perception, Devices and Scenarios*, Vol. 502, No. 4, 2008, pp. 867–875.

[3] Cowherd, C., "Sandblaster 2: Support of See-Through Technologies for Particulate Brownout," US Army Aviation and Missile Command, 2007.

[4] Pickford, M., "Operating Helicopters Safely in a Degraded Visual Environment in Support of Military Operations," Proceedings of the Royal Aeronautical Society, Rotorcraft Group Conference, London, UK, June 16–17 2010, Royal Aeronautical Society, Rotorcraft Group.

[5] Milluzzo, J., and Leishman, J. G., "Assessment of Rotorcraft Brownout Severity in Terms of Rotor Design Parameters," *Journal of the American Helicopter Society*, Vol. 55, No. 3, July 2010, pp. 32009.

[6] "The Global Elite Forces and Special Operations Webpage," 2011.

[7] Sutherland, A. J., Proposed Mechanism for Sediment Entrainment by Turbulent Flows," *Journal of Geophysical Research*, Vol. 72, No. 24, December 1967, pp. 6,183-194.

[8] Raulesder, J., and Leishman, J. G., "Measurements of the Turbulent Flow Environment on the Ground Below a Hovering Rotor," Proceedings of the 37th European Rotorcraft Forum, Gallarate (VA), Italy, September 13-15, 2011.

[9] Syal, M., "Development of a Lagrangian-Lagrangian Methodology to Predict Brownout Dust Clouds," Ph.D. Dissertation, Department of Aerospace Engineering, University of Maryland at College Park, 2012.

[10] Wenren, Y., Fan, M., Wang, L. and Steinhoff, J., "Vorticity Confinement and Advanced Rendering to Compute and Visualize Complex Flows," AIAA Paper 2006-945, 44th AIAA Aerospace Sciences Meeting and Exhibit, Reno, NV, January 9–12, 2006.

[11] Phillips, C., and Brown, R.E., "Eulerian Simulation of the Fluid Dynamics of Helicopter Brownout," American Helicopter Society 64th Annual Forum Proceedings, Montréal, Canada, April 29–May 1, 2008.

[12] Thomas, S., "A GPU-Accelerated, Hybrid FVM-RANS Methodology For Modeling Rotorcraft Brownout," Ph.D. Dissertation, Department of Aerospace Engineering, University of Maryland at College Park, 2013.

[13] Sydney, A., Baharani, A., and Leishman, J. G., "Understanding Brownout Using Near Wall Dual Phase Flow Measurements," American Helicopter Society 67th Annual Forum Proceedings, May 3–5, 2011.

[14] Leishman, J. G., "Principles of Helicopter Aerodynamics 2nd Edition", Cambridge University Press, New York, NY, 2006.

[15] Johnson, B., Leishman, J. G., and Sydney, A., "Investigation of Sediment Entrainment in Brownout Using High-Speed Particle Image Velocimetry," American Helicopter Society 65th Annual Forum Proceedings, Grapevine, TX, May 27–29, 2009.

[16] Betz, A., "The Ground Effect on Lifting Propellers," *NACA TM 836, April 1937.*

[17] Knight, M., and Hefner, R. A., "Analysis of Ground Effect on the Lifting Airscrew," *NACA TN 835, 1941.*

[18] Cheeseman, I. C., and Bennett, W. E., "The Effect of the Ground on a Helicopter Rotor in Forward Flight," ARC RM 3021, 1955.

[19] Fradenburgh, E. A., "The Helicopter and the Ground Effect Machine," *Journal of the American Helicopter Society*, Vol. 5, No. 4, October 1960, pp. 24-33.

[20] Lighthill, J., "A Simple Fluid-Flow Model of Ground Effect on Hovering," *Journal of Fluid Mechanics*, Vol. 93, part 4, 1979, pp. 781–797.

[21] Hayden, J. S., "The Effect of the Ground on Helicopter Hovering Power Required," 32nd Annual Forum Proceedings of the American Helicopter Society, Washington D.C., May 10-12, 1976.

[22] Rossow J.V., "Effect of Ground and/or Ceiling Planes on Thrust of Rotors in Hover," *NASA TM 86754, 1985.*

[23] Caradonna, F. X., and Tung, C., "Experimental and Analytical Studies of a Model Helicopter Rotor in Hover," *NASA-TM-81232, 1981*

[24] Tangler, J. L., "Experimental Investigation of the Sub-wing Tip and its Vortex Structure,",*NASA-CR-3058, 1978*

[25] Thompson T. L., Komerath N. M., and Gray R. B., "Visualization and Measurement of the Tip Vortex Core of a Rotor Blade in Hover," *AIAA Journal of Aircraft*, Vol. 25, No. 12, December 1988, pp. 1113-1121.

[26] Martin, P. B., Pugilese, G. J., and Leishman, J. G., "High Resolution Trailing Vortex Measurements in the Wake of a Hovering Rotor," *Journal of the American Helicopter Society*, Vol. 48, No. 1, January 2003, pp. 39-52.

[27] Ramasamy, M., and Leishman, J. G., "A Generalized Model for Transitional Rotor Blade Tip Vortices," *Journal of the American Helicopter Society*, Vol. 51, No. 1, January 2006, pp. 92-103.

[28] McAlister, K.W., "Rotor Wake Development during the First Revolution," *Journal of the American Helicopter Society*, Vol. 49, No. 4, October 2004, pp. 371-390.

[29] Ramasamy, M., Leishman, J.G., and Timothy E. Lee., "Flow Field of a Rotating Wing MAV," Proceedings of the 62nd Annual Forum of the American Helicopter Society, Phoenix, AZ, May 2006.

[30] Han Y.O., and Leishman J.G., "Investigation of Helicopter Rotor-Blade-Tip-Vortex Alleviation Using a Slotted Tip," *AIAA Journal*, Vol.42, No.3, March 2004, pp. 524–535.

[31] Milluzzo, J., and Leishman, J. G., "Development of the Turbulent Vortex Sheet in theWake of a Hovering Rotor,", American Helicopter Society 66th Annual Forum Proceedings, Phoenix, AZ, May 21–23, 2013.

[32] Russell, J. W., Sankar, L. N., Tung, C., and Patterson, M. T., "Alterations of Tip Vortex Structure from a Hovering Rotor using Passive Tip Devices," Proceedings of the 53rd Annual Forum of the American Helicopter Society, Virginia Beach, VA, May 1997.

[33] Russell, J. W., Sankar, L. N., and Tung, C., "High Accuracy Studies of the Tip Vortex Structure from a Hovering Rotor," 28th AIAA Fluid Dynamics Conference, AIAA Paper 1997-1845, Snowmass Village, CO, July 1997.

[34] McAlister, K. W., Schuler, C. A., Branum, L., and Wu, J.C., "The 3-D Wake Measurements Near a Hovering Rotor for Determining Profile and Induced Drag," *NASA-TP-3577, August 1995.*

[35] Usta, E., "Application of a Symmetric Total Variation Diminishing Scheme To Aerodynamics of Rotors," Ph.D. Dissertation, Department of Aerospace Engineering, Georgia Institute of Technology, 2002.

[36] Harten, A.,"High Resolution Schemes for Hyperbolic Conservation Laws," *Journal of Computational Physics*, Vol. 49, 1983, pp. 357.

[37] Yee, H. C., Sandham, N. D., and Djomehri, M. J., "Low-dissipative Highorder Shock-capturing Methods Using Characteristic-based Filters," *Journal of Computational Physics*, Vol. 150, No. 1, 1999, pp. 199-238.

[38] Tang, L., "Improved Euler Simulation of Helicopter Vortical Flows," Ph.D. Dissertation, Department of Aerospace Engineering, University of Maryland at College Park, 1998.

[39] Martin, P.B., Pugilese, G.J., and Leishman, J.G., "High Resolution Trailing Vortex Measurements in the Wake of a Hovering Rotor," Proceedings of the 53rd Annual Forum of the American Helicopter Society, 2001.

[40] Duraisamy, K., "Studies in Tip Vortex Formation, Evolution and Control," Ph.D. Dissertation, Department of Aerospace Engineering, University of Maryland at College Park, 2005.

[41] Duraisamy, K., and Baeder, J., "High Resolution Wake Capturing Methodology for Hovering Rotors," *Journal of the American Helicopter Society*, Vol. 52, No. 2, April 2007, pp. 110-122.

[42] Duraisamy, K., Ramasamy, M., Baeder, J., and Leishman, G., "High Resolution Computational and Experimental Study of Hovering Rotor Tip Vortex Formation," *AIAA Journal*, Vol. 45, No. 11, November 2007, pp. 2593-2602.

[43] Lakshminarayan, V. K., and Baeder, J. D., "Computational Investigation of Micro Hovering Rotor Aerodynamics," *Journal of the American Helicopter Society*, Vol. 55, No. 2, April, 2010, pp.22001–1

[44] Lakshminarayan, V. K., "Computational Investigation of Micro-Scale Coaxial Rotor Aerodynamics in Hover," Ph.D. dissertation, Department of Aerospace Engineering, University of Maryland at College Park, 2009.

[45] Taylor, M. K., "A Balsa-Dust Technique for Air-Flow Visualization and its Applications to Flow Through Model Helicopter Rotors in Static Thrust," *NACA Technical Note 2220*, Langley Aeronautical Laboratory, Langley Air Force Base, VA, November 1950.

[46] Curtiss, H. C., Sun, M., Putman, W. F., and Hanker, E. J., "Rotor Aerodynamics in Ground Effect at Low Advance Ratios," *Journal of the American Helicopter Society*, Vol. 29, No. 1, 1984, pp. 48-55.

[47] Light, J.S., "Tip Vortex Geometry of a Hovering Helicopter Rotor in Ground Effect," 45th Annual Forum Proceedings of the American Helicopter Society, Boston, MA, May 22–24, 1989.

[48] Lee, T. E., Leishman, J. G., and Ramasamy, M., "Fluid Dynamics of Interacting Blade Tip Vortices With a Ground Plane," American Helicopter Society 64th Annual Forum Proceedings, Montréal, Canada, April 29–May 1, 2008.

[49] Nathan, N.D., and Green, R.B., "Measurements of a rotor flow in ground effect and visualization of the brown-out phenomenon," American Helicopter Society 64th Annual Forum Proceedings, Montréal, Canada, April 29–May 1, 2008.

[50] Milluzzo, J., Sydney, A., Rauleder, J., Leishman, J. G., "In Ground Effect Aerodynamics of Rotors with Different Blade Tips,", American Helicopter Society 66th Annual Forum Proceedings, Phoenix, AZ, May 11–13, 2010.

[51] Glucksman-Glaser M.S. and Jones A.R., . "Effects of Model Scaling on Sediment Transport in Brownout," 30th AIAA Applied Aerodynamics Conference, New Orleans, LA, June 25–28, 2012.

[52] Sydney, A., and Leishman, J.G., "Measurements of Rotor/Airframe Interactions in Ground Effect Over a Sediment Bed," American Helicopter Society 69th Annual Forum Proceedings, Phoenix, AZ, May 21–23, 2013.

[53] Xin, H., Prasad, J., and Peters, D. A., An analysis of partial ground effect on the aerodynamics of a helicopter rotor," AIAA 38th Aerospace Sciences Meeting and Exhibit, January 2000.

[54] Griffiths, D. A., Ananthan, S., and Leishman, J. G., "Predictions of Rotor Performance in Ground Effect Using a Free-Vortex Wake Model," *Journal of the American Helicopter Society*, Vol. 50, No. 4, October 2005, pp. 302-314.

[55] Bhattacharyya, S. and Conlisk, A., "The structure of the rotor wake in ground effect," AIAA 41th Aerospace Sciences Meeting and Exhibit, January 2003.

[56] Wachspress, D.A., Whitehouse, G.R., Keller, J.D., Yu, K., Gilmore, P., Dorsett, M., McClure, K.,"High Fidelity Rotor Aerodynamic Module for Real Time Rotorcraft Flight Simulation," American Helicopter Society 65th Annual Forum Proceedings, Grapevine, TX, May 27–29, 2009.

[57] D'Andrea, A., "Numerical Analysis of Unsteady Vortical Flows Generated by a Rotorcraft Operating on Ground: A First Assessment of Helicopter Brownout," 65th Annual Forum Proceedings of the American Helicopter Society, Grapevine, TX, May 27-29, 2009.

[58] Brown, R.E., "Rotor Wake Modeling for Flight Dynamic Simulation of Helicopters," *AIAA Journal*, Vol. 38, No. 1, January 2000, pp. 57-63.

[59] Hariharan, N., Wissink, A., Steffen, M., and Potsdam, M., "Tip Vortex Field Resolution Using an Adaptive Dual-Mesh Computational Paradigm," 49th AIAA Aerospace Sciences Meeting, Orlando, FL, January 4–7, 2011,

[60] Kutz, B.M., Kowarsch, U., Kebler, Manuel., and Kramer, E., "Numerical Investigation of Helicopter Rotors in Ground Effect," 30th AIAA Applied Aerodynamics Conference, New Orleans, LA, June 25–28, 2012.

[61] Morales, F., and Squires, K. D., "Simulation of Rotor Vortex Interactions with a Particle-Laden Turbulent Boundary Layer," 29th AIAA Applied Aerodynamics Conference, Honolulu, HI, June 27-30, 2011.

[62] Hirsch, C., "Numerical Computation of Internal and External Flows," Volume 2, Wiley Publishers, 1990.

[63] Spalart, P. R., and Allmaras, S. R., "A One-equation Turbulence Model for Aerodynamic Flows," AIAA Paper 1992-0439, 30th AIAA Aerospace Sciences Meeting and Exhibit, Reno, NV, January 6–9, 1992.

[64] Dacles-Mariani, J., Zilliac, G. G., Chow, J. S., and Bradshaw, P., "Numerical/Experimental Study of a Wingtip Vortex in the Near Field," *AIAA Journal*, Vol. 33, No. 9, 1995, pp. 1561–1568.

[65] Spalart, P.R., and Shur, M., "On the Sensitization of Turbulence Models to Rotation and Curvature," Aerospace Science and Technology, Vol. 1, No. 5, 1997.

[66] Blazek, J., "Computational Fluid Dynamics: Principles and Applications," Second Edition. Elsevier Science, 2006.

[67] Van Leer B., "Towards the Ultimate Conservative Difference Scheme V. A Second-Order Sequel To Godunovs Method," *Journal of Computational Physics*, Vol. 135, No. 2, 1997, pp. 229–248.

[68] Henrick, A. K., Aslam, T. D., and Powers, J. M., "Mapped Weighted Essentially Non-oscillatory Schemes: Achieving Optimal Order Near Critical Points," *Journal of Computational Physics*, Vol. 207, No. 2, 2005, pp. 542–567.

[69] Roe, P., "Approximate Riemann Solvers, Parameter Vectors and Difference Schemes," *Journal of Computational Physics*, Vol. 135, No. 2, 1997, pp. 250–258.

[70] Koren, B., "Multigrid and Defect Correction for the Steady Navier-Stokes Equations", Proceedings of the 11th International Conference on Numerical Methods in Fluid Dynamics , Willamsburg, VA, June 1988.

[71] Jameson, A., and Yoon, S., "Lower-upper implicit schemes with multiple grids for Euler equations", *AIAA Journal*, Vol. 25, No. 7, 1987, pp. 929.

[72] Pulliam, T., and Chaussee, D., "A Diagonal Form of an Implicit Approximate Factorization Algorithm," *Journal of Computational Physics,* Vol. 39, No. 2, February 1981, pp. 347–363.

[73] Warming, R., and Beam, R., "On the Construction and Application of Implicit Factored Schemes for Conservation Laws, SIAM-AMS Proceeedings, Vol. 11, 1978, pp. 85-129.

[74] Buelow P. E. O., Schwer D. A., Feng J., and Merkle C. L. "A Preconditioned Dual-Time, Diagonalized ADI scheme for Unsteady Computations," AIAA paper 1997-2101, 13th AIAA Computational Fluid Dynamics Conference, Snowmass Village, CO, June 29–July 2, 1997.

[75] Pandya, S. A., Venkateswaran, S., and Pulliam, T. H. "Implementation of Preconditioned Dual-Time Procedures in OVERFLOW," AIAA paper 2003-0072, 41st AIAA Aerospace Sciences Meeting and Exhibit, Reno, NV, January 6–9, 2003.

[76] Turkel, E., "Preconditioning Techniques in Computational Fluid Dynamics," *Annual Review of Fluid Mechanics,* Vol. 31, January 1999, pp. 385–416.

[77] Launder, B.E., and G. J. Reece, G.J., and Rodi, W., "Progress in the development of a reynolds-stress turbulent closure," *Journal of Fluid Mechanics*, Vol. 68, No. 3, 1975, pp. 537–566.

[78] Durbin, P., "A reynolds stress model for near wall turbulence," *Journal of Fluid Mechanics*, Vol. 249, 1993, pp. 465–498.

[79] Lee, Y., "On Overset Grids Connectivity and Automated Vortex Tracking in Rotorcraft CFD," Ph.D. Dissertation, Department of Aerospace Engineering, University of Maryland at College Park, 2008.

[80] Gupta, V., "An Investigation of Quad Tilt Rotor Aerodynamics in Helicopter mode, Ph.D. Dissertation, Department of Aerospace Engineering, University of Maryland at College Park, 2005.

[81] Jose, A. I., "Investigation Into the Aerodynamics of Swashplateless Rotors Using CFD-CSD Analysis," Ph.D. Dissertation, Department of Aerospace Engineering, University of Maryland at College Park, 2012.

[82] Lee, Y-L., and Baeder, J.D., "Vortex Tracking in Overset Method for Quad Tilt Rotor Blade Vortex Interaction," AIAA Paper, 2003, pp. 35–31.

[83] Kalra T. S., Lakshminarayan V. K., Baeder J. D., "CFD Validation of Micro Hovering Rotor in Ground Effect", American Helicopter Society 66th Annual Forum Proceedings, Phoenix, AZ, May 11–13, 2010.

[84] Barth, T. J., Puliam, T. H., and Buning P. G., "Navier-Stokes Computations for Exotic Airfoils, 23rd AIAA Aerospace Sciences Meeting, AIAA, Reno, NV, January 1985.

[85] Kalra T. S., Lakshminarayan V. K., Baeder J. D., "CFD Validation of Micro Hovering Rotor in Ground Effect", American Helicopter Society 66th Annual Forum Proceedings, Phoenix, AZ, May 11–13, 2010.

[86] Jeong, J., and Hussain, F., "On the Identification of a Vortex," *Journal of Fluid Mechanics,* Vol. 285, 1995, pp. 69–94.

[87] Harvey, J. K., and Perry, F. J., "Flowfield Produced by Trailing Vortices in the Vicinity of the Ground," *AIAA Journal*, Vol. 9, No. 8, 1971, pp. 1659-1660.

[88] Baharani, A., "Investigation Into The Effects of Aeolian Scaling Parameters On Sediment Mobilization Below a Hovering Rotor," Masters Dissertation, Department of Aerospace Engineering, University of Maryland at College Park, 2011.

[89] Spalart, P.R., Jou, W.-H., Strelets, M., Allmaras, S.R., "Comments on the feasibility of LES for wings, and on a hybrid RANS/LES approach," In: Pro-

ceedings of rst AFOSR international conference on DNS/LES, Ruston, LA, Aug. 1997.

[90] Spalart, P.R., Deck, S., Shur, M.L., Squires, K.D., Strelets, M.Kh., Travin, A., 2006 "A new version of detached eddy simulation, resistant to ambiguous grid densities," *Theoretical Computational Fluid Dynamics*, Vol. 20, No. 3, 2006, pp. 181-195.

[91] Medida. S., and Baeder. J.D., "Numerical Investigation of 3-D Dynamic Stall using Delayed Detached Eddy Simulation," 50th AIAA Aerospace Sciences Meeting, Nashville, TN, 09–12, Jan 2012.

[92] Scotti, A., Meneveau. C., and Lilly, D.K., "Generalized Smagorinsky model for anisotropic grids," *Physics of Fluid A*, Vol. 5, No. 9, 1993, pp. 2306–2308.